HOLOGRAPHIC WAVEFIELD IMAGING FOR SURFACE RECONSTRUCTION AND 3D TOMOGRAPHY

HOLOGRAPHIC WAVEFIELD IMAGING FOR SURFACE RECONSTRUCTION AND 3D TOMOGRAPHY

Proefschrift

ter verkrijging van de graad van doctor
aan de Technische Universiteit Delft,
op gezag van de Rector Magnificus prof. dr. ir. T.H.J.J. van der Hagen,
voorzitter van het College voor Promoties,
in het openbaar te verdedigen op donderdag 10 september 2020 om 10:00 uur

door

Jos VAN ROOIJ
MSc. Technische Universiteit Delft
geboren te Schiedam, Nederland

Dit proefschrift is goedgekeurd door de

promotor: Prof. dr. ir. L.J. van Vliet
copromotor: Dr. J. Kalkman

Samenstelling promotiecommissie:

Rector Magnificus,	voorzitter
Prof.dr.ir. L.J. van Vliet,	Technische Universiteit Delft
Dr. J. Kalkman,	Technische Universiteit Delft
Onafhankelijke leden:	
Prof.dr.ir. F.J. Verbeek	Universiteit Leiden
Prof.dr.ir. A.J. den Boef	VU Amsterdam/ARCNL/ASML
Prof.dr. M. Kujawinska,	Warsaw University of Technology
Prof.dr. H.P. Urbach,	Technische Universiteit Delft
Prof.dr.ir. G.V. Vdovine,	Technische Universiteit Delft

TU Delft Delft University of Technology

An electronic version of this dissertation is available at
http://repository.tudelft.nl/.

Aan mijn ouders
Marja Admiraal en Jan van Rooij

CONTENTS

1

INTRODUCTION

1

Since the invention of the first camera obscura (pinhole camera), and it's subsequent description by Ibn al-Haytham in (AD 965–1040) [1], imaging played an increasingly important role for human beings in a variety of applications, such as medicine, biology, astronomy, industry and earth observation. Ibn al -Haytham first thoroughly described the camera obscura and postulated the idea that light travels along straight lines and that the object is inverted in the image plane (see Fig. 1.1), laying the foundations for geometric optics. Centuries later, the idea of optical microscopy was developed in Europe after the art of grinding lenses was perfected. In the 17th century, Antoni van Leeuwenhoek used a one-lens microscope to examine biological specimens and was the first to visualize bacteria [1]. Although the camera obscura and the first microscope differ greatly from modern-day imaging systems in many aspects (components, type of contrast, capabilities, etc.), all of imaging can be described as creating a correspondence between a point in the object (based on some form of contrast) and a point in the image, in order to make a spatial map of a physical property [2]. The method or technique of forming this correspondence defines the type of imaging method, together with the kind of contrast that is measured.

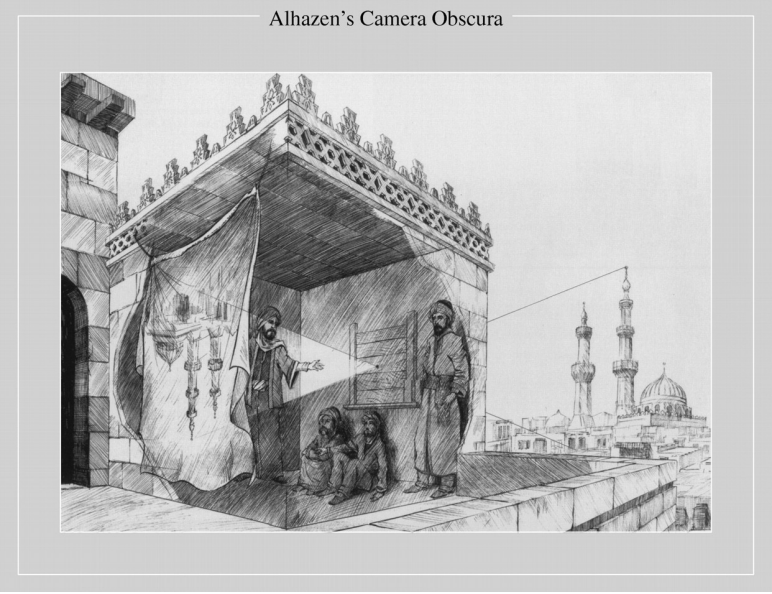

Figure 1.1: The concept of the camera obscura as described by Ibn al-Haytham. An inverted image is formed that can be constructed with a ray diagram. Taken from [1].

Historically, two kinds of developments took place in the advancement of imaging techniques. First of all, the methods improved by which to create an image, such as the invention of the first optical microscope. For example, the invention of the first optical microscope enabled humans to see things that the human eye could not see before in terms of scale. An example of a method by which new kind of contrast could be imaged is the invention of the phase contrast microscope by Frits Zernike in the 1930's, which converts phase shifts in light passing through a transparent specimen to brightness changes

in the image [3].

The second kind of development concerns the methods by which to store the image. For example, the invention of the CCD camera contributed to a shift away from analog optical processing to digital processing. Digital imaging led to the start of joint optical-computational approaches, where optical information is encoded specifically with post-detection digital processing in mind, e.g. to enhance resolution [4], increase the depth of field of the imaging system [5][6] or to image the distribution of primary light sources in 3D [7]. In these cases, the method of forming the image is intertwined with the method of capturing the data.

Such joint optical-computational approaches (now called computational imaging) eventually went on to have an enormous impact on fields like biology (e.g. super resolution microscopy [8]) and process control (e.g. nanoscale metrology [9]). Developments in imaging continue to shape these fields and form an essential element in their success.

1.1. OPTICAL WAVEFIELD IMAGING CONTRAST

Much of today's imaging is done by probing a sample with a kind of wave, such as acoustic waves or light waves. Waves can be mathematically described by, among other things, their complex amplitude (amplitude and phase of the wave) and polarization [10]; the amplitude contains information about the energy of the wave, whereas the phase can be seen as the relative shift of a wave with respect to an identical wave at another point in time. The polarization takes into account the direction in which the field oscillates perpendicular to the propagation direction. A sample generally modulates some or all of these three wave properties. The image contrast can then be seen as the extent to which the sample modulates a specific property. In optical imaging however, we can only measure an intensity distribution of the wavefield from which only the amplitude of the wave can be directly deduced [11]. Whether or not the intensity in the measurement plane is affected by the phase or polarization of the wave depends on how the experiment is conducted.

1.1.1. PHASE CONTRAST

When a light wave travels through a pure phase sample, i.e. a sample that only causes the wavefield to be delayed (see Fig. 1.2), the interaction of a wave with a thin sample can be described as a multiplication of the wave's complex amplitude with a phase factor $e^{i\phi}$ where ϕ is the net phase acquired by the wave due to the sample, and is given by [12]

$$\phi = \frac{2\pi}{\lambda} \int n(s) \mathrm{d}s, \tag{1.1}$$

where $n(s)$ is the refractive index of the sample at position s in the sample, λ is the wavelength of the light and the integral is over the ray path. With regards to measuring the phase, the following scenario's may apply:

- The phase sample is imaged in focus onto the detector. In this case the phase distribution in the input plane does not affect the amplitude in the measurement plane and the amplitude thus does not contain information about the phase, which can thus not be retrieved.

- The wavefield emerging from the sample interferes coherently with a reference wave. In this case the amplitude in the measurement plane is always modulated by the phase of the sample wavefield, whether the sample wavefield propagates or not. Interferometric techniques such as digital holography rely on this principle to determine the phase.
- After transmission through the sample, the wavefield is propagated over a finite distance (greater than zero) before arriving at the detector. In this case the phase distribution in the input plane will affect the amplitude distribution in the measurement plane. The detected amplitude thus encodes the phase. Based on field or intensity propagation models, the amplitude and phase of the object can be extracted. This is utilized in ptychography, where the measurement plane is in the far field.

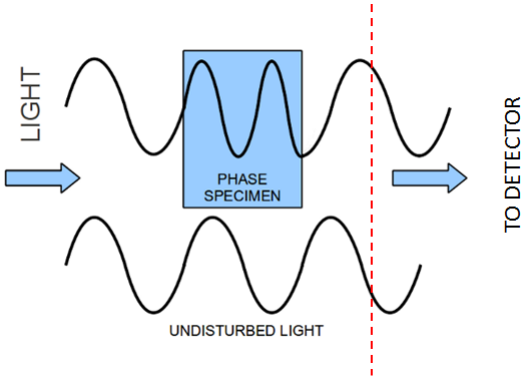

Figure 1.2: Schematic illustration of a samples that generates phase contrast in transmission. The wave exiting from the sample is generally at a different point in its oscillation with respect to an unperturbed reference wave, as is clear when comparing the amplitude of the wave on the red dashed line.

Different methods exist to retrieve the phase of a wave from intensity measurements, two (ptychography and digital holography) are discussed in more detail later in this introduction.

1.1.2. POLARIZATION CONTRAST

In a birefringent material, the refractive index experienced by a lightwave depends on its polarization. This concept is illustrated in Fig. 1.3 using the refractive index ellipsoid. The refractive index ellipsoid is an ellipsoid with three main axes with lengths n_x,n_y and n_z. In Fig. 1.3 (a), the wave propagates in the y-z plane, indicated by the long arrow. The propagating wave can be decomposed into two mutually orthogonal polarization states, which are also orthogonal to the direction of propagation, indicated by the smaller arrows. These two polarization states are the normal modes associated to the wave. The refractive index experienced by these states can be found using the index ellipsoid as follows:

- Draw the ray in the index ellipsoid (given the propagation direction)

- Draw a plane that contains the origin and is normal to the ray
- The plane intersects with the index ellipsoid to form an ellipse; the length of the of the principal axes of the ellipsoid give the refraction indices experienced by the two polarization states.

In a uniaxial material, two of the ellipsoid axes are equal. In case all ellipsoid axes are equal, the material is optically isotropic. In all other cases the ellipsoid has three distinct axes and the material is called biaxial [13]. The refractive index ellipsoid of a uniaxial material is schematically depicted in Fig. 1.3 (b).

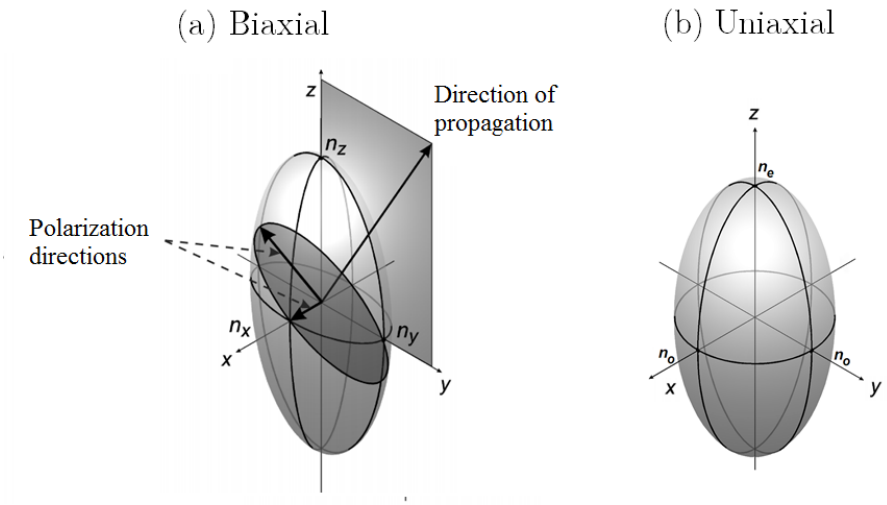

Figure 1.3: a) Refractive index ellipsoid of a biaxial material with $n_x \neq n_y \neq n_z$; the refractive index that a wave experiences depends on its polarization; if a wave is a superposition of polarization states, each polarization component will experience a separate refractive index and travel at a different speed, causing a phase shift between the components. b) Refractive index ellipsoid of a uniaxial material (taken from [14])

.

The two polarization states in Fig. 1.3 (a) experience a different refractive index. This leads to a relative phase shift between the two polarization states, causing a change in the net polarization of the light. This is utilized in polarimetry, where the contrast in the image is generated by this polarization state [15]. A schematic depiction of a polarimetry setup is shown in Fig. 1.4 where the sample is placed between two polarizers. Without a birefringent sample in between, no light would be let through the second polarizer (the analyzer) if it is oriented orthogonal to the input polarization. A birefringent sample, however, changes the polarization of the light after the first polarizer, hence leading to transmission of light and generating a form of polarisation contrast that can be used for imaging. Jones calculus is often used to describe polarized light propagation. Polarized light is then described by a Jones vector, whereas linear optical elements are represented as Jones matrices. The resulting polarization when light crosses an optical element is the

1

product of the Jones matrix of the optical element and the Jones vector of the incoming light. In the case of a cross-polarizer polarimetry setup, this can be represented as [16]

$$\boldsymbol{E_t} = P_x \cdot M \cdot P_x \cdot \boldsymbol{E_0}, \tag{1.2}$$

where $\boldsymbol{E_t}$ is the transmitted field, P_x and P_y the crossed linear polarizers given by Jones matrices

$$P_x = \begin{pmatrix} 1 & 0 \\ 0 & 0 \end{pmatrix}, \tag{1.3}$$

$$P_y = \begin{pmatrix} 0 & 0 \\ 0 & 1 \end{pmatrix}, \tag{1.4}$$

M is a (birefringent) wave retarder and $\boldsymbol{E_0}$ is the incoming field. Under the uniaxial assumption, M is given by

$$M = \begin{pmatrix} \cos(\theta) & \sin(\theta) \\ -\sin(\theta) & \cos(\theta) \end{pmatrix} \begin{pmatrix} e^{\frac{i\delta}{2}} & 0 \\ 0 & e^{-\frac{i\delta}{2}} \end{pmatrix} \begin{pmatrix} \cos(\theta) & -\sin(\theta) \\ \sin(\theta) & \cos(\theta) \end{pmatrix}$$

with δ the relative phase shift between the two polarization components and θ the in-plane orientation of the optic axis of the fiber with respect to the y,z-plane. The geometry is illustrated in Fig. 1.4. In Chapter 4, we will use Jones calculus to show in theory and experiment that the amplitude, phase and polarisation can be combined using digital holography in order to reconstruct phase and polarisation contrast in 3D.

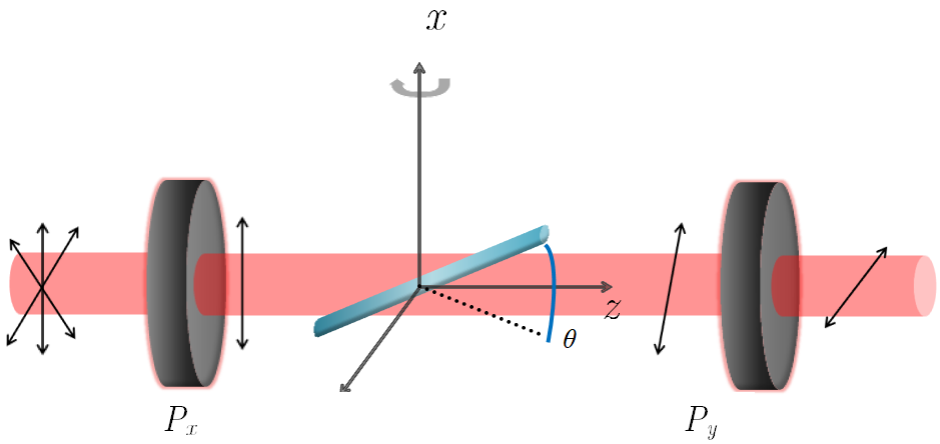

Figure 1.4: Cross-polarizer setup; Unpolarized light goes through the first polarizer P_x to obtain polarized light along the vertical direction. After travelling through the birefringent sample, the polarization of the wave changes. The light then passes through a polarizer P_y (the analyzer) to filter out all the light except the horizontally polarized light.

1.2. COMPUTATIONAL IMAGING

In digital imaging, characteristics of an object are directly or indirectly digitally encoded. One of the main advantages is that digital data can be processed. This can be either directly on the image (such as the filtering to enhance an image), or this can involve complex algorithms to form the image from digitally acquired data as is the case in computational imaging. This results in imaging systems with greatly enhanced capabilities compared to traditional imaging systems [2], for example super resolution microscopy techniques, or with completely new capabilities that were not possible with conventional imaging in the first place, such as 3D imaging through computed tomography (CT) or quantitative phase imaging. Often, multiple computational imaging techniques are combined such as in 3D quantitative phase imaging. In this case, computational imaging is involved in two stages; firstly in the calculation of the phase and/or amplitude projections and secondly in the tomographic reconstruction. In order to illustrate the concept of computational imaging in optics, we first discuss some techniques to retrieve the phase, and after that the principles of tomographic reconstruction.

1.2.1. PTYCHOGRAPHY

In optical imaging, phase cannot be measured directly due the very high temporal frequency of the optical wavefield. However, the phase can be retrieved from intensity measurements only. An example is ptychography, a phase retrieval method that does not use a reference wave to interfere with the object scattered wave. Instead, in ptychography an unknown object is probed by a lightwave at different shifted positions [12]. Given the translational invariance of the probe and the object, together with known shifts of the probe with respect to the sample, the phase of the wavefield can be retrieved with an inverse (iterative) operation. Convergence typically takes place after a few tens of iterations. The benefit of ptychography is that it does not require a reference wave to retrieve the interference, and as such is less prone to setup instabilities. However, it does require multiple measurements and an iterative computation scheme.

1.2.2. DIGITAL HOLOGRAPHY

In holography , a known reference wave R is superimposed onto the object wave O (both from the same coherent light source) and the intensity in the sensor plane is given by [17]

$$\begin{aligned} I(x,y) &= \left|O(x,y)+R(x,y)\right|^2 \\ &= O^*(x,y)R(x,y)+O(x,y)R^*(x,y)+\left|O(x,y)\right|^2+\left|R(x,y)\right|^2. \end{aligned}$$

From the resulting cross-terms, the amplitude and the phase of the object wave can be retrieved. Only one of the two cross-terms is needed in order to reconstruct the object wave, as they contain the same information. If there is no angle between the object and reference waves, the diffraction orders will overlap, contaminating the desired image. This can be solved by either introducing an angle between the object wave and the reference wave, or by recording multiple phase-shifted holograms to remove the unwanted diffraction orders [18]. Since wave propagation can be described mathematically using diffraction integrals, knowledge of the complex object field $O(\xi,\eta)$(amplitude

and phase) in the sensor plane enables one to calculate the object field in any arbitrary plane in three-dimensional free space. For example, assuming paraxial propagation the object field at a plane x, y at a distance z from the input plane is described by Fresnel diffraction[19] and can be calculated with

$$O(x,y,z) = \frac{e^{ikz}}{i\lambda z}\iint_{-\infty}^{\infty} O(\xi,\eta,0)e^{\frac{ik}{2z}((x-\xi)^2+(y-\eta)^2)}d\xi d\eta \tag{1.5}$$

with $O_(\xi,\eta)$ the field in the input plane, $O(x,y,z)$ the input field propagated over a distance z to the output plane, and $k = \frac{2\pi}{\lambda}$. Thus, digital holography allows for numerically refocussing of the wavefield, which has applications in extended focus imaging [20] and tomography [21]. Since the complex wavefield is known, digital holography can be used for phase contrast imaging. The wrapped phase can be calculated as the inverse tangent of the ratio of the imaginary and real parts of the object wavefield

$$\phi(x,y,z)_{\text{wrapped}} = \arctan\frac{\text{Im}[O(x,y,z)]}{\text{Re}[O(x,y,z)]}. \tag{1.6}$$

The unwrapped phase can then be found by applying a phase unwrapping algorithm which ensures that all appropriate multiples of 2π have been included in ϕ [22].

Digital holography setups can be broadly categorized in reflection and transmission setups, of which two examples are shown in Fig. 1.5. Although the underlying mathematics describing the interference is completely identical, the difference between the two setups is in how the object wave is formed. In reflection geometry, a light waves illuminates an opaque surface and the reflected beam interferes with the reference wave, whereas in transmission geometry the light goes through a transparent or weakly scattering sample before interfering with the reference wave. The nature of the information contained in both object waves is thus completely different. For volumetric imaging, the transmission setup is most suitable. In chapter 2, we will use the reflection based geometry to do depth resolved imaging with digital holography. In chapter 3 and 4, we use the transmission geometry to achieve volumetric phase and polarization contrast respectively.

1.2.3. COMPUTED TOMOGRAPHY

In order to retrieve 3D object contrast information the probing wave must interact with the complete object. One way of achieving this, is by sending the wave through the object and measuring the transmitted wave. An advantage is that the wave has to pass any voxel in the object only once per projection, increasing the imaging depth. A disadvantage is that, as mentioned in the previous section, the measured field leads only to a summation over the projection path of some quantity related to the contrast. The object must thus be probed from different angles in order to reconstruct the 3D object contrast. Various reconstruction algorithms exist, such as algebraic reconstruction techniques (ART) and filtered backprojection (FBP). These concepts are widely used in hospitals for diagnostics under the name of computed tomography (CT) with X-ray radiation. Due to the short wavelength of the X-rays, multiple scattering effects and diffraction can be neglected, and the light going through the sample can be considered as propagating in straight rays.

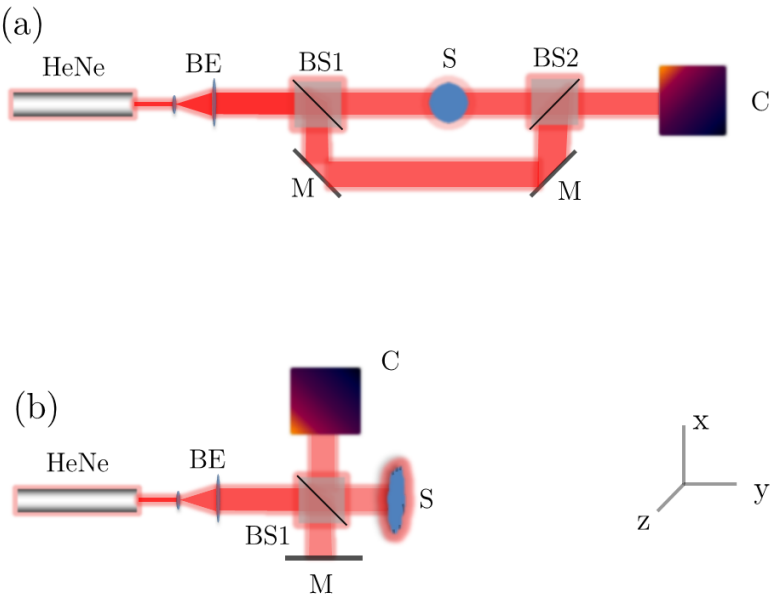

Figure 1.5: Digital holography setup in transmission (a) and reflection (b) geometry. HeNe: Helium-Neon laser, BE: beam expander, BS: beam splitter, S: sample, M: mirror, C: camera.

Mathematically, the relation between the measured projection and the object $f(x,y)$ can be expressed with the Radon transform

$$p(\theta,t) = \int_{-\infty}^{\infty}\int_{-\infty}^{\infty} f(x,y)\delta(x\cos\theta + y\sin\theta - t)\mathrm{d}x\mathrm{d}y, \tag{1.7}$$

The function $p(\theta,t)$ is called the sinogram (see Fig. 1.6 (b)), with θ the angle at which the sample is illuminated and t the coordinate on the detector line (see Fig. 1.6). The delta function implies a light ray travelling through the object in a straight line at angle θ. In order to reconstruct the object $f(x,y)$ from measurements $p(\theta,t)$, one can invert the Radon transform with filtered back projection (FBP). In order to do this, the Fourier slice theorem is used, which states that the 1D Fourier transform of a projection is equal to a radial cross-section of the 2D object Fourier transform perpendicular to the projection direction. The filtered back projection reconstruction is then defined as

$$f(x,y) = \int_0^{\pi}\int_{-\infty}^{\infty} P_\theta(f_t)\mathrm{e}^{i2\pi f_t t}|f_t|\mathrm{d}f_t\mathrm{d}\theta, \tag{1.8}$$

where $P_\theta(f_t)$ is the 1D Fourier transform of $p(\theta,t)$ and $|f_t|$ is a filter in the frequency domain. The FBP reconstruction of an object from the sinogram is schematically illustrated in Fig. 1.6 (c). As mentioned, technically, FBP is valid only when the light travels through the sample in straight rays and diffraction can be neglected; an approximation that holds well for CT with X-ray radiation due to the high energy of the photons, but may be violated in optical tomography.

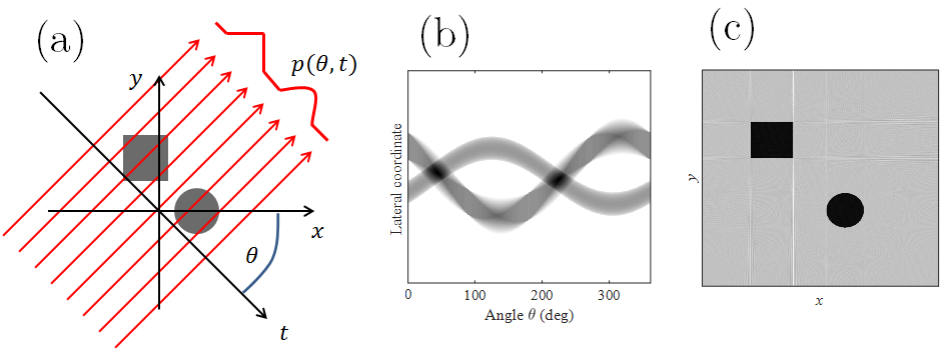

Figure 1.6: Schematic overview of FBP. (a) Projection geometry , (b) the sinogram of the object, (c) the FBP reconstruction of the object from the singoram.

1.2.4. DEPTH RESOLVED IMAGING

Another way of performing tomography is in reflection geometry. In this case it is possible to localize information in the object wave to a single point in the depth direction without scanning the illumination or rotating the object like in computed tomography. The simplest of such cases is when the object is a single opaque scattering surface, since there is only one point in 3D space where the wave interacts with the object. Wavelength scanning interferometry (WSI) is one such technique to reconstruct the object surface [23]. WSI is based on the interference signal of a low-coherence (white light) source. The interference between the reference field and object wave field imaged with a lens onto the camera changes as a function of the distance of the scanning reference mirror. The technique can acquire surface topography in full-field at sub-nanometer axial resolution. Furthermore, it can be applied to surfaces that are complex in terms of roughness and discontinuities, but has a long acquisition time due to the requirement of axial scanning. Time-domain OCT is similar to WSI but instead of only measuring surface topography, it is used to image the inside of turbid media, such as retinal tissue or skin [24]. Time-domain OCT is based on lateral scanning and the use of a focusing lens to suppress scattered light while measuring deep in tissue. In Fourier-domain OCT an axial depth scan is calculated with a Fourier transform of an acquired interference spectrum, and as such does not require axial scanning, but is in general not full-field and therefore lateral scanning is necessary (except for swept-source full-field OCT). Digital holography can be used to reconstruct depth as well, since it allows reconstruction of the object wavefield in three dimensions. A way to determine the surface location is to apply a metric to determine the local amount of focus of the intensity of the reconstructed wavefield, such as the gray-scale variance, and to determine at which depth the metric peaks [20]. This can be applied in order to do extended depth-of-focus imaging, since each part of the image can be reconstructed in-focus, even those parts of the object traditionally outside of the depth-of-field (DOF) of the imaging system. Another application can be in surface metrology; both applications will be exploited in this thesis. In chapter 2, resolving depth of a reflecting surface will be done for the purpose of metrol-

ogy. In chapter 3 and 4, we use depth reconstruction to achieve extended depth-of-focus imaging for the purpose of noise suppression in volumetric imaging.

1.3. OPTICAL TOMOGRAPHY

Computed tomography can be done with light in the optical wavelength range. Advantages include the non-ionizing character of the radiation, the high spatial resolution and the cost-efficiency [25]. There are also drawbacks however, such as diffraction and tissue scattering. The former typically plays a role when imaging biological specimens in 3D, whereas the latter limits the attainable imaging depth. Two optical tomographic imaging modalities will be discussed, namely, optical projection tomography (OPT) and optical diffraction tomography (ODT).

1.3.1. OPTICAL PROJECTION TOMOGRAPHY

Optical projection tomography is the optical analog of X-ray CT, in the sense that the object is reconstructed from the projections of transmitted or emitted optical radiation [26]. In OPT, emission and attenuation contrast can be measured. Emission contrast results from the excitation of fluorescent markers or intrinsic luminescence in the sample, which can be used to image different tissue regions or particular types of proteins [27]. Attenuation contrast results from the transmission of light through the sample where the resulting loss of light due to scattering and absorption provides structural information about the sample. In OPT, with a wavelength in the order of hundreds of nanometers, the effect of diffraction plays a role. Refraction and scattering are sample dependent effects that can be minimized using, for example, optical clearing techniques. Whether or not diffraction plays a significant role depends on the imaging system parameters. Optical tomography therefore requires the sample to be within the depth of field (DOF) of the system, during the rotation of the sample. Since the lateral resolution is proportional to the numerical aperture of the objective lens, while the depth of field is inversely proportional, there exists a trade-off between sample thickness and resolution. This is schematically depicted in Fig. 1.7. Moreover, the resolution is not isotropic throughout the sample, meaning that the point spread function (PSF) is spatially variant. Approaches have been developed to compensate for these effects. One approach is to correct for the spatially variant PSF by means of a deconvolution method [28]. The 3D image is thus first reconstructed by means of conventional FBP, and then corrected. Another approach is to incorporate the PSF in an iterative reconstruction [29]. In this case the FBP reconstruction functions as the first estimate of the object. Using the measured beam shape a forward projection is calculated, after which the object is again reconstructed.

1.3.2. OPTICAL DIFFRACTION TOMOGRAPHY

In conventional CT, the light is considered to travel through the sample along straight lines, which is called the ray approximation.This approximation becomes less accurate when the wavelength is comparable to the sample size. In biomedical optical imaging for example, the size of the features of interest is generally in the same order of magnitude as the wavelength used. Furthermore, the larger the numerical aperture of the objective, the higher the resolution but the lower the depth of field (DOF), which is illustrated in

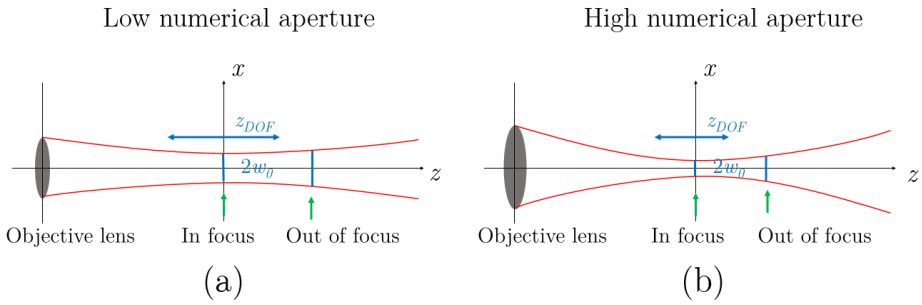

Figure 1.7: Illustration of the concepts of numerical aperture and depth of field; a lower numerical aperture (NA) and thus larger depth of field (a) implies that objects further away from the focal plane will still appear in focus, but also results in a larger beam width w_0 in-focus and thus poorer resolution than in the case of high NA (b).

Fig. 1.7. Features outside of the image plane and beyond the depth of field will be imaged onto the detector, but with a degree of defocus. When repeating the acquisition for different angles, either through sample rotation or angular scanning of the illumination beam, the sinogram will then contain projections where relevant information is imaged out of focus. This negatively affects the reconstructed image if conventional FBP is used. Optical diffraction tomography (ODT) incorporates diffraction, using certain approximations regarding the sample. Most commonly used are the Born approximation, which asserts that the absolute optical path length difference through the sample is small, and the Rytov approximation, which asserts that the gradient in optical path length difference is sufficiently small [30]. In order to reconstruct an image of the refractive index (RI) distribution of the sample it is necessary that the complex wavefield be recorded for each projection angle, rather than just the intensity image. This is most commonly done using digital holography. Similar to FBP, the projection can then be related to the spatial frequency spectrum of the object of interest, with two differences:

- the Fourier transform is now over the projection of the complex scattered wave instead of the intensity
- each projection is mapped along arcs in the Fourier space, instead of lines as is the case in FBP. This is illustrated in Fig. 1.8.

The radius of the arcs in spatial frequency space limits the maximum resolution and is given by

$$k_m = \frac{2\pi n_m}{\lambda}, \tag{1.9}$$

with n_m the refractive index of the background medium. It can be seen that for small wavelengths λ the radius of the arcs becomes large, approximating the straight lines in the case of the ray approximation to tomography in Fig. 1.8 a). In practice, whether the complete arc can be filled depends on the resolution of the imaging system. The smaller

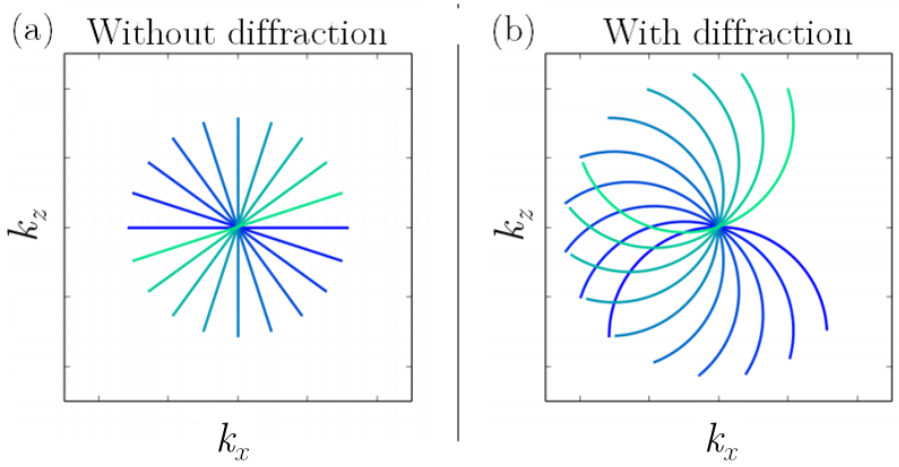

Figure 1.8: Schematic comparison between the Fourier slice (a) and the Fourier diffraction (b) theorems; the Fourier slice theorem is used in FBP and assumes an infinitely small wavelength, i.e. straight ray projections. The real-valued intensity projections are then mapped onto lines in Fourier space. In ODT the finite wavelength is taken into account, leading the complex projection data to be mapped onto arcs. Adapted from [31]

the numerical aperture of the imaging system, the smaller the part of the arc that is filled, and thus the better it will approximate a straight line. By measuring the complex scattered wave from different directions, the spatial frequency spectrum of the sample can be filled. The object can then be reconstructed with an inverse Fourier transform. Optical diffraction tomography has been applied mainly on the scale of single cells (several tens of microns) [32][33][34], or on larger (mm size) synthetic samples such as a lens [35].

1.3.3. ZEBRAFISH IMAGING

In biology and medicine, small animal models are often studied to understand disease progression and treatment, eventually enabling (improved) treatment for human beings. For this purpose, zebrafish have gained popularity over the past decades, due to the fact that they grow and reproduce rapidly and are relatively cheap to keep. An additional advantage is that they are optically transparent in the embryo and larva stages, making them especially suitable for studying embryologically and genetically tractable disease models. Thus, zebrafish models of a wide variety of human diseases have been developed [36]. Zebrafish research has been conducted with a variety of optical imaging techniques, among which are OPT [37] and OCT [38]. An example of an OPT virtual cross-section of a zebrafish is shown in Fig. 1.9.

1.3.4. OPTICAL CLEARING

Biological objects are often scattering, even when non absorbing, due to the fact that they consist of different types of biological materials having different refractive indices.

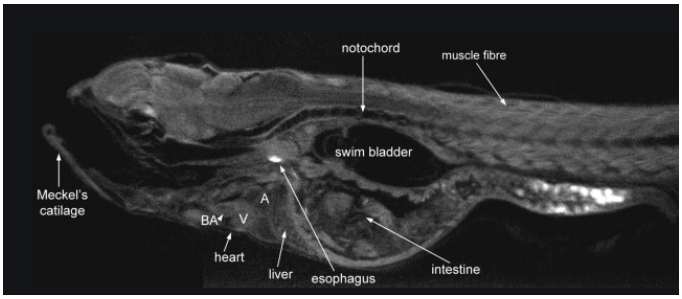

Figure 1.9: Example of an OPT virtual cross-section of a zebrafish taken from [39]

.

This causes light to scatter due to refraction and limits the penetration of (visible) light into the tissue, causing both the imaging resolution and contrast to decrease when going deeper into the tissue. This is an obstacle for high resolution volumetric imaging. In order to enable studying larger tissue samples in 3D, optical clearing of tissue is regularly used. The aim of optical clearing is to reduce the width of the RI distribution in a sample in order to reduce the amount of scattering. Examples of clearing agents are a mixture of benzyl alcohol/benzyl benzoate (BABB) with a RI of 1.55, and glycerol (RI of 1.47) [40]. There are different views on how the clearing mechanism works, for example that optical clearing agents with higher RI diffuse into tissues, matching the RI's of tissue components of extracellular fluid [41].

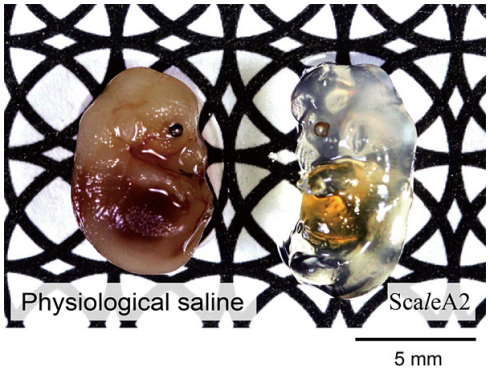

Figure 1.10: Mouse embryo's extracted from a physiological saline solution (left) and after optical clearing (right). Optical clearing reduces scattering and thereby improves light transmission through tissue. Image taken from [42]

.

1.4. THESIS CHALLENGES

The general theme of this thesis is 3D imaging using the complete optical wavefield. The first challenge is to reconstruct the depth profile from rough reflecting objects in the

millimeter range, and to theoretically understand the attainable axial resolution. The second challenge is to extend the use of ODT from small cellular level biological objects to large scale biological tissue. In order to achieve this, the object contrast must be as low as possible in order to measure useful projections, while the imaging method must be sensitive enough to still detect the contrast. The third challenge is to do multi-contrast imaging of phase and polarisation contrast.

1.4.1. OUTLINE OF THIS THESIS

CHAPTER 2: DEPTH RESOLVED DIGITAL HOLOGRAPHY

This chapter presents sub-millimeter full-field depth-from-focus digital holography of surface topography of rough objects. Although depth can be accurately reconstructed using techniques such as white light or wavelength scanning interferometry, the depth range of such techniques is generally limited to the order of the size of a wavelength. Depth resolved imaging has been achieved with digital holography before, however, with limited axial resolution. First, the axial resolution is described theoretically, and the feasibility of sub-millimeter resolution is demonstrated assuming standard experimental conditions. Then, it is experimentally demonstrated that an axial resolution of 100 micron can be achieved.

CHAPTER 3: LARGE SCALE OPTICAL DIFFRACTION TOMOGRAPHY

In this chapter, large-scale optical diffraction tomography is demonstrated on a zebrafish larva using optical clearing to reduce RI contrast and thus scattering, while obtaining high RI sensitivity in order to image the remaining contrast. We demonstrate that combining off-axis placement of the sample in combination with a large number of projections is necessary in order to achieve sufficient RI sensitivity. Finally, we demonstrate that the technique can be applied to detect the cryo-injured region in a millimeter sized adult zebrafish heart.

CHAPTER 4: POLARISATION CONTRAST OPTICAL DIFFRACTION TOMOGRAPHY

In this chapter large-scale multi-contrast ODT is experimentally demonstrated with polarization and phase-contrast. We show that by probing the sample with a polarized wave, the phase of the parallel polarized output contains the average phase-contrast, while the amplitude of the orthogonally polarized output contains the polarization contrast. Furthermore, we show that FBP can only be used for reconstruction of the polarization contrast in the case of thin samples or small birefringence. Finally, we propose a solution to the reconstruction problem in case this condition is not met.

CHAPTER 5: CONCLUSION AND OUTLOOK

In this chapter the main results are summarized and future directions for research are presented.

REFERENCES

[1] A. H. Zewail, *Micrographia of the twenty-first century: from camera obscura to 4D microscopy,* Phil. Trans. R. Soc. A. **368**, 1191 (2010).

[2] J. N. Mait, G. W. Euliss, and R. A. Athale, *Computational imaging,* Adv. Opt. Photon. **10**, 409 (2018).

[3] F. Zernike, *How i discovered phase contrast,* **121**, 345 (1955).

[4] W. T. Cathey, B. R. Frieden, W. T. Rhodes, and C. K. Rushforth, *Image gathering and processing for enhanced resolution,* J. Opt. Soc. Am. A **1**, 241 (1984).

[5] E. R. Dowski and W. T. Cathey, *Extended depth of field through wave-front coding,* Appl. Opt. **34**, 1859 (1995).

[6] J. van der Gracht, E. R. Dowski, W. T. Cathey, and J. P. Bowen, *Aspheric optical elements for extended depth-of-field imaging,* in *Novel Optical Systems Design and Optimization*, Vol. 2537 (1995) pp. 279 – 288.

[7] D. L. Marks, R. A. Stack, and D. J. Brady, *Three-dimensional coherence imaging in the Fresnel domain,* Appl. Opt. **38**, 1332 (1999).

[8] L. Schermelleh, A. Ferrand, T. Huser, C. Eggeling, M. Sauer, O. Biehlmaier, and G. P. C. Drummen, *Super-resolution microscopy demystified,* Nat. Cell Biol. **21**, 72 (2019).

[9] R. M. Silver, B. M. Barnes, R. Attota, J. Jun, M. Stocker, E. Marx, and H. J. Patrick, *Scatterfield microscopy for extending the limits of image-based optical metrology,* Appl. Opt. **46**, 4248 (2007).

[10] M. Kujawińska and T. Kozacki, *Holographic television: Status and future,* in *Optical Imaging and Metrology* (John Wiley Sons, Ltd) Chap. 3, pp. 57–94.

[11] Y. Shechtman, Y. C. Eldar, O. Cohen, H. N. Chapman, J. Miao, and M. Segev, *Phase retrieval with application to optical imaging: A contemporary overview,* IEEE Signal Processing Magazine **32**, 87 (2015).

[12] J. Rodenburg, *Ptychography and related diffractive imaging methods,* Adv. Imag. Electron. Phys. **150**, 87 (2008).

[13] N. Ortega-Quijano, J. Fade, and M. Alouini, *Generalized Jones matrix method for homogeneous biaxial samples,* Opt. Express **23**, 20428 (2015).

[14] J. Farnell, *Nonlinear and tunable metamaterials*, Ph.D. thesis (2010).

[15] E. Dijkstra, H. Meekes, and M. Kremers, *The high-accuracy universal polarimeter,* Journal of Physics D: Applied Physics **24**, 1861 (1991).

[16] M. Menzel, K. Michielsen, H. De Raedt, J. Reckfort, K. Amunts, and M. Axer, *A Jones matrix formalism for simulating three-dimensional polarized light imaging of brain tissue,* .

[17] U. Schnars, C. Falldorf, J. Watson, and W. Jüptner, *Fundamental principles of holography,* in *Digital Holography and Wavefront Sensing: Principles, Techniques and Applications* (Springer Berlin Heidelberg, Berlin, Heidelberg, 2015) pp. 5–38.

[18] I. Yamaguchi and T. Zhang, *Phase-shifting digital holography,* Opt. Lett. **22**, 1268 (1997).

[19] U. Schnars, C. Falldorf, J. Watson, and W. Jüptner, *Digital holography,* in *Digital Holography and Wavefront Sensing: Principles, Techniques and Applications* (Springer Berlin Heidelberg, Berlin, Heidelberg, 2015) pp. 39–68.

[20] C. P. McElhinney, B. M. Hennelly, and T. J. Naughton, *Extended focused imaging for digital holograms of macroscopic three-dimensional objects,* Appl. Opt. **47**, D71 (2008).

[21] J. Kostencka, T. Kozacki, M. Dudek, and M. Kujawińska, *Noise suppressed optical diffraction tomography with autofocus correction,* Opt. Express **22**, 5731 (2014).

[22] D. C. Ghiglia and L. A. Romero, *Robust two-dimensional weighted and unweighted phase unwrapping that uses fast transforms and iterative methods,* J. Opt. Soc. Am. A **11**, 107 (1994).

[23] A. Dávila, *Wavelength scanning interferometry using multiple light sources,* Opt. Express **24**, 5311 (2016).

[24] R. Forte, G. L. Cennamo, M. L. Finelli, and G. de Crecchio, *Comparison of time domain stratus oct and spectral domain slo/oct for assessment of macular thickness and volume,* Eye **23**, 2071 EP (2008), clinical Study.

[25] C. Balas, *Review of biomedical optical imaging—a powerful, non-invasive, non-ionizing technology for improvingin vivodiagnosis,* Meas. Sci. Technol. **20**, 104020 (2009).

[26] J. Sharpe, U. Ahlgren, P. Perry, B. Hill, A. Ross, J. Hecksher-Sørensen, R. Baldock, and D. Davidson, *Optical projection tomography as a tool for 3D microscopy and gene expression studies,* **296**, 541 (2002).

[27] *Chapter twenty - morphometrics, 3D imaging, and craniofacial development,* in *Craniofacial Development*, Current Topics in Developmental Biology, Vol. 115, edited by Y. Chai (Academic Press, 2015) pp. 561 – 597.

[28] J. van der Horst and J. Kalkman, *Image resolution and deconvolution in optical tomography,* Opt. Express **24**, 24460 (2016).

[29] A. K. Trull, J. van der Horst, W. J. Palenstijn, L. J. van Vliet, T. van Leeuwen, and J. Kalkman, *Point spread function based image reconstruction in optical projection tomography,* Phys. Med. & Biol. **62**, 7784.

[30] *An extended rytov approximation and its significance for remote sensing and inverse scattering,* Opt. Commun. **18**, 421 (1976).

[31] P. Müller, M. Schürmann, and J. Guck, *The theory of diffraction tomography,* (2015).

[32] Y. Sung, W. Choi, C. Fang-Yen, K. Badizadegan, R. R. Dasari, and M. S. Feld, *Optical diffraction tomography for high resolution live cell imaging,* Opt. Express **17**, 266 (2009).

[33] S. Shin, D. Kim, K. Kim, and Y. Park, *Super-resolution three-dimensional fluorescence and optical diffraction tomography of live cells using structured illumination generated by a digital micromirror device,* Sci. Rep. **8**, 9183 (2018).

[34] K. Lee, S. Shin, Z. Yaqoob, P. T. C. So, and Y. Park, *Low-coherent optical diffraction tomography by angle-scanning illumination,* J. Biophotonics **12**, e201800289.

[35] K. Kim, J. Yoon, and Y. Park, *Large-scale optical diffraction tomography for inspection of optical plastic lenses,* Opt. Lett. **41**, 934 (2016).

[36] G. J. Lieschke and P. D. Currie, *Animal models of human disease: zebrafish swim into view.* Nat. Rev. Genet. **8**, 353 (2007).

[37] J. A. Mcginty, H. G. B. Taylor, L. Chen, L. Bugeon, J. R. Lamb, M. J. Dallman, and P. M. W. French, *In vivo fluorescence lifetime optical projection tomography,* Biomed. Opt. Express **2**, 1340 (2011).

[38] K. D. Rao, A. Alex, Y. Verma, S. Thampi, and P. K. Gupta, *Real-time in vivo imaging of adult zebrafish brain using optical coherence tomography,* J. Biophotonics **2**, 288.

[39] *Optical projection tomography for spatio-temporal analysis in the zebrafish,* in *The Zebrafish: Cellular and Developmental Biology*, Methods in Cell Biology, Vol. 76 (Academic Press, 2004) pp. 37 – 50.

[40] E. A. Genina, A. N. Bashkatov, and V. V. Tuchin, *Tissue optical immersion clearing,* Expert Review of Medical Devices **7**, 825 (2010).

[41] V. V. Tuchin, I. L. Maksimova, D. A. Zimnyakov, I. L. Kon, A. H. Mavlyutov, and A. A. Mishin, *Light propagation in tissues with controlled optical properties,* J. Biomed. Opt. **2**, 401 (1997).

[42] H. Hama, H. Kurokawa, H. Kawano, R. Ando, T. Shimogori, H. Noda, K. Fukami, A. Sakaue-Sawano, and A. Miyawaki, *Scale: a chemical approach for fluorescence imaging and reconstruction of transparent mouse brain,* Nat. Neurosci. **14**, 1481 EP (2011).

2

SUB-MILLIMETER DEPTH RESOLVED DIGITAL HOLOGRAPHY

2.1. ABSTRACT

We present sub-millimeter full-field depth from focus digital holography of surface topography of rough objects. For each pixel, the depth of the object is calculated from the variance of the intensity image over a set of reconstruction distances. First, we theoretically describe the axial resolution of this method and show that sub-millimeter resolution is feasible. Second, using a digital holography setup without magnifying optics or lateral scanning we experimentally demonstrate 100 micron axial resolution depth ranging and surface topography imaging. This is significantly better than what has previously been reported using digital holography and could make this technique useful for rapid large area characterization of surface topography of objects.

2.2. INTRODUCTION

Surface metrology and absolute distance measurement are essential in many applications; for example in the field of geosciences, remote sensing aims to reconstruct the surface topology and track changes of the earth surface over time. On a much smaller scale, optical measurement of surface topography has become vital in many process and quality control methods [1]. A number of established optical surface imaging techniques are available, such as Phase Shifting Interferometry (PSI), White Light Interferometry (WLI), Optical Coherence Tomography (OCT), Digital Holographic Microscopy (DHM), and Focus Variation Microscopy (FVM). In PSI a controlled phase shift is applied to the reference wave while acquiring the full field interference pattern. From a series of images, acquired at different phase shifts, the phase can be calculated with 2π ambiguity. Since phase unwrapping is necessary, PSI is problematic with phase discontinuities greater than 2π [2]. WLI is based on the interference signal of a low coherence (white light) source. The interference between the reference field and object wavefield imaged with a lens onto the camera changes as a function of the distance of the scanning reference mirror. The technique can acquire surface topography in full-field at sub nanometer axial resolution. Furthermore, in contrast to PSI [3], it can be applied to surfaces that are complex in terms of roughness and discontinuities, but has a long acquisition time due to the requirement of axial scanning. Time-domain OCT is similar to WLI but instead of only measuring surface topography, it is used to image the inside of turbid media such as retinal tissue or skin. Time-domain OCT is based on lateral scanning and the use of a focusing lens to suppress scattered light while measuring deep in tissue. In Fourier-domain OCT an axial depth scan is calculated with a Fourier transform of an acquired interference spectrum, and as such does not require axial scanning, but is not full-field and therefore lateral scanning is necessary. Meter-scale OCT depth ranging with 15 micron axial resolution has recently been achieved [4]. DHM is a technique that does not use scanning because it reconstructs the complete wavefield. The acquisition time is therefore short compared to other techniques while having the possibility to attain sub-nanometer axial resolution. When the reconstructed wavefield is in focus, the phase of the wavefield is linear to the height of the sample. The reconstructed phase is defined modulo 2π and therefore the height that can be reconstructed in reflection mode without ambiguity is half a wavelength [5]. This can be overcome using phase unwrapping, however, this does not work if abrupt steps greater than half a wavelength are present.

Furthermore, for rough objects the wavefront becomes too disturbed to calculate the topography. Localization of rough objects with digital holography has also been demonstrated using a statistical fringe processing technique [6]. In this technique, the object is illuminated from two angles, a digital hologram is captured for each angle, and the two wavefronts are reconstructed at a number of reconstruction distances near the object plane. At each reconstruction plane, a statistical algorithm is applied to the phase difference map for object localization up to a precision of 250 microns. FVM on the other hand is not an interferometric technique. It uses axial focus scanning and exploits the limited depth of focus of the objective lens to extract topology information from focus variation quantified with a focus metric, provided the surface is optically rough [7]. The axial precision of this technique depends on the magnification used; a 2.5x and 100x magnification for example lead to micron and nanometer range precision respectively [8]. Just like in WLI, the acquisition time is relatively long due to the requirement of axial scanning. For any of these techniques there exists trade-offs between acquisition time, sample properties (e.g. roughness and discontinuities), the presence of scanning, depth range, and axial resolution. Depth from focus digital holography (DFF-DH) attempts to combine the short acquisition time of digital holography (scanless imaging) with the ability to reconstruct topographies with large discontinuities or rough surfaces. In contrast to ordinary imaging where the focus is varied by changing the position of the lens, in DH the in-focus image can be calculated at any depth plane. The DFF-DH method is an image processing approach that estimates the surface location from the optimum of a focus metric calculated from the digitally reconstructed image. For 3D objects the image plane depends on the distance of every part of the object to the camera. By reconstructing the image of the object at different depths, the degree of focus of a particular region in the image reconstruction (calculated with a focus metric) encodes the depth of the object [9]. Because one can reconstruct the complete wavefield at any depth from a single digitally captured hologram, this method does not need lateral or axial scanning and has no fundamental limit regarding the depth range that can be measured other than the coherence length of the light source. DFF was first used within the context of digital holography by Ma et al. (2004) [10], who recovered object depth for every part of the object in this way from a digital hologram. A similar approach was also used for extended focus imaging by McElhinney et al. (2008) [11]. While Tachiki et al. (2008) measured an axial accuracy of a centimeter [9], the theoretical understanding of the axial resolution and its fundamental limits remains largely unknown. In this paper we show how the depth resolution of DFF-DH depends on sample properties and on experimental setup parameters. Furthermore, we show experimentally that the precision in the axial direction can be brought down to the 100 micron range in a basic DH setup without any magnification. In the next section, we first give an overview of the basic principles of DFF-DH and a theoretical framework to analyze the precision. Subsequently, we compare our framework with simulations where we show that sub-mm resolution is possible. In the results section we experimentally demonstrate sub-mm axial in DFF-DH.

2.3. THEORY

2.3.1. DEPTH FROM FOCUS DIGITAL HOLOGRAPHY

In digital holography the image is numerically calculated from an interferogram, instead of it being formed optically with a lens. For an explanation of the basic principles of digital holography, we refer the reader to Schnars and Jueptner (2005) [12]. Digital holography suffers from a limited depth of field just like most other imaging systems. If the reference wave $R(x, y)$ is a plane wave, as we will assume throughout this paper, then the reconstruction distance z_r equals the recording distance z_0 and the reconstructed image appears in focus [13]. Reconstructing the image at other distances than z_0 leads to defocus blurring of the image due to the limited depth of field. The degree of focus in the image depends on the reconstruction distance and therefore encodes the distance of the object to the sensor. Since the degree of focus is at its' maximum when z_r=z_0, one needs to quantify the degree of focus with a focus metric and find the optimum value as a function of the reconstruction distance. For each pixel in the object image we can repeat this process and calculate its' distance to the sensor plane z_0 to obtain a height map of the object. The degree of focus in the image as a function of reconstruction distance z_r depends on the numerical aperture (NA) of the imaging system. In DH, the NA is inversely proportional to the recording distance and proportional to the dimensions of the sensor.

2.3.2. FOCUS METRIC DEFINITION

The degree of focus is quantified using image based metrics. These metrics are calculated from the image and have their maximum when the image is in focus, and decrease rapidly when the image is out of focus. Different focus metrics exist, see for example Tian et al. (2007) for an overview [14]. Image variance is a focus metric that is simple to calculate, and has been proven to be a good depth measure [15]. The variance of a digital image I of $n \times m$ pixels is given by:

$$\mathrm{var}(I) = \frac{1}{NM} \sum_{i=1}^{N} \sum_{j=1}^{M} (I(i,j) - \overline{I})^2 , \tag{2.1}$$

where $\overline{I}$ is the mean intensity of the image. In order to derive an analytic model for the variance as a function of reconstruction distance, we will use a continuous form which is given by

$$\mathrm{var}(I) = \int\int (I(x,y) - \mu)^2 \mathrm{d}x\,\mathrm{d}y , \tag{2.2}$$

where μ is the mean of the image and is given by

$$\mu = \int\int I(x,y) \mathrm{d}x\,\mathrm{d}y . \tag{2.3}$$

2.3.3. DEPTH FROM FOCUS PRECISION ANALYSIS

To obtain a theoretical description, we neglect the details of surface scattering processes, following the assumption of Nikolaev et al. (2016) in their linear theory approach to FVM

[7], and consider the object surface to be a perfect plane with a reflection coefficient that has a random distribution. The object will be considered to have a reflection coefficient that has a "white" frequency distribution, i.e., all spatial frequencies have equal power. Due to the linearity of the digital holographic imaging process with respect to the object field, the reconstructed object field is described by propagation of every spatial frequency of the object into the image space. For each spatial frequency in the object, the focus curve is periodic due to the Talbot effect, and we will term such a focus curve a Talbot curve. In our specific case, it turns out that the focus curve for the object is a sum of the individual Talbot curves for all spatial frequencies. In order to keep the expressions concise we consider a one dimensional input, although a generalization to two dimensions is straightforward. We first derive an expression for the image of a reflecting planar object with a single spatial frequency and random phase at recording distance z_0 as input to the holographic imaging system, which we reconstruct at reconstruction distance z_r. Neglecting the finite extent of the aperture, we consider an object described by the field reflection

$$t_n = \frac{1}{2}[1 + m\cos(2\pi n\xi/L + \phi_n)], \tag{2.4}$$

where ϕ_n is a random phase term, n/L is the spatial frequency and m is an amplitude factor and ξ is the lateral spatial coordinate in the input plane. In principle n can be any number, although in practice it is an integer value due to discrete sampling of the detector. The reconstructed holographic wavefield is calculated by propagating the input wavefield to the hologram plane, and then to the reconstruction plane, using the transfer function Fresnel diffraction method approach according to the treatment of Goodman (1996) [16]. The resulting reconstructed wavefield is

$$U_n(\xi, z_r) = \frac{2 + 2me^{-\frac{i\pi\lambda n^2(z_0+z_r)}{L^2}}\cos\left(\frac{2\pi n\xi}{L} + \phi_n\right)}{4N}, \tag{2.5}$$

where N is the total number of spatial frequencies captured by the imaging system. The intensity of the reconstructed wavefront is then

$$\begin{aligned} I_n(\xi, z_r) = \frac{1}{4N^2}\left(m\cos\left(\frac{2\pi n\xi}{L} + \phi_\mathrm{n}\right) + 2\cos\left(\frac{\pi\lambda n^2(z_0+z_r)}{L^2}\right)\right) \\ m\cos\left(\frac{2\pi n\xi}{L} + \phi_n\right) + \frac{1}{4N^2}. \end{aligned} \tag{2.6}$$

This reduces to $|t_n|^2$ for reconstruction distances

$$z_r = -z_0 + \frac{2L^2k}{\lambda}, \tag{2.7}$$

which means that the input grating is replicated at fixed distances for an integer value of k, also called "self-imaging". This occurs for periodic inputs in general and is a manifestation of the Talbot effect [16] appearing in holographic reconstruction. The variance for one spatial frequency as a function of reconstruction distance is subsequently found by

calculating the integral in one dimension ((2.2)) over the integration range 0 to L, which yields

$$\mathrm{var}_n(z_r) = a + b\cos\left(\frac{2\pi\lambda n^2(z_0+z_r)}{L^2}\right), \tag{2.8}$$

where m is assumed to be equal to one, and

$$a = \frac{9L\left(2L^2-4L+3\right)}{128N^4}, \tag{2.9}$$

and

$$b = \frac{L}{16N^4}. \tag{2.10}$$

For every spatial frequency n/L the variance is thus periodic as a function of reconstruction distance z_r. For this reason we will refer to such a curve as a Talbot curve. We now assume that the object is composed of many spatial frequencies. Since in an experimental setting the spatial frequencies are discretely sampled, we describe the reflection of the object as

$$t_N = \frac{1}{N}\sum_{n=1}^{N}\frac{1}{2}[1+m\cos(2\pi n\xi/L+\phi_n)]. \tag{2.11}$$

According to the superposition principle, the reconstructed field intensity is

$$I_N(\xi,z_r) = \left|\sum_{n=1}^{N} U_n(\xi,z_r)\right|^2 \tag{2.12}$$

$$= \sum_{n=1}^{N}|U_n|^2 + \sum_{n=1}^{N}\sum_{m=1}^{N} U_nU_m^*(1-\delta_{n,m}). \tag{2.13}$$

Due to the random phase term ϕ_n, the first term in (2.13) and the last term are independent random variables. Using the property that $\mathrm{var}(a+b) = \mathrm{var}(a)+\mathrm{var}(b)$ if a and b are independent random variables, we can write the variance of the reconstructed field intensity as

$$\mathrm{var}(I_N) = \sum_{n=1}^{N}\mathrm{var}\left(|U_n|^2\right) + \mathrm{var}\left(\sum_{n=1}^{N}\sum_{m=1}^{N} U_nU_m^*(1-\delta_{n,m})\right). \tag{2.14}$$

We then have:

$$\sum_{n=1}^{N}\sum_{m=1}^{N} U_n U_m^*(1-\delta_{n,m}) = \frac{1}{4N^2}\sum_{n=1}^{N}\sum_{m=1}^{N}\cos\left(\frac{\pi\lambda(n^2-m^2)(z_0+z_r)}{L^2}\right)\cos\left(\frac{2\pi n\xi}{L}+\phi_n\right)\cdot \cos\left(\frac{2\pi m\xi}{L}+\phi_m\right)(1-\delta_{n,m})+ \frac{N-1}{2N^2}\sum_{n=1}^{N}\cos\left(\frac{\pi\lambda n^2(z_0+z_r)}{L^2}\right)\cos\left(\frac{2\pi n\xi}{L}+\phi_n\right) + \frac{N(N-1)}{4N^2}. \quad (2.15)$$

Using the independence property for the variance, we obtain for the variance of this expression

$$\mathrm{var}(I_n) = \mathrm{var}\left(\sum_{n=1}^{N}\sum_{m=1}^{N} U_n U_m^*(1-\delta_{n,m})\right) = \mathrm{var}\left(\sum_{n=1}^{N}\sum_{m=1}^{N}\cos\left(\frac{\pi\lambda(n^2-m^2)(z_0+z_r)}{L^2}\right)\cos\left(\frac{2\pi n\xi}{L}+\phi_n\right)\cos\left(\frac{2\pi m\xi}{L}+\phi_m\right)\frac{(1-\delta_{n,m})}{2N^2}\right)+ \mathrm{var}\left(\frac{N-1}{2N^2}\sum_{n=1}^{N}\cos\left(\frac{\pi\lambda n^2(z_0+z_r)}{L^2}\right)\cos\left(\frac{2\pi n\xi}{L}+\phi_n\right)\right). \quad (2.16)$$

The first term is equal to

$$\mathrm{var} = \frac{L}{32N^4}\sum_{n=1}^{N}\sum_{m=1}^{N}\cos\left(\frac{2\pi\lambda(n^2-m^2)(z_0+z_r)}{L^2}\right)+1. \quad (2.17)$$

The last term is equal to

$$\mathrm{var} = \frac{L(N-1)^2}{16N^4}\sum_{n=1}^{N}\left(\cos\left(\frac{2\pi\lambda n^2(z_0+z_r)}{L^2}\right)+1\right). \quad (2.18)$$

From an analogy with Fourier analysis we can observe that the peak width of $\sigma^2(I_N)$ is limited by the higher spatial frequencies caused by the n^2 terms in the argument of the cosine, and not by the difference terms n^2-m^2 which correspond to lower spatial frequencies. We thus approximate the variance curve as a linear sum of the Talbot-curves resulting from the n^2/L^2 frequencies in the variance curve:

$$\mathrm{var}_N(z_r) = A + \sum_{n=1}^{N} B\cos\left(\frac{2\pi\lambda n^2(z_0+z_r)}{L^2}\right), \quad (2.19)$$

where

$$A = N\left(a+\frac{L(N-1)^2+L}{16N^4}\right), \quad (2.20)$$

and

$$B = \frac{L(N-1)^2 + L}{16N^4}. \tag{2.21}$$

Equation 2.19 provides a physical understanding of the width of the focus curve. The sum of cosines gives rise to a peak at $z_r = -z_0$, the virtual image plane. For larger N, either because of a larger numerical aperture or a larger number of contributing spatial frequencies in the input, the peak width becomes smaller. The result in (2.19) gives a limit for the precision that can be achieved by depth from focus digital holography in terms of the peak width. In Figure 2.1, the focus curve of (2.19), for z_0=70.9 mm (real image), λ=633 nm, L=6.7 mm and N=1024, is plotted as a function of reconstruction distance z_r. In the preceding analysis it has been assumed that the object has an ideal flat power spectrum, and the phases ϕ_n for spatial frequencies n/L were assumed to be statistically independent (ideal white noise input). For a real object the spatial frequency distribution of the object may be less ideal leading to less terms contributing to the summation in 2.19 and therefore resulting in a wider peak. Finally, the summation is limited by the numerical aperture and sampling of the imaging system. The numerical aperture of the system limits the highest spatial frequency to reach the sensor, while the pixel pitch of the sensor limits the highest spatial frequency that can be sampled properly. At the critical recording distance, the maximum amount of spatial frequencies is imaged without aliasing. This distance is given by $z_{crit} = N_{pix}\Delta\xi^2/\lambda$ where N_{pix} is the number of sensor pixels, $\Delta\xi$ is the pixel pitch and λ the recording wavelength. For an amplitude grating with spatial frequency n/L, the angle under which the first diffraction order propagates from the normal is

$$\sin(\theta) = \frac{\lambda n}{L}. \tag{2.22}$$

The numerical aperture is determined by the sensor dimension $N_{pix}\Delta\xi$ and recording distance z_0 and limits the maximum diffraction angle θ_{max} that can be imaged by the system, according to

$$\theta_{max} = \tan^{-1}\left(\frac{N_{pix}\Delta\xi}{2z_0}\right), \tag{2.23}$$

which follows from the imaging geometry.
Combining the last two equations and solving for the maximum spatial frequency $n/L = N_{max}/L$, we find that

$$\frac{N_{max}}{L} = \sin\left(\tan^{-1}\left(\frac{N_{pix}\Delta\xi}{2z_0}\right)\right)\frac{1}{\lambda}. \tag{2.24}$$

Using the critical sampling distance $z_0 = z_{crit}$ this becomes

$$\frac{N_{max}}{L} = \frac{1}{2\Delta\xi\sqrt{\frac{\lambda^2}{4\Delta\xi^2}+1}} \approx \frac{1}{2\Delta\xi}. \tag{2.25}$$

Hence, the summation in (2.19) is limited to the term with the maximum spatial frequency N_{max}/L that is imaged with the system. At the critical sampling distance, this is equal to the Nyquist frequency and in the summation of (2.19) limits the DFF-DH minimum peak width.

2.4. DIGITAL HOLOGRAPHY SIMULATIONS

We validate the analytic focus curve model of (2.19) as a sum of Talbot curves by comparing it to the well-known method of Fresnel diffraction calculations, namely the transfer function method, . We implemented the transfer function methodcode in MATLAB 2016, we refer the reader to the work of Voelz (2011) [17] for more information. The input image in the simulation is given by (2.11), where the input object support L is 200 pixels, the number of pixels in the recording plane is N=1000, the number of unique spatial frequencies in the input image is $L/2-1$, the wavelength λ=633 nm, the pixelsize $\Delta\xi$=6.45 micrometer and the recording distance z_0 at $N\Delta\xi^2/\lambda$ (critical recording distance). These are parameters used in a typical experimental digital holography realization.

The digital hologram is calculated and the real image is reconstructed in 400 steps over the distance z_0 - 2 mm to z_0 + 2 mm. The variance of the reconstructed image is calculated at each step. The variance as a function of reconstruction distance is shown in Figure 2.1.

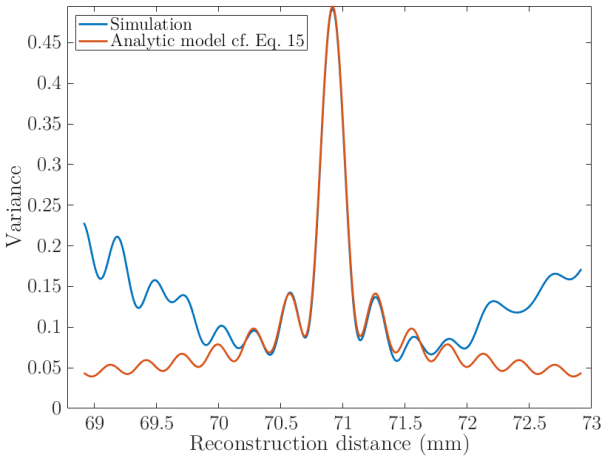

Figure 2.1: Comparison between the focus (variance) curves resulting from the Fresnel diffraction simulation (blue) and the analytic model Eq. 2.19 (red). The difference between the two calculations is due to the finite aperture used in the simulation.

Since there is amplitude scaling in the diffraction calculation that is not present in the analytic model, the simulated focus curve is scaled along the vertical axis to match the peak variance of the analytic model. The simulated focus curve describes the analytic model of (2.19) well around the center $z_r = z_0$, and deviates towards the edges due to finite aperture effects that occur in the simulation, but are not accounted for in the analytic model. Both approaches lead to the same focus curve peak-width of approximately 450 microns, indicating the possibility of sub-millimeter axial resolution with DFF-DH without magnification.

2.5. MATERIALS AND METHODS

2.5.1. DIGITAL HOLOGRAPHY SETUP

The digital holography setup is shown in Fig. 2.2 and consists of a Michelson interferometer with the light illuminating the object normal to the surface. The light source is a HeNe laser with a wavelength of 633 nm and an output power in the order of 3 mW. Two lenses (Thorlabs, LD2568 and LA1979) are used to expand and collimate the illuminating laser beam respectively to a width (FWHM) of approximately 15 mm, besides that no lenses or objectives are used in the imaging process. A shearing interferometer (Thorlabs, SI254) is used to assure proper collimation of the reference beam, so that the distance in reconstruction (virtual) space equals the physical recording distance. The object is placed approximately 70 mm away from the sensor plane. The mirror in the reference arm is mounted onto a piezoelectric transducer controlled by a computer for phase-shifting the digital hologram, where we capture four holograms with a phase shift of $\pi/2$ of the reference beam between each subsequent hologram. From a linear combination of these holograms a complex hologram is formed where the zeroth and out of focus conjugate order are removed[18]. In this way we can use the full image plane and maximize the lateral resolution in the reconstructed image. We use a pellicle beam splitter (Thorlabs, BP233) in order to avoid ghost-images in the reconstructions (that resulted in degraded reconstructions in earlier research on DFF-DH [9]). Due to the sensitivity of the pellicle beamsplitter membrane to vibrations from sound or airflow, the setup is enclosed in a box in order to minimize movement of the membrane. A variable neutral density filter is placed between the beamsplitter and the piezo mounted mirror and right after the laser aperture in order to control saturation of the camera and the ratio of the intensity between the reference and the object beam, which is close to 1. The digital holograms are captured by a CCD camera (ORCA ER, Hamamatsu) with 1344 × 1024 square pixels with a pixel size of 6.45 micrometer and acquisition speed of approximately 10 frames a second.

2.5.2. SAMPLE PREPARATION AND CHARACTERIZATION

We use a brass reflector with four different step heights (squares) separated at heights approximately 200 microns apart as a test target to demonstrate sub-mm axial resolution. The sample surface is made rough by briefly sandblasting the object. The total area of the square sample is 25 mm^2. For a reference measurement of the surface height topology we use a white light interferometer (WLI, Bruker ContourGT-K). We used the smallest magnification available on the WLI, which was 2.5×. Due to the field of view (2 mm) being significantly smaller than the lateral sample dimensions (5 mm), stitching is necessary which is done automatically with the accompanied $Vision$ software. Tilt is corrected for by fitting a plane to one of the four surfaces and correcting the entire profile for this tilt. The acquisition time for the full surface at the lowest magnification is in the order of 30 min. The roughness parameters S_a (average roughness) and S_q (root mean square roughness) are measured with WLI for the sample and are given by 3.6 and 11.6 micrometer, respectively.

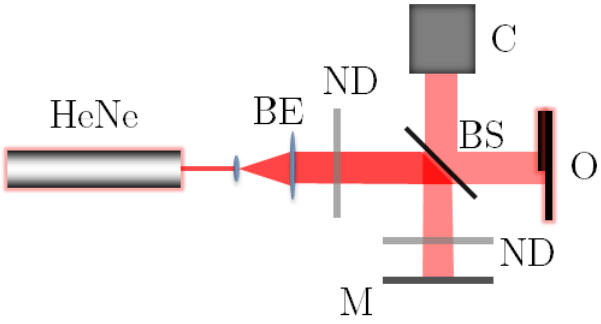

Figure 2.2: Michelson interferometer setup for acquiring the digital holograms. HeNe=HeNe laser (633 nm), BS=pellicle beam-splitter, C=CCD camera (1344x1024 pixels), M=piezo mounted mirror and O=object, L=lens, ND=variable neutral density filter.

2.5.3. DIGITAL HOLOGRAPHIC RECONSTRUCTION

Even though the lateral sample dimensions are smaller than the sensor and thus the transfer function approach can be used, there is the possibility of the sample holder, which extends to beyond the sensor plane, appearing in the reconstructed image. For this reason reconstruction of the digital holograms was performed using the S-FFT method [19] since this does not restrict the reconstruction plane to the dimensions of the sensor. Since noise appears as high frequency information in the reconstructed images, we apply a spatial Gaussian filter to each reconstructed image. We found that a standard deviation σ of approximately 0.7 pixels gave the most accurate reconstructions. We calculate the focus metric per pixel for each reconstruction distance by taking a window of N by N pixels around the center pixel. A trade-off exists in DFF-DH between the axial resolution and the window size and thus the lateral resolution [9]. We used a window size of 61 by 61 pixels (0.2 mm^2) and calculated the variance of the windowed image over reconstruction distances $z_r = z_0$ - 2 mm to z_0 + 2 mm. The reconstruction distance where the variance peaks for a particular pixel is our estimate for the distance from the recording plane to the object pixel. Finally, we corrected for surface tilt of the entire object with respect to the recording plane by fitting a plane to two diagonally opposite surfaces and calculating the average tilt. This tilt is subtracted from the actual distances. The time for the algorithm to calculate a complete depth image on a quad core computer is around half a minute.

2.6. RESULTS

Figure 2.3 a) and b) show the reconstructed DH intensity images at reconstruction distances $z_r = 69.8$ and $z_r = 70.4$ mm respectively. At $z_r = 69.8$ mm, the lower right quadrant is in focus and shows the fine details of the surface, whereas the upper left quadrant has a blurred appearance because it is out of focus. At $z_r = 70.4$ mm the opposite occurs.

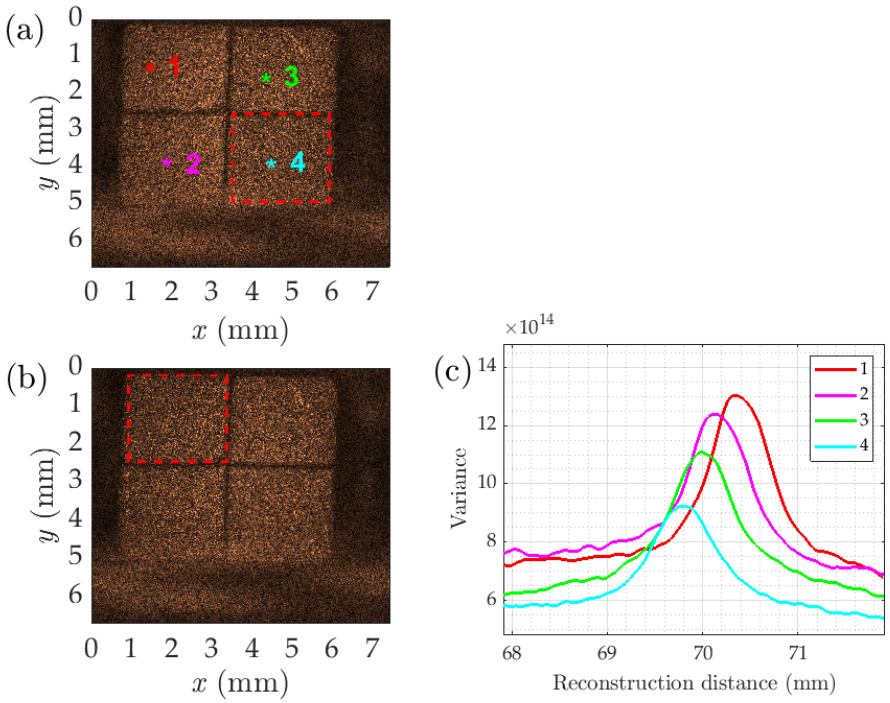

Figure 2.3: Reconstructed intensity image of the brass reflector object at $z_r = 69.8$ (a) and $z_r = 70.4$ mm (b). For (a) the lower right square is in focus, for (b) the upper left square is in focus. c) DFF curves obtained from the experimental data at the points indicated in (a) at different planes.

Figure 2.3 (c) shows focus metric curves obtained from the experimental data at the locations indicated in Fig. 2.3 (a). The experimental focus curve has a full width at half maximum of approximately 750 microns, which is significantly broader than the width of the simulated curve in Fig. 2.1. We attribute this to the fact that the frequency content of the object is limited and the object plane was slightly tilted with respect to the sensor plane. In that sense, the focus curve in Fig. 2.1 represents a limiting case with perfect parallel orientation and uniform spatial frequency power spectrum in the input image. The spatial frequency content of the experimental input is estimated by taking the Fourier transform of the optimal in focus intensity image. The logarithm of the power spectrum in Fig. 2.5 shows that indeed the power spectrum is not flat, but instead shows a significant drop off in power for high spatial frequencies. Based on the optimum of the focus curves, the surface is reconstructed as shown in Fig. 2.4.

To obtain an estimate of the accuracy of our approach we determined the distribution of reconstructed depth values for all pixels in the image. The result is shown in Fig. 2.6 as a histogram together with a comparison of the distribution obtained with the white light interferometer. Good agreement is obtained with the DFF-DH method shown here. Assuming that the WLI data represents the actual height distribution of the object we estimate that from the width of DFF-DH histogram our method has a depth

resolution of approximately 100 microns.

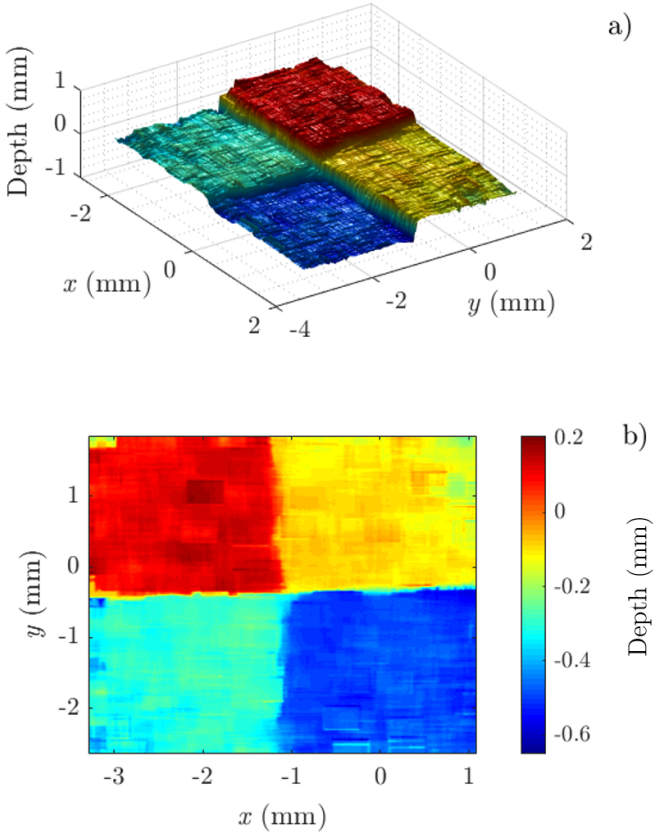

Figure 2.4: (a) Reconstructed DFF-DH depth map of the brass reflector object (b) and top view.

2.7. DISCUSSION

We presented sub-millimeter DFF-DH imaging of surface topography without the use of magnifying or lateral scanning optics. In the theoretical analysis presented in this paper it is assumed that all spatial frequencies in the object surface are equally present with randomly distributed phases. This results in a lower limit of the depth resolution of DFF-DH systems in terms of the peak width of the focus curve.

The focus curves obtained from experimental data do not show the oscillating behavior in the sidelobes of the curve. Moreover, the experimental focus curve was significantly broader than the theoretical limit. Both effects are likely caused by the fact that the object plane was not perfectly parallel to the camera, but instead is slightly tilted, and the spatial frequency spectrum of the object does not correspond to a white noise signal.

On the other hand, the optimal depth is determined from the maximum value of the

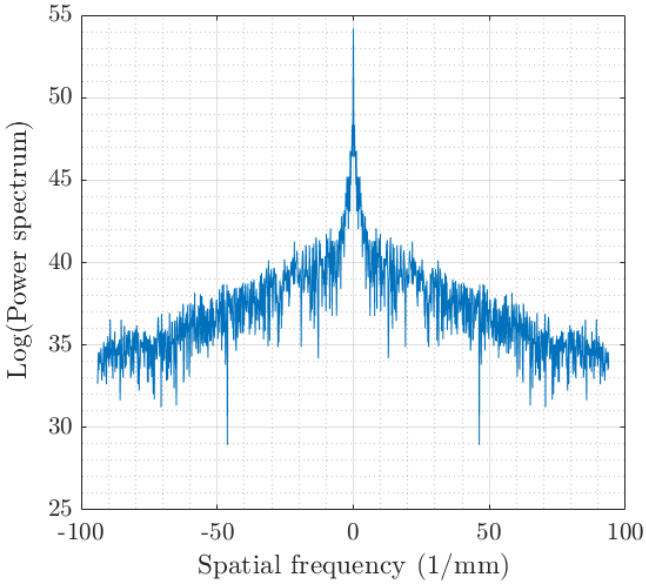

Figure 2.5: Cross section along the vertical axis of the logarithm of the object image power spectrum when reconstructed in focus along x=4 mm in Fig. 2.3.

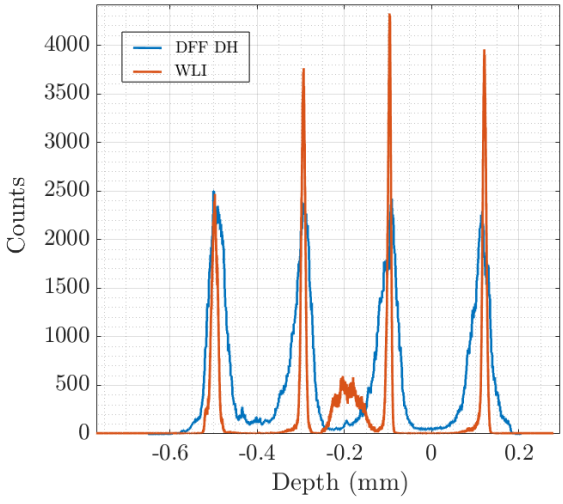

Figure 2.6: Histogram of the distribution of depth values from the DFF-DH reconstruction of Figure 2.4 (blue), together with the depth distribution of the reference WLI measurement (red).

peak which is much better defined than the peak width. Since the DFF-DH method in this paper relies only on finding the maximum, this partially compensates for the broadening of the focus curve in the experiment; the measured width is approximately 750 microns, while the DFF depth resolution is around 100 microns. As a result the surface height estimation precision is significantly below the width of the focus curves. Although using the maximum value of the focus metric to estimate the surface position has a physical basis, it does not utilize other information of the focus curve, such as the peak width and shape, to improve the depth estimate. Fitting a polynomial or point spread function curve, as applied in FVM ([8], could further improve the axial resolution.

While this paper mainly was dedicated to analyzing the axial resolution of DFF-DH, lateral resolution also plays an important role in applications. DFF-DH is based on an area of pixels to calculate the focus metric at the center pixel, thus smoothing the depth map in the transversal direction. In principle there is a relation between the number of pixels needed for obtaining a depth estimate and the axial precision, thereby resulting in an intrinsic trade-off between axial and lateral resolution. We observed that a window size of 61 pixels gave good results. Using more sophisticated methods, mentioned earlier to estimate the depth, will likely enable the use of smaller window sizes.

In our configuration, four digital holograms were acquired for phase shifting digital holography. This was to make full use of the image plane, however this is not a strict requirement. A setup with a larger sensor can produce equivalent results from a single hologram capture if the reconstructed diffraction orders are properly separated spatially in the reconstruction plane.

The results in this work were obtained with a basic form of DFF-DH, without using additional magnifying optics. Magnifying optics can be incorporated into the DFF-DH system in order to improve lateral and axial resolution, which goes at the expense of the field of view. Since in digital holography lateral resolution depends also on the aperture of the sensor and indirectly on the pixel size, resolution in DFF-DH also can be improved without magnifying optics by using a larger sensor while retaining the field of view. We envision this technique can be useful for characterizing objects in art, process control and computer vision, or in general when absolute distance measurements are needed in a very short acquisition time.

2.8. CONCLUSIONS

We demonstrated that the DFF curve as a function of reconstruction depth can be approximated by the sum of Talbot curves for every spatial frequency. Analytic theory and numerical simulation indicated that the axial precision in terms of the peak width can be brought down to well below the millimeter range using a basic digital holography setup without scanning, imaging optics or magnification. Sub-millimeter depth resolution was experimentally demonstrated in a DFF-DH set-up using a rough reflecting step-profile where our method was able to discriminate between layers that were approximately 200 micrometer apart. This is approximately 100 times better than what was previously demonstrated in DFF-DH [9].

REFERENCES

[1] R. Leach, *Optical Measurement of Surface Topography* (Springer Berlin Heidelberg, 2011).

[2] P. de Groot, *Phase shifting interferometry,* in *Optical Measurement of Surface Topography*, edited by R. Leach (Springer, Heidelberg, 2011) Chap. 8, pp. 167–186.

[3] P. de Groot, *Coherence scanning interferometry,* in *Optical Measurement of Surface Topography*, edited by R. Leach (Springer, Heidelberg, 2011) Chap. 9, pp. 187–208.

[4] Z. Wang, B. Potsaid, L. Chen, C. Doerr, H.-C. Lee, T. Nielson, V. Jayaraman, A. E. Cable, E. Swanson, and J. G. Fujimoto, *Cubic meter volume optical coherence tomography,* Optica **3**, 1496 (2016).

[5] J. K. Tristan Colomb, *Digital holographic microscopy,* in *Optical Measurement of Surface Topography*, edited by R. Leach (Springer, Heidelberg, 2011) Chap. 10, pp. 209–235.

[6] T. J. T. Abregana and P. F. Almoro, *Object localization using the statistical behavior of volume speckle fields,* Optical Engineering **55**, 121720 (2016).

[7] N. Nikolaev, J. Petzing, and J. Coupland, *Focus variation microscope: linear theory and surface tilt sensitivity,* Appl. Opt. **55**, 3555 (2016).

[8] F. Helmli, *Focus variation instruments,* in *Optical Measurement of Surface Topography*, edited by R. Leach (Springer, Heidelberg, 2011) Chap. 7, pp. 131–166.

[9] M. L. Tachiki, M. Itoh, and T. Yatagai, *Simultaneous depth determination of multiple objects by focus analysis in digital holography,* Appl. Opt. **47**, D144 (2008).

[10] L. Ma, H. Wang, Y. Li, and H. Jin, *Numerical reconstruction of digital holograms for three-dimensional shape measurement,* Journal of Optics A: Pure and Applied Optics **6**, 396.

[11] C. P. McElhinney, B. M. Hennelly, and T. J. Naughton, *Extended focused imaging for digital holograms of macroscopic three-dimensional objects,* Appl. Opt. **47**, D71 (2008).

[12] U. Schnars and W. Jueptner, *Digital holography,* in *Digital Holography: Digital Hologram Recording, Numerical Reconstruction, and Related Techniques* (Springer Berlin Heidelberg, Berlin, Heidelberg, 2005) pp. 41–69.

[13] J. chang Li and P. Picart, *Digital holography,* in *Digital Holography* (John Wiley Sons, Inc., 2013) pp. 165–236.

[14] Y. Tian, K. Shieh, and C. F. Wildsoet, *Performance of focus measures in the presence of nondefocus aberrations,* J. Opt. Soc. Am. A **24**, B165 (2007).

[15] M. Subbarao and G. Surya, *Depth from defocus: A spatial domain approach,* International Journal of Computer Vision **13**, 271 (1994).

[16] J. Goodman, *Introduction to Fourier Optics*, 2nd ed. (MaGraw-Hill, 1996).

[17] J. Breckinridge and D. Voelz, *Computational Fourier Optics: A MATLAB Tutorial*, SPIE Press monograph.

[18] I. Yamaguchi and T. Zhang, *Phase-shifting digital holography,* Opt. Lett. **22**, 1268 (1997).

[19] N. Verrier and M. Atlan, *Off-axis digital hologram reconstruction: some practical considerations,* Appl. Opt. **50**, H136 (2011).

3

LARGE SCALE ODT

3.1. ABSTRACT

In this work we demonstrate large scale high sensitivity optical diffraction tomography (ODT) of zebrafish. We make this possible by three improvements. First, we obtain a large field of view while still maintaining a high resolution by using a high magnification over numerical aperture ratio digital holography set-up. With the inclusion of phase shifting we operate close to the optimum magnification over numerical aperture ratio. Second, we decrease the noise in the reconstructed images by implementing off-axis sample placement and numerical focus tracking in combination with the acquisition of a large number of projections. Although both techniques lead to an increase in sensitivity independently, we show that combining them is necessary in order to make optimal use of the potential gain offered by each respective method and obtain a refractive index (RI) sensitivity of $8 \cdot 10^{-5}$. Third, we optimize the optical clearing procedure to prevent scattering and refraction to occur. We demonstrate our technique by imaging a zebrafish larva over 13 mm^3 field of view with 4 micrometer resolution. Finally, we demonstrate a clinical application of our technique by imaging an entire adult cryoinjured zebrafish heart.

3.2. INTRODUCTION

Three dimensional (3D) optical imaging is used in many areas of biology and medicine as is evidenced by the multitude of 3D imaging modalities that have been developed. Advantages of such techniques include the capability of virtual instead of physical sectioning and the possibility of quantitative 3D analysis in the original geometry. However, for many 3D imaging techniques the measurement method is not sensitive to an inherent contrast in the sample. Instead, imaging is performed with the relevant features in the sample labeled, which requires extra sample preparation and biases the detection to only the labelled structures. For example, in the study of heart regeneration in zebrafish after cryoinjury, clinicians must do sectioning of the sample, fixation, staining and finally manually estimate the injured volume relative to that of the total heart[1]. Therefore, to image label free in 3D there has been an increased interest in recent years in 3D imaging of unlabeled samples making use of intrinsic contrast present in the sample[2][3][4]. One such contrast is the refractive index (RI) variation in the sample, which is often feature specific and provides information about the global structure in the sample (in contrast to molecular specific techniques). Optical diffraction tomography (ODT), sometimes also referred to as phase tomography, images the RI contrast by measuring the complex wavefront of the transmitted object wave. and is used to make quantitative images of the 3-D RI distribution of transparent samples. This is done by acquiring phase images of a sample from different angles, and combining these in a 3D reconstruction of the sample by using a back propagation algorithm.

Closely related to ODT is optical projection tomography (OPT), an established method to reconstruct 3-D fluorescence emission or attenuation in a sample. Although tomographic acquisition and reconstruction have common ground in both techniques, the two fields have been operating independently in some important respects. For example, in both OPT and ODT research has focused on dealing with diffraction from out of focus planes. Since OPT and ODT acquire light intensity and complex wave field information,

respectively, the ways in which diffraction is tackled are completely different. In OPT diffraction can be corrected through image deconvolution[5] or point-spread function based reconstruction [6]. This is quite different from ODT where diffraction is accounted for in the reconstruction algorithm[7] or where the wavefield is digitally refocused [8].

Another example is the striking difference in the size scale at which ODT is applied compared to that in OPT. It is common in the field of OPT to image both small scale samples like cells[9] as well as large scale biological samples, like zebrafish (adult and embryo's)[10][11] or mouse brains [12], and OPT is considered especially useful in such millimeter scale samples [13]. ODT of biological tissue is mainly focused on small scale imaging and applied to samples in the tens of microns size range, such as cells[14][15] and (plant) fibers [16]. This is caused by the fact that on the one hand ODT relies on RI differences inside the sample to be present for image formation. On the other hand ODT requires that RI differences are sufficiently small in order to prevent a change in direction of the rays passing through the object or severe aberrations of the wavefront to occur, both which inhibit accurate reconstruction of the object wavefield. In larger samples, even small changes in refraction can cause a major lateral displacement of the rays hitting the detector or cause large wavefront aberrations due to the larger optical path length through the object. Hence, even for small RI differences, deformation of the phase projection occurs, with a resulting poor imaging reconstruction as a result. Consequently, for large scale ODT of biological tissues, the RI variation must be small enough in order to minimize these effects, but the imaging method must be sensitive enough to still detect this RI variation in the wavefront and allow for sufficient contrast in the reconstructed image. Since this combination is challenging to obtain it is not surprising that attention in ODT research has mainly focused on small samples which are inherently transparent, like biological cells or (plant) fibers, that are in the range of $10-30$ μm in diameter, and thus do not cause significant beam deviation and wavefront aberrations when light propagates through the sample.

A recent exception is ODT applied to a large scale synthetic lens object with high phase sensitivity [17]. However, in this case the surrounding index matching liquid had to be very precisely matched to the RI of the lens. This kind of precise index matching only works for homogeneous samples. An alternative is to use optical clearing of the sample and image the sample in the clearing liquid. Optical clearing aims to homogenize the RI in a sample in order to increase imaging depth and image quality [18]. However, optical clearing causes RI differences to be (very) small, necessitating high sensitivity and therefore a low noise level in the reconstruction to obtain high quality images. Although the issues of deformation of the projections (due to ray displacement) and severe aberrations of the wavefront could then be solved, the challenge is then to accurately image the remaining RI contrast accurately.

In this paper, we demonstrate, to our knowledge for the first time, that high contrast and high resolution 3D refractive imaging of large scale biological samples can be done with phase tomography without extensive index matching procedures using the following steps:

- large scale high resolution imaging using a large image sensor and phase shifting digital holography to make full use of the spatial frequency bandwidth of the system.

- high sensitivity RI detection through off-axis sample placement combined, with numerical focus tracking during rotation, and acquisition of a large number of projections.
- minimization of scattering and refraction by using a passive optical clearing procedure common in OPT.

We demonstrate our large scale high resolution approach with measurements on a 3 day old zebrafish larva and an adult zebrafish heart. Here, ODT adds an additional type of contrast (RI) to large scale organic tissue imaging not traditionally accessible in OPT, which allows for imaging of structures such as eyes, brains and yolk sack using intrinsically present RI contrast. Finally, we demonstrate a clinically relevant application where we image regenerating zebrafish heart tissue after damage based on RI contrast and estimate the relative volume of the injured tissue. This can eliminate the need for the current labour intensive procedure of sectioning and staining of the heart[19].

3.3. MATERIALS AND METHODS

3.3.1. ACQUISITION OF PHASE PROJECTIONS

In ODT, the scattered field is recorded from multiple angles using digital holography. The digital holography setup is shown in Fig. 3.1 and consists of a Mach-Zehnder interferometer operated in transmission. The light source is a HeNe laser with a wavelength of 633 nm and an output power of 3 mW. Two lenses (Thorlabs, LD2568 and LA1979) are used to expand and collimate the illuminating laser beam respectively to a full width at half maximum (FWHM) of approximately 15 mm.

In the object arm a 4X Super Apochromatic objective lens ($NA = 0.2$) is used in combination with a 200 mm focal length tube lens (both Thorlabs) to image the sample on the CMOS camera, (Basler beA4000-62kc) with 4096 x 3072 pixels and a pixel pitch of 5.5 micrometer. A rotation mount (Thorlabs CR1) rotates the sample stepwise over 360 degrees. The sample is displaced from the center of rotation by approximately 1 mm in order to suppress noise in the reconstruction of the sample caused by fixed pattern coherent speckle [20]. In the reference arm, a 4X Olympus microscope objective partly compensates for the object wave curvature to avoid the presence of too high spatial frequencies on the camera. The mirror in the reference arm is mounted onto a piezoelectric transducer controlled by a computer for phase-shifting the digital hologram. We capture four holograms with (reference arm) phase shift increments of $\pi/2$ between each subsequent hologram. From a linear combination of these holograms a complex hologram is formed where the zeroth and out of focus conjugate orders are removed [21]. In this way we maximize the lateral resolution in the reconstructed image. This is specifically important for large scale ODT where magnification is low but an as high as possible NA is desired, as we will show in the following section. After acquiring the complex hologram, autofocus correction in the reconstruction of the digital hologram is applied in order to obtain the wavefield in the object region. For off-axis sample placement the object position as a function of the projection angle is a sine function. To find the object position we calculate a focus metric (grayscale variance) as a function of the reconstruction distance for ten samples of a full rotation acquisition (i.e. 0°, 36°, 72°and so on) .

For transparent objects, the grayscale variance has a minimum value when the reconstruction distance is located at the object [20], in contrast to imaging reflective samples where the grayscale variance has a maximum [22]. A sinus function is fitted to the data to retrieve the object distance as a function of projection angle. The hologram is then (for each angle separately) reconstructed with the object in focus by back propagating the field from the detector plane to the object plane using the angular spectrum method for diffraction calculation, which is exact (apart from the scalar approximation to the wave equation). The phase is then calculated by taking the argument of the reconstructed wavefield. Since the phase change in a projection mostly exceeds 2π, the phase is unwrapped using a least squares phase unwrapping algorithm [23].

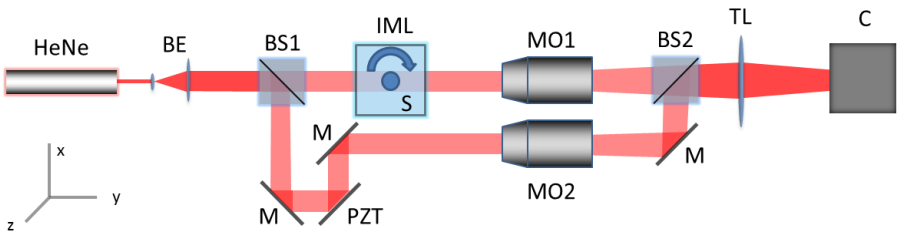

Figure 3.1: Experimental setup for acquiring the digital holograms. HeNe: Helium Neon laser, BE: Beam expander, BS: Beam splitter, IML: Index matching liquid, S: Sample rotated around the z-axis, MO: Microscope objective, M: Mirror, TL: Tube lens, PZT: Mirror mounted on piezo stage, C: Camera.

3.3.2. OPTIMIZING ODT RESOLUTION AND FIELD OF VIEW

In conventional microscopy, in order to meet the Nyquist sampling criterion, it must hold that $\eta \geq 2\xi$, where η is the projected feature size and ξ is the pixel pitch of the camera. In off-axis digital holography, diffraction orders appear that must be spatially separated by introducing an angle between the object beam and the reference beam. In order to separate the twin images, neglecting the frequency content in the zeroth order for simplicity, only half of the spatial frequency bandwidth offered by the camera is available, i.e. $\eta \geq 4\xi$. The smallest resolvable feature that can be imaged with a microscope objective is $\Delta x = 0.61\lambda/NA$ according to the Rayleigh criterion. Hence, for a point object projected onto the camera sensor by an objective with magnification M, the condition

$$\frac{0.61\lambda}{NA} M \geq 4\xi \tag{3.1}$$

must be met in order to satisfy the Nyquist sampling criterion and separate the twin images. For the camera pixel size $\xi = 5.5 \cdot 10^{-6}$ m and wavelength $\lambda = 633 \cdot 10^{-9}$ m the ratio between magnification and numerical aperture to make full use of the available resolution is

$$\frac{M}{NA} \gtrapprox 57. \tag{3.2}$$

Since typical NA values are between 0 and 1 only microscope objectives with high magnification use the spatial frequency bandwidth of the camera without loss in resolution.

In large scale ODT, it is desirable to use a low magnification to image a relatively large object onto the camera while having an as high as possible NA to maximize the resolution. In a standard off-axis configuration this results in a significant loss in resolution. In the setup in this paper we have $M/NA = 20$. Since, by applying phase shifting there are no twin images, Eq. 3.2 reduces to $M/NA \geq 28$ and hence, our ODT imaging set-up configuration is close to the optimum configuration for large scale high resolution ODT.

3.3.3. NOISE SUPPRESSION IN LARGE SCALE ODT

In large scale ODT, RI contrast should be small enough not to cause severe ray displacements and aberrations as a result of light propagation through the sample. Optical clearing of the samples reduces the RI contrast significantly to make the samples suitable for imaging. However, at the same time the contribution of the noise relative to the RI contrast will increase as a result, decreasing the effective sensitivity of the ODT reconstruction. Noise suppression therefore plays an important role, especially in large scale ODT, to obtain high quality images. The noise in the phase projections originates from intensity noise in the digital hologram (assuming perfect phase unwrapping). The noise in the digital hologram translates into the phase noise in a highly non-linear way and an in depth discussion is beyond the scope of this paper. Two sources of intensity noise that contribute to the phase noise can be identified, namely fixed speckle noise in the digital hologram that is constant for each projection[20] and variable noise that changes from projection to projection (e.g. due to read-out or shot noise), which we call incoherent noise. Two methods can be used to reduce the noise levels. The first noise suppression method was proposed by Kostencka et al. [20], where they argue that placing the sample at the center of rotation (as is generally done to keep the sample in focus) leads to more noise in the reconstruction as the speckle noise is spread over a circle in the reconstructed image with radius equal to the off-axis distance. By displacing the sample with respect to the center of rotation the noise is spread over a larger circle in the reconstructed image, and hence is strongly decreased. Kostencka et al. reported a reduction in the reconstruction error by a factor between 2 and 7, depending on the sample size.

Besides the fixed speckle noise, there is noise in the phase projections resulting from incoherent (shot and read) noise fluctuations in the recorded digital holograms. Since this type of noise varies from hologram to hologram it thus leads to variable phase noise in the projections, and can be mitigated through averaging. We suppress this noise with an increase in the number of projections, since backprojection is akin to averaging of projections for each pixel. This is analogous to what is common in signal processing, where signal averaging increases the strength of the signal relative to the noise. More specifically, averaging N realizations of the same, uncorrelated noise reduces the standard deviation by a factor $\sqrt{N}$.

We expect that in the region close to the center of rotation, the first kind of (angle independent) speckle noise dominates the noise level, and that an increase in the number of projections is less effective in suppression of the noise than displacing the sample of axis. Further away from the center of rotation, we expect the contribution due to the speckle noise to be small, and thus further displacing the sample away from the center of rotation will not give significant improvements. Instead, we expect that off-axis the incoherent noise dominates the noise level, and that increasing the number of pro-

jections dominates further improvement in terms of noise suppression according to the $\sqrt{N}$ law. Thus, we expect that noise suppression with an increasing number of projections is effective mainly outside of the center of rotation. To quantify the noise level, we take the standard deviation of the RI difference values in a collection of voxels of a constant RI part of optically cleared agarose. This is in line with the approach of Kim et al. [17], where they associate the standard deviation of a constant background reconstruction with the sensitivity of the ODT reconstruction. In Fig. 3.2 (b) the standard deviation at the axis of rotation (purple circle in Fig. 3.2 (a)) and outward towards the edge of the sample (red circle in Fig. 3.2 (a)) is plotted as a function of the number of projections. It is clear that increasing the number of projections as well as moving the sample radially outward significantly reduces the noise level, increasing the sensitivity up to approximately a factor 4 for 1440 projections compared to on-axis placement of the sample with 360 projections. Furthermore, in Fig. 3.2 (b) a curve $\sigma = a \cdot N_p^{-0.5}$ is fitted to the off axis noise level, where N_p represents the number of projections and a is a constant. The accuracy of the fit confirms the expectation that away from the center of rotation, the incoherent noise type dominates and reduces with the square root of the number of projections. In the center of rotation the decrease in noise as a function of the number of projections is limited due to the presence of the fixed speckle noise, which is indicated by a horizontal line in Fig. 3.2 (b). In Fig. 3.2 (c) the reciprocal of the variance curve (also called the precision or variability) increases linearly with the number of projections in the off-axis case as expected, but stays nearly constant for the on-axis case. Figure 3.2 (d) shows the noise standard deviation through a cross section of the reconstructed object. It shows that the noise level at the center of rotation is similar for 144 and 1440 projections, whereas it differs significantly away from the center of rotation. The noise level can be seen to be approximately constant around half a millimetre away from the center, and further sample displacement will not yield significant noise reduction. Thus, for on-axis placement an increase of the number of projections will not yield significant noise reduction, and away from the center of rotation the variable phase noise (e.g. due to read-out and shot noise) dominates and can be effectively reduced by increasing the number of projections. The fact that the sample must be off-axis (to guarantee low noise) does however reduce the field of view, in our case by almost a factor 8, to approximately 13 mm^3. This was estimated by calculating the area of the largest possible circle in a region starting approximately 0.5 mm away from the center of rotation, until the edge of the horizontal field of view, and multiplying this by the vertical field of view to obtain the volume.

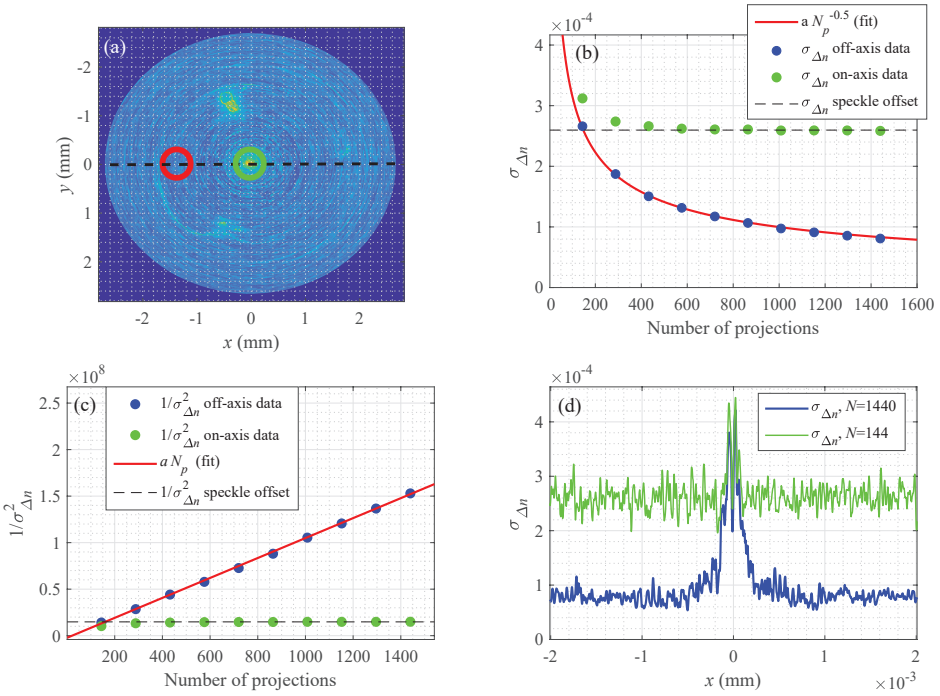

Figure 3.2: (a) Reconstruction of a horizontal cross-section of the agar sample indicating the a point close to the center of rotation (green circle) and one 1 mm radially outward (red circle). (b) Noise levels at the center of rotation and 1.5 mm radially outward as a function of the number of projections (N_p), with $y = a\ N_p^{-0.5}$ fitted to the off-axis data and the on-axis noise limit indicated by a constant. (c) Plot of the precision, defined as the inverse of the variance, of the same data and model as in (b), with $y = a\ N_p$ fitted to the off-axis data and the on-axis noise limit indicated by a constant. (d) Noise levels as a function of distance to the center for 1440 and 144 projections respectively (cross-section horizontally through the middle in (a)).

3.3.4. TOMOGRAPHIC IMAGE RECONSTRUCTION

For reconstruction of the digital hologram the angular spectrum method is used. The phase distribution at the in-focus position is then unwrapped using a least squares phase unwrapping technique [23]. Assuming that RI variation in the sample is sufficiently small so that refraction does not occur, a phase projection can be regarded as a scaled integral over the RI variation with respect to the background medium along the illumination direction. The 3D relative RI (Δn) structure of the object is reconstructed using the filtered back projection (FBP) algorithm, in which case reconstruction can be performed for each transverse slice separately. In this study, we perform tomographic reconstruction with 1440 projections over 360 degrees (steps of 0.25 degrees) with four phase steps per projection. The net acquisition time is approximately 7 minutes. The total acquired data in this case is around 20 GB , which fits in the internal memory of a 32 GB RAM desktop PC.

3.3.5. CHARACTERIZATION OF RESOLUTION

We characterized the spatial resolution of the setup using a FEP-tube (Fluorinated Ethylene Propylene) with an inner diameter of 0.9 mm embedded in a 9 % mass-percentage glucose/water solution. The spatial resolution is estimated based on the edge response from the inner boundary between the FEP-tube and the liquid (at 0.45 mm from the center of rotation) along the x-axis (where z is the vertical axis, and the y-axis the optical axis). For a reconstruction based on 1440 projections, the resolution is estimated to be 4 micrometer.

3.3.6. 3D DATA VISUALISATION

In order to discern different features in the zebrafish samples, we estimated the mean relative RI of different parts of the zebrafish larva by calculating the Δn distribution of a sub volume inside that feature. We used the Drishti software package [24] with a non-linear transfer function of Δn based on the Δn distributions of different zebrafish features for the visualisation.

3.3.7. SAMPLE PREPARATION: 3 DAY OLD ZEBRAFISH LARVA

The sample is a 3 day old zebrafish embryo (wild type). The eggs are grown on a petridish and subsequently placed in PTU (1-phenyl 2-thiourea) to prevent pigment formation. At 72 hours, the eggs are dechorionated and fixated in 4 % paraformaldehyde. Then, the eggs are washed with Phosphate buffered saline tween-20 three times, after which it is replaced with 100% MeOH in two cycles for dehydration. The embryos are placed in small cylinders (4 mm diameter) and mixed with agarose (2% mass-percentage). After the agarose is dry, the agarose containing the embryo's is removed from the cylinders and as a whole placed in BABB, a mixture of benzyl alcohol (Sigma B-1042) and benzyl benzoate (Sigma B-6630) in a 1:2 ratio, to make the sample completely transparent. During this process, the RI of the sample becomes almost that of the BABB clearing solution. The optimal clearing time ensures that the sample is transparent enough for optical phase tomography, while at the same time maximizing remaining RI contrast in order to keep a good signal (RI contrast in the reconstruction) to noise (background) ratio in the final reconstruction. We used a clearing time of 3 hours that we estimate is the optimal time that fulfills the above mentioned criterion.

3.3.8. SAMPLE PREPARATION: DAMAGED ZEBRAFISH HEART

The heart is extracted from a one year old zebrafish. Seven days before extraction, the heart is damaged through cryoinjury. This is done by anesthetizing the fish in tricaine, after which the chest is opened and the heart is damaged with a copper needle cooled in liquid nitrogen [25]. 7 days after damaging the hearts, the fish is euthanized in ice-water. The heart is then isolated in phosphate buffered saline), KCl (Potassium chloride) and heparin. After fixation, the heart is dehydrated, mounted in an agarose (2% mass-percentage) cylinder and placed in BABB solution like the zebrafish samples in the previous section.

3.4. RESULTS

3.4.1. LARGE SCALE ZEBRAFISH ODT

Virtual cross-sections of our large scale zebrafish ODT reconstructions of the sample are shown in Fig. 3.3 (a-c) where Δn is quantitatively visualized on a linear gray scale. The Δn distribution of the reconstructed background (optically cleared agarose) is depicted in Fig. 3.3 (d) and found to have a standard deviation of $\sigma = 8 \cdot 10^{-5}$. Visualization of different structures is done based on the RI difference distribution plotted in the histogram in Fig. 3.4 (f) on a logarithmic scale, and is shown in Fig. 3.4. The RI distribution of an organ was estimated by scaling the distribution of a sub-volume of that organ to the maximum in the histogram. The brain tissue, for example, is distributed around $\Delta n = 2.2 \cdot 10^{-3}$ (visualized in blue in Fig. 3.4), the interstitial tissue is centered around $\Delta n = 7.5 \cdot 10^{-4}$ (visualized in green), and the yolk sac appears in the distribution centered around $\Delta n = 2.0 \cdot 10^{-4}$ (visualized in red). Due the small volume of the eyes and the relatively high RI, it is not visible in Fig. 3.4 (f), but has a RI of around $\Delta n = 1 \cdot 10^{-2}$ and is visualized in red in Fig. 3.4 (d) and (f).

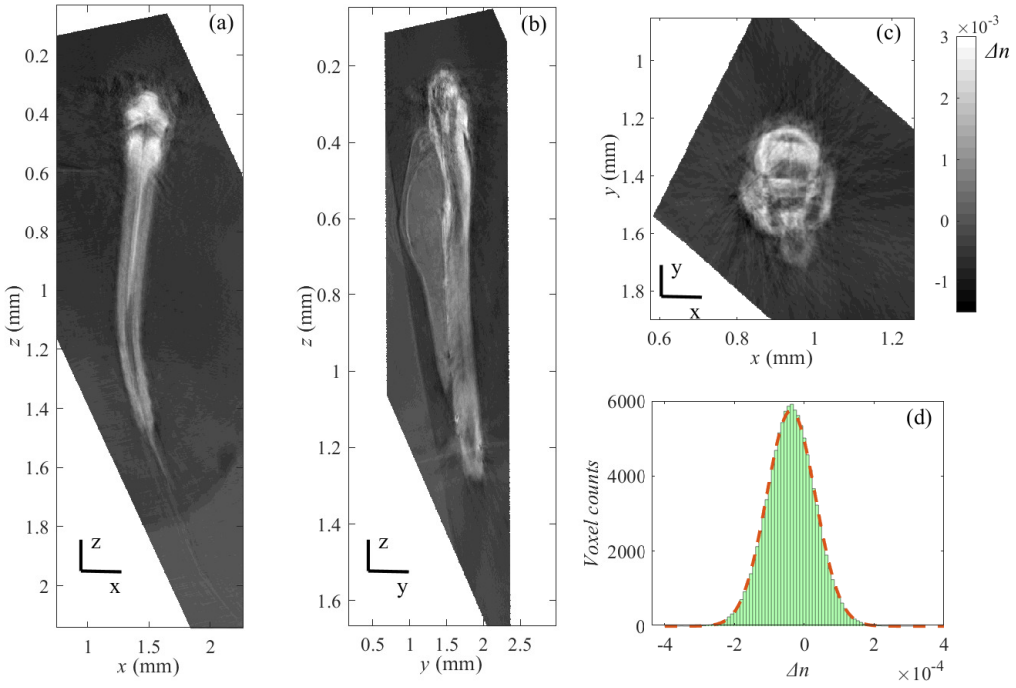

Figure 3.3: (a-c) Coronal, saggital, and axial cross-sections of ODT reconstructed refractive index contrast of an optically cleared 3 day old zebrafish larva. (d) Δn distribution of agarose background in which the zebrafish sample is placed. From this the sensitivity in the reconstruction was calculated as the standard deviation of the distribution and yields $\sigma = 8 \cdot 10^{-5}$

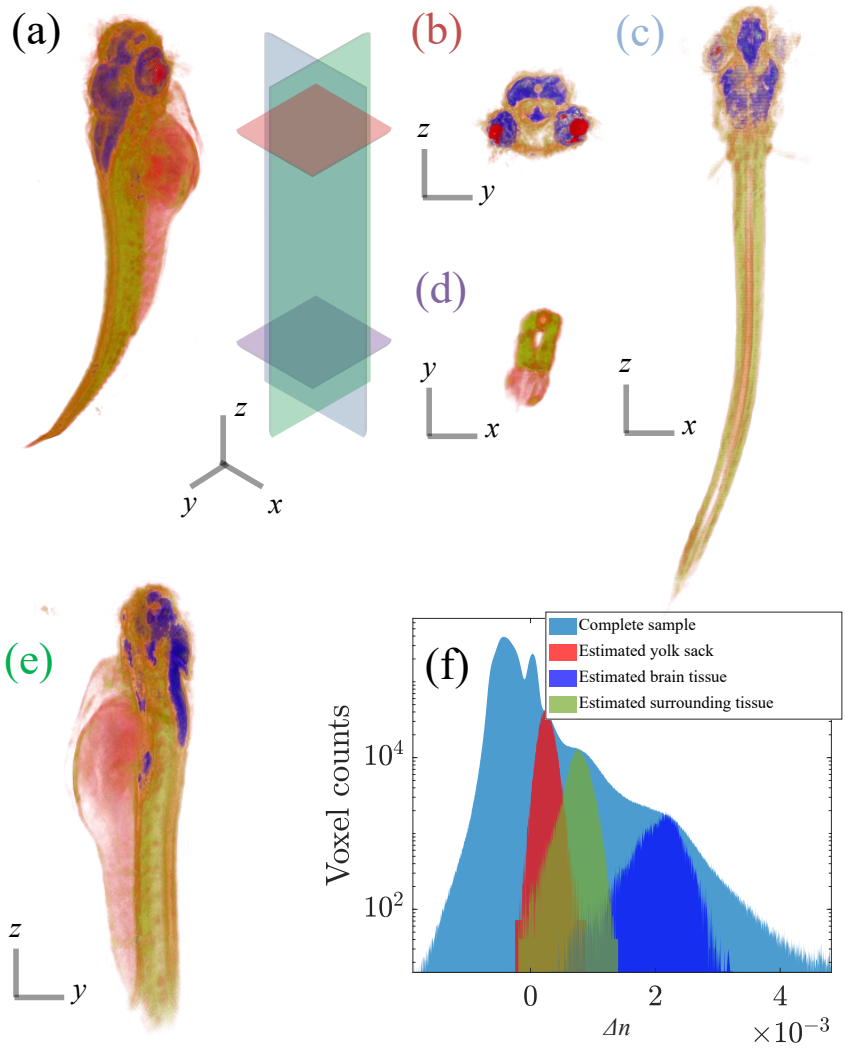

Figure 3.4: A 3D visualization of a complete zebrafish larva (3 days old) based on RI differences is shown in (a) and different cross-sections in (b-e). In (f), a logarithmic plot is shown of the RI distribution of the complete sample (zebrafish larva and agarose). Indicated are the estimated Δn distributions of different types of tissue in the zebrafish larvae. The first two peaks in blue from the left are from the agarose and index matching liquid (BABB) contributions respectively

3.4.2. LARGE SCALE ZEBRAFISH HEART ODT

Virtual cross-sections of the zebrafish heart are shown in Fig. 3.5. Different parts of the heart can be discerned, such as the injured area (IA), the ventricle (V), the bulbus (B) and the atrium (A). The damaged part of the heart is correctly segmented using a region growing algorithm based on RI values of the image [26], and is indicated in the bounded area (red) in Fig. 3.5 (a). The Δn range of the entire heart is found to be comparable to that of the zebrafish larva. The RI distribution of the regenerating tissue was compared to the cleared agarose background and found to have the same mean, but larger standard deviation, since less structure appears in the regenerating tissue. This is as expected, as the zebrafish was euthanized 7 days after cryoinjury, whereas full recovery after cryoinjury takes approximately 2 months. We estimate the relative volume of the injured part to be approximately 14 ($\pm$ 0.5)% of the total heart volume through manual slice by slice segmentation of the 3D reconstruction. This estimate is in line with histological studies of zebrafish regeneration, e.g. Chablais et al. who found an average of relative scar volume between 13.5% and 18.5% in 6 samples aged between 6-18 months and with a similar cryoinjury procedure [1].

3.5. DISCUSSION AND CONCLUSIONS

In this paper, we showed for the first time, to the best of our knowledge, the viability of high resolution and high sensitivity 3D RI imaging of millimeter sized biological samples using ODT. Previously, this has only been achieved using OPT, or with ODT on non-organic homogeneous samples [17], using careful index matching to obtain a low RI contrast (and thus low scattering) and high sensitivity. Optical clearing proved to be an easy to implement solution to make samples sufficiently transparent for ODT , while still retaining relevant RI contrast to segment different organs and features in the zebrafish larva and zebrafish heart. Optimizing the clearing time to approximately 3 hours and the system sensitivity were found to be important for obtaining high quality images. We showed that high RI sensitivity can be achieved by using noise suppression of two independent noise sources. We achieved this by combining off-axis placement of the sample and auto-focus correction together with the acquisition of a large number of projections. Although both techniques lead to an increase in sensitivity independently, we showed that combining them is necessary in order to make optimal use of the potential gain offered by each respective method. In this way, high RI sensitivity can be achieved that is necessary for phase tomography of optically cleared large scale organic tissue. We demonstrate the identification of tissue structures with features in the order of $\Delta n = 6 \cdot 10^{-4}$ with respect to the background and, based on this RI contrast, are able to segment it from the background. Finally, we demonstrated a possible clinical application where regenerating zebrafish heart tissue could be detected and segmented based on RI contrast, and quantified the relative volume of the injured area (after cryoinjury) of a zebrafish heart. Although we did this manually, this can make it possible to study heart regeneration quantitatively in an automated fashion without labour intensive staining, sectioning, and manual estimating of the volumes. To underline this potential, we demonstrated automated segmentation of the injured area using a region growing algorithm on a single slice.

The high sensitivity ODT imaging comes at the cost of the acquisition and processing

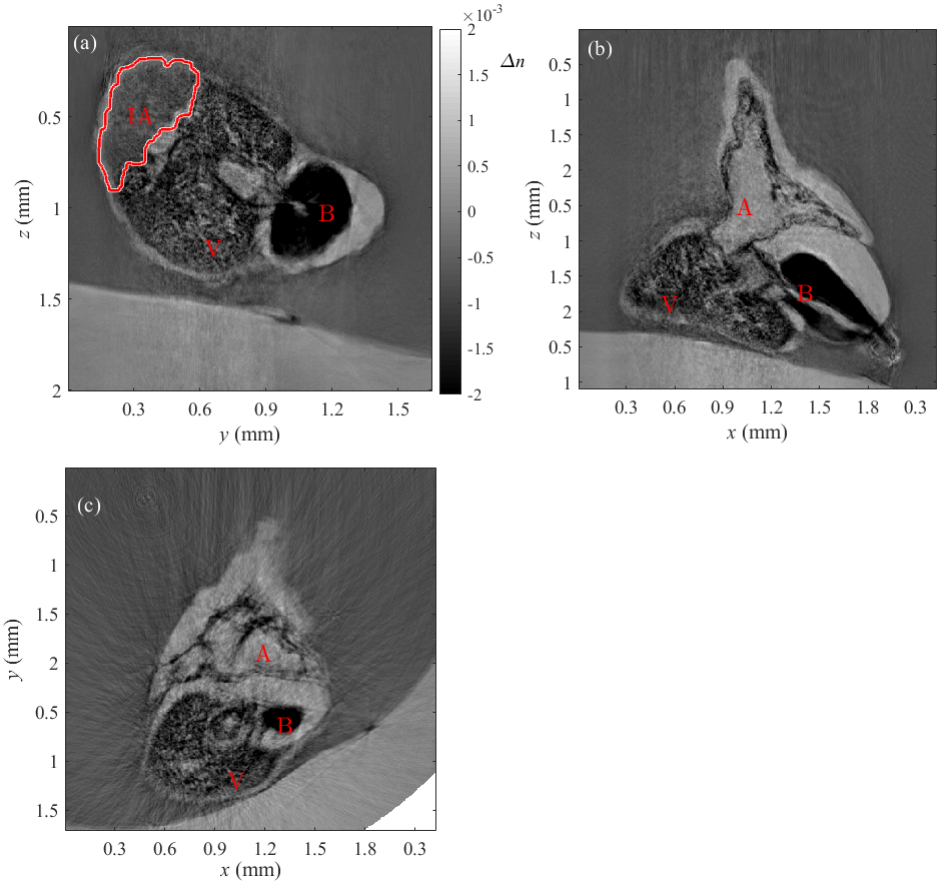

Figure 3.5: Virtual cross-sections in the y-z plane (a), x-y plane (b) and the x-z plane (c) showing the Δn distribution of a 1 year old zebrafish heart, damaged through cryoinjury. The regenerating tissue can be seen in the bounded region (red) in image (a) obtained through region growing segmentation. Features can be seen such as the injured area (IA), the ventricle (V), the bulbus (B) and the atrium (A).

of large data sets which is challenging to handle even with today's powerful desktop computers. Using phase shifting digital holography in large scale ODT, unlike in cases with high magnification, proved necessary for a high resolution with a large field of view but further increases the amount of data. The phase images are reconstructed using filtered back projection, which assumes that rays traverse the object in straight paths and no diffraction takes place. Although this is not a strictly valid assumption, this was done in view of the large dataset; phase projections obtained with 12 Megapixels lead to a dataset of over 100 GB for 1440 projections. In current implementations of ODT using the Rytov approximation the total data should fit in memory at one time in order to do the reconstruction, which is far more than typically available even on powerful desktop computers. FBP allows slice by slice reconstruction, circumventing the memory issue, but at the same time gives a non-isotropic resolution (with resolution deteriorating away from the

focus position). We expect this effect to be limited for zebrafish larva due to the relatively small dimensions in the axial plane and digital refocusing that was applied. However, for large scale ODT on samples with isotropic dimensions and with high (isotropic) resolution we therefore think it is necessary that ODT implementations are developed that allow for step by step reconstruction of the 3D reconstruction, thereby reducing the memory needed at one time, instead of solving the inverse diffraction problem on the entire dataset.

Finally, the zebrafish is relatively long compared to its width. Hence, in order to fit the complete zebrafish larva on the sensor, the magnification should be in the order of 4X for a 12 Megapixel camera. In the vertical direction the image plane (and thus resolution) was therefore used efficiently, but not in the lateral direction. Since the region of interest is usually the brain, the field of view can be restricted to this part of the sample and imaged at a higher magnification (10X) to obtain a higher resolution. The zebrafish heart was more isotropic in size, and can be studied at a higher magnification (10X) without losing part of the sample. It is important however to still keep sufficient unused space laterally in the image plane in order to apply off-axis placement of the sample. We envision that the method presented by us opens the door to application of ODT as a label-free diagnostic tool for studying a wider variety of clinically relevant and larger organic samples than what has been previously done, for example for studying cleared human tissue.

REFERENCES

[1] F. Chablais, J. Veit, G. Rainer, and A. Jaźwińska, *The zebrafish heart regenerates after cryoinjury-induced myocardial infarction,* BMC Developmental Biology **11**, 21 (2011).

[2] *Tomographic diffractive microscopy: Towards high-resolution 3D real-time data acquisition, image reconstruction and display of unlabeled samples,* Optics Communications **422**, 28 (2018).

[3] *Measurements of three-dimensional refractive index tomography and membrane deformability of live erythrocytes from pelophylax nigromaculatus,* Sci. Rep. **8** (2018).

[4] K. Kim, W. S. Park, S. Na, S. Kim, T. Kim, W. D. Heo, and Y. Park, *Correlative three-dimensional fluorescence and refractive index tomography: bridging the gap between molecular specificity and quantitative bioimaging,* Biomed. Opt. Express **8**, 5688 (2017).

[5] J. van der Horst and J. Kalkman, *Image resolution and deconvolution in optical tomography,* Opt. Express **24**, 24460 (2016).

[6] A. K. Trull, J. van der Horst, W. J. Palenstijn, L. J. van Vliet, T. van Leeuwen, and J. Kalkman, *Point spread function based image reconstruction in optical projection tomography,* Phys. Med. & Biol. **62**, 7784.

[7] *Three-dimensional structure determination of semi-transparent objects from holographic data,* Optics Communications **1**, 153 (1969).

[8] T. K. Julianna Winnik, *Autofocusing method for holographic tomography of 3D samples with large axial thickness,* in *Speckle 2018: VII International Conference on Speckle Metrology*, Vol. 10834 (2018) pp. 377 – 384.

[9] B. Belay, J. T. Koivisto, K. Vuornos, T. Montonen, O. Koskela, M. Lehti-Polojärvi, S. Miettinen, M. Kellomäki, E. Figueiras, and J. Hyttinen, *Optical projection tomography imaging of single cells in 3D gellan gum hydrogel,* in *EMBEC & NBC 2017*, edited by H. Eskola, O. Väisänen, J. Viik, and J. Hyttinen (Springer Singapore, Singapore, 2018) pp. 996–999.

[10] A. Bassi, L. Fieramonti, C. D'Andrea, M. C. Mione, and G. Valentini, *In vivo label-free three-dimensional imaging of zebrafish vasculature with optical projection tomography.* Journal of Biomed. Opt. **16(10)**, 100502 (2011).

[11] T. Correia, N. Lockwood, S. Kumar, J. Yin, M.-C. Ramel, N. Andrews, M. Katan, L. Bugeon, M. J. Dallman, J. McGinty, P. Frankel, P. M. W. French, and S. Arridge, *Accelerated optical projection tomography applied to in vivo imaging of zebrafish,* PLOS ONE **10** (2015).

[12] T. Alanentalo, A. Asayesh, H. Morrison, C. Lorén, D. Holmberg, J. Sharpe, and U. Ahlgren, *Tomographic molecular imaging and 3D quantification within adult mouse organs,* (2006).

[13] J. Sharpe, *Optical projection tomography,* in *Advanced Imaging in Biology and Medicine: Technology, Software Environments, Applications*, edited by C. W. Sensen and B. Hallgrímsson (Springer Berlin Heidelberg, Berlin, Heidelberg, 2009) pp. 199–224.

[14] Y. Sung, W. Choi, C. Fang-Yen, K. Badizadegan, R. R. Dasari, and M. S. Feld, *Optical diffraction tomography for high resolution live cell imaging,* Opt. Express **17**, 266 (2009).

[15] M. Kujawińska, W. Krauze, A. Kus, J. Kostencka, T. Kozacki, B. Kemper, and M. Dudek, *Problems and solutions in 3D analysis of phase biological objects by optical diffraction tomography,* International Journal of Optomechatronics **8**, 357 (2014).

[16] M. Malek, H. Khelfa, P. Picart, D. Mounier, and C. Poilâne, *Microtomography imaging of an isolated plant fiber: a digital holographic approach,* Appl. Opt. **55**, 111 (2016).

[17] K. Kim, J. Yoon, and Y. Park, *Large-scale optical diffraction tomography for inspection of optical plastic lenses,* Opt. Lett. **41**, 934 (2016).

[18] *Clarifying tissue clearing,* Cell **162**, 246 (2015).

[19] S.-L. Lai, R. Marín-Juez, P. L. Moura, C. Kuenne, J. K. H. Lai, A. T. Tsedeke, S. Guenther, M. Looso, and D. Y. Stainier, *Reciprocal analyses in zebrafish and medaka reveal that harnessing the immune response promotes cardiac regeneration,* **6** (2017).

[20] J. Kostencka, T. Kozacki, M. Dudek, and M. Kujawińska, *Noise suppressed optical diffraction tomography with autofocus correction,* Opt. Express **22**, 5731 (2014).

[21] I. Yamaguchi and T. Zhang, *Phase-shifting digital holography,* Opt. Lett. **22**, 1268 (1997).

[22] J. van Rooij and J. Kalkman, *Sub-millimeter depth-resolved digital holography,* Appl. Opt. **56**, 7286 (2017).

[23] D. C. Ghiglia and L. A. Romero, *Robust two-dimensional weighted and unweighted phase unwrapping that uses fast transforms and iterative methods,* J. Opt. Soc. Am. A **11**, 107 (1994).

[24] A. Limaye, *Drishti: a volume exploration and presentation tool.* Proc. SPIE 8506, Developments in X-Ray Tomography VIII, 85060X (2012).

[25] J. M. González-Rosa and N. Mercader, *Cryoinjury as a myocardial infarction model for the study of cardiac regeneration in the zebrafish,* Nature Protocols **7**, 782 (2012).

[26] D.-J. Kroon, *Region growing algorithm (m-file)* (MathWorks, Accessed 2 Dec. 2019).

4

POLARIZATION CONTRAST ODT

4.1. ABSTRACT

We demonstrate large scale polarization contrast optical diffraction tomography (ODT). In cross-polarized sample arm detection configuration we determine, from the amplitude of the optical wavefield, a relative measure of the birefringence projection. In parallel-polarized sample arm detection configuration we image the conventional phase projection. For off-axis sample placement we observe for polarization contrast ODT, similar as for phase contrast ODT, a strongly reduced noise contribution. In the limit of small birefringence phase shift δ we demonstrate tomographic reconstruction of polarization contrast images into a full 3D image of an optically cleared zebrafish. The polarization contrast ODT reconstruction shows muscular zebrafish tissue, which cannot be visualized in conventional phase contrast ODT. Polarization contrast ODT images of the zebrafish show a much higher signal to noise ratio (SNR) than the corresponding phase contrast images, SNR=73 and SNR=15, respectively.

4.2. INTRODUCTION

3D imaging in the life sciences is of great importance for studying fundamental biology and performing (pre-) clinical studies. For these studies, label free optical imaging methods play an important role. There are various label-free contrast mechanisms such as scattering, absorption, or refractive index (RI). However, in some cases these contrast mechanisms are not sufficiently sensitive to observe the relevant information, hence, there is a need for imaging with alternative types of intrinsic contrast.

Optical diffraction tomography (ODT) has shown to be an effective tool for 3D imaging of RI contrast on the scale of cells [1] or small organisms [2]. More recently, phase contrast ODT was applied on a millimeter scale, where different structural features of a zebrafish larva and a cryo-injured heart could be distinguished in 3D using RI contrast [3]. However, some types of tissue are not visible in conventional phase contrast ODT.

An alternative form of contrast is given by the polarization change of the optical wavefield caused by tissue birefringence. Birefringent samples are not described by a single scalar RI value per voxel that contributes to the optical path length, but the RI value experienced by the wavefield depends on its polarization state. Polarization contrast has been widely applied in microscopy [4, 5], digital holography[6], optical coherence tomography [7], and optical projection tomography [8]. Birefringence provides a high-constrast label-free mechanism for imaging fibrous structures such as muscle (collagen) or brain (myelin) tissue. Muscle tissue has been imaged in 3D using polarization sensitive optical projection tomography (OPT), as an extension of brightfield OPT using a white light source [8]. However, with OPT phase information is lost and refractive index contrast cannot be determined.

In this work we show that in addition to phase contrast also polarization contrast is compatible with large scale ODT and offers a significantly higher signal to noise ratio (SNR) compared to conventional phase contrast ODT. We determine under what conditions a birefringent sample can be properly reconstructed using conventional filtered backprojection (FBP). Furthermore, we show that off-axis sample placement, which has been used in conventional ODT [9] for noise reduction, also for polarization ODT offers

significant noise reduction and that the same steps of numerical refocusing to correct for defocus can be applied. Finally, we demonstrate 3D multi-contrast imaging of a zebrafish larva using two orthogonal components of the transmitted wavefield, from which a conventional phase contrast and polarization contrast ODT image are reconstructed.

4.3. POLARIZATION CONTRAST IMAGING

In conventional ODT, refractive index differences in the sample causes a change in optical path length of the transmitted light wave. Assuming an isotropic medium, each voxel in the sample gives a fixed contribution to the optical path length of a ray traveling through it regardless of its' polarization. However, when a sample is birefringent this contribution generally depends on the orientation of the polarization of the wave with respect to the medium.

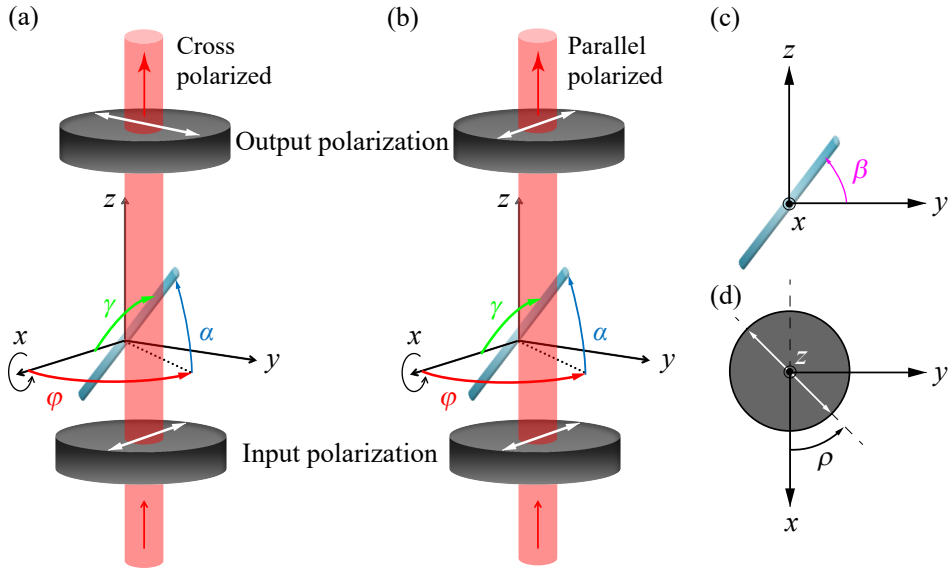

Figure 4.1: Schematic of the ODT sample arm geometry. (a) The orientation of the uniaxial sample is defined by the inclination angle α and the direction angle φ. The sample is rotated around the x-axis for tomographic measurement. The input polarization state is along the x-axis, after which the parallel polarized x-component (a) or the cross-polarized y-component (b) of the complex wave is measured for each projection angle. The tomographic angle β is defined with respect to the fiber orientation in the y-z plane. The angle of the polarizers ρ is defined with respect to the x axis.

Here we use Jones calculus to calculate light interactions with linear polarizing samples. We assume that the birefringent tissue locally can be described as uniaxial, where the optical axis corresponds to the predominant fiber direction. The birefringent tissue is modeled as a wave retarder that introduces a relative phase shift δ along the fast axis with respect to the slow axis, and introduces a common phase shift ϵ (i.e. the average phase of the two components) for both polarization components. The relative phase shift δ between the two components is then defined as [10]

$$\delta = k\Delta\cos^2(\alpha(\beta)), \text{with}\,\Delta = \int [n_e(s) - n_o(s)]\,\mathrm{d}s, \tag{4.1}$$

where α is the fiber inclination angle relative to the x-y plane of the polarizers as indicated in Fig. 4.1(a-b). The wavenumber k is given by $k = \frac{2\pi}{\lambda}$ and Δ is the optical path difference integrated over the sample. As indicated in Fig. 4.1(a-b) the angle φ indicates the angle of rotation of the optic axis of the uni-axial sample with respect to the x-axis projected onto the $x-y$ plane. The rotation angle of the polarizers is given by ρ, which is the angle of the cross/parallel polarizers to the x-axis. The birefringent object is assumed to rotate around the x-axis for tomographic measurement with angle β, which is shown in Fig. 4.1(c). We define the tilt angle of the object with respect to the x axis as γ as show in Fig. 4.1(a-b). During tomographic measurements, the tilt angle γ stays constant. The tomographic rotation causes α and φ to change for each projection according to

$$\alpha = \gamma\sin\beta \qquad \text{and} \qquad \varphi = \gamma\cos\beta, \tag{4.2}$$

respectively.

We assume an incoming beam polarized along the x-axis that travels through the sample in the z-direction. Both the x and y components are extracted by placing an analyzer in the sample arm that can be rotated to align with the parallel x or cross-polarized y-axis. The complex wavefield of an incoming wave polarized along the x-axis after transmission through the birefringent medium is

$$U = \begin{pmatrix} \mathrm{e}^{-\frac{1}{2}i(\delta-2\epsilon)}\left(\sin^2(\rho-\varphi) + \mathrm{e}^{i\delta}\cos^2(\rho-\varphi)\right) \\ -i\mathrm{e}^{i\epsilon}\sin\left(\frac{\delta}{2}\right)\sin(2\rho-2\varphi) \end{pmatrix}, \tag{4.3}$$

with ϵ defined as the average phase

$$\epsilon = \frac{2\pi}{\lambda}\int \frac{n_e(s) + n_o(s)}{2}\,\mathrm{d}s. \tag{4.4}$$

4.3.1. PARALLEL-POLARIZATION OUTPUT

The first component in Eq. 4.3 is the x-component of the transmitted field with a polarization parallel to that of the input field. It can be extracted by placing a polarizer aligned along the x-axis after the sample. The x-component in Eq. 4.3 contains phase contributions of both the conventional phase contrast ϵ and the birefringence contrast δ. The phase of this component is defined as the inverse tangent of the imaginary part divided by the real part

$$\phi_{U_x} = \tan^{-1}\left(\frac{\cot\left(\frac{\delta}{2}\right)\sin(\epsilon)\sec(2\rho-2\varphi) + \cos(\epsilon)}{\cot\left(\frac{\delta}{2}\right)\cos(\epsilon)\sec(2\rho-2\varphi) - \sin(\epsilon)}\right). \tag{4.5}$$

The derivative of ϕ_{U_x} with respect to ϵ is equal to unity and thus the measured phase of the x-component is a linear function of the phase contrast projection ϵ. There is however also a contribution to the phase of the birefringence δ, which is in general non-linear. This can be seen by taking the derivative of Eq. 4.5 with respect to δ, i.e.,

$$\frac{\partial \phi_{U_x}}{\partial \delta} = \frac{\csc^2\left(\frac{\delta}{2}\right)\sec(2\rho - 2\varphi)}{2\cot^2\left(\frac{\delta}{2}\right)\sec^2(2\rho - 2\varphi) + 2}, \tag{4.6}$$

where csc is the cosecant or the reciprocal of the sine function. For small values of δ, Eq. 4.5 can be expanded (in zeroth and first order) as

$$\phi_{U_x} \approx \tan^{-1}(\tan(\epsilon)) + \frac{1}{2}\delta\cos(2\rho - 2\varphi). \tag{4.7}$$

For small values of δ, the measured phase of the x-component will thus be dominated by the average phase ϵ, where $\tan^{-1}(\tan(\epsilon))$ is the wrapped average phase.

4.3.2. CROSS-POLARIZATION OUTPUT

The vertical y-component is the second component of the field in Eq. 4.3 and is perpendicular to the input polarization. The amplitude of this component is given by

$$|U_y| = \left|\sin\left(\frac{\delta}{2}\right)\right| \left|\sin(2\rho - 2\varphi)\right|. \tag{4.8}$$

Similar to what is done in polarimetry it can be measured using crossed polarizers. The presence of birefringence causes modulation in the amplitude of the wavefield as δ appears in the y-component as $\sin\left(\frac{\delta}{2}\right)$ in the amplitude. The amplitude modulation is utilized to generate qualitative birefringence contrast projections in 2D. However, this is problematic for 3D tomographic reconstruction as tomographic reconstruction algorithms usually assume a linear relation between contrast and projection. The projection function δ is thus not measured directly and must be retrieved. Taking the inverse sine of the modulation term we obtain

$$\sin^{-1}\left(\left|\sin\left(\frac{\delta}{2}\right)\right|\right) = \begin{cases} \frac{\delta}{2} - m\pi \text{ if } 0 \le \frac{\delta}{2} < \frac{\pi}{2} \bmod \pi \\ -\frac{\delta}{2} + m\pi \text{ if } \frac{\pi}{2} \le \frac{\delta}{2} < \pi \bmod \pi \end{cases}, \tag{4.9}$$

with m and integer. In Eq. 4.9 the absolute value in the inverse sine is taken since the amplitude is the square root of the intensity and is thus always positive. The inverse sine changes the sign of the original $\frac{\delta}{2}$ function for values $\frac{\pi}{2} \le \frac{\delta}{2} < \pi \bmod \pi$, making the inverse sine of the signal not directly suitable as a linear input projection for FBP reconstruction. Moreover, to reconstruct for arbitrary large δ, the signal needs to be unwrapped using phase unwrapping.

However, from Eq. 4.9 it follows that in case the maximum value of δ in the projection does not exceed π, the signal can be directly retrieved by taking the inverse sine and no further processing is necessary. Even more, if δ is small, the amplitude of the y-component of Eq. 4.3 can be approximated as a linear function of δ, since for small values of δ it holds that

$$|U_y| \approx \frac{1}{2}\delta\left|\sin(2\rho - 2\varphi)\right|. \tag{4.10}$$

To demonstrate the general approach of tomographic birefringence tomography a polarization contrast calculation for the case of a uniaxial birefringent cylinder of 10 mm

radius with a maximum projected phase shift of $\delta = 18$ radians is shown in Fig 4.2. The blue line indicates the original phase shift as a function of position after a plane wavefront travels through the cylinder and this is the signal that has to be retrieved.

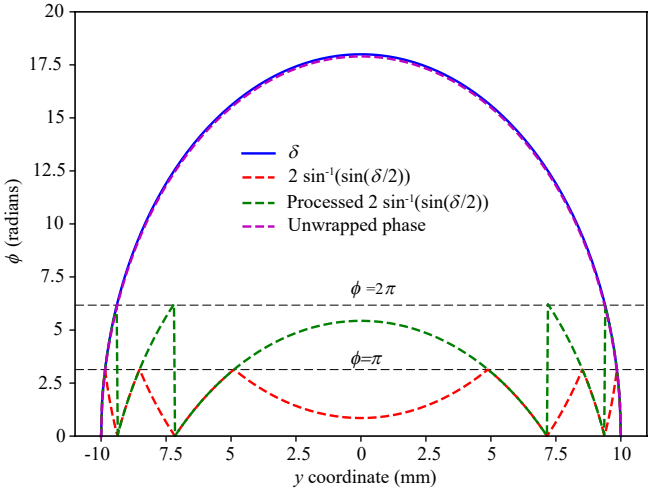

Figure 4.2: Phase shift δ between the two orthogonal polarizations in the case of a uniaxial birefringent cylinder with maximum projected phase shift $\delta = 18$ radians as quantified with polarization contrast imaging.

The red line shows two times the inverse sine of the measured $|\sin(\delta/2)|$ term. The green line is obtained by flipping the inverse sine function in the appropriate domains and adding π according to Eq. 4.9. The function δ can then be retrieved with standard phase unwrapping and is plotted in magenta and corresponds with the original birefringence distribution. Thus, in theory the projection function δ can be retrieved. However, in practice this may not be possible, for example, when the data is noisy or the jumps in the sinusoidal signal of the transmitted field U_y are not properly sampled due to large increase of δ.

4.3.3. POLARIZATION TOMOGRAPHY

In 3D polarization sensitive tomographic imaging, the sample is rotated and the x (parallel) and y (cross) components of the wave are recorded for each angle for phase and polarization contrast respectively. Due to the small contribution of the birefringence contrast in the x-component phase it can be used for conventional ODT. However, it should be noted that in order to preserve the linear relationship between the projection and δ for the y component, it can be seen from Eq. 4.10 that not the intensity (amplitude squared) of the wavefield should be taken as the projection, but the square root of the intensity (amplitude).

However, in general δ itself depends on the tomographic rotation angle β through α in Eq. 4.1 and Eq. 4.2. Furthermore, the angle φ in Eq. 4.10 depends on β as well through

Eq. 4.2. Using these dependencies we find that for small δ the y-component of the field is

$$|U_y|(\beta) \approx \frac{1}{2} k\Delta \cos^2(\gamma \sin(\beta)) \left|\sin(2\rho - 2\gamma\cos(\beta))\right| . \tag{4.11}$$

Thus, even though the amplitude of U_y is linear with respect to δ, the signal is non linear with respect to the rotation angle β. The first non-linearity occurs due to the $\cos^2(\gamma\sin(\beta))$ term in Eq. 4.11. Here we demonstrate the effect of this non-linearity in the amplitude projection on the tomographic reconstruction. The object we consider is a cylinder according to the orientation outlined in the theory section of this paper. The cylinder has radius R, and birefringence $n_e - n_o = \delta n$. For a plane wave traveling along the z-axis linearly polarized along the x-axis, the polarization contrast is retrieved from the cross-polarized transmitted component after traveling through the sample. This component U_y is given by the y component of Eq. 4.13. Using the relations $\delta = k\Delta\cos^2(\alpha(\beta))$, $\alpha = \gamma\sin(\beta)$ and $\phi = \gamma\sin(\beta)$, the full expression for U_y on β becomes

$$U_y(\beta) = -ie^{i\epsilon} \sin(2\rho - 2\gamma\cos(\beta)) \sin\left(\frac{1}{2} k\Delta\cos^2(\gamma\sin(\beta))\right), \tag{4.12}$$

and the amplitude of $U_y(\beta)$ is

$$|U_y(\beta)| = \left|\sin(2\rho - 2\gamma\cos(\beta))\right| \left|\sin\left(\frac{1}{2} k\Delta\cos^2(\gamma\sin(\beta))\right)\right| . \tag{4.13}$$

For a cylinder located at the origin with a tilt γ with respect to the x-axis of tomographic rotation, the cross-section seen by a wave traveling along the z-axis is an ellipse $f(y,z)$, with semi-major and semi-minor axes $a = R\sec(\gamma)$ and $b = R$, respectively. The Radon transform $\Re(f)$ for a 2D slice of the ellipse gives the path length experienced by the probing wave per projection angle β and is given by [11]

$$\Re(f) = \begin{cases} \frac{2R^2\sec(\gamma)\sqrt{A-p^2}}{A} & p^2 \le A \\ 0 & \text{otherwise} \end{cases} \tag{4.14}$$

where

$$A = R^2\cos^2(\beta)\sec^2(\gamma) + R^2\sin^2(\beta), \tag{4.15}$$

and p is the transverse coordinate along the projection. Replacing Δ in Eq. 4.13 with $\Re(f)\delta n$, the effective amplitude projection function measured at the detector becomes

$$|U_y(p,\beta)| = \begin{cases} \left|\sin(2\rho - 2\gamma\cos(\beta)) \sin\left(\frac{R^2\,\delta n\, k\sec(\gamma)\cos^2(\gamma\sin(\beta))\sqrt{A-p^2}}{A}\right)\right| & p^2 \le A \\ 0 & \text{otherwise} \end{cases} \tag{4.16}$$

The projection functions $|U_y(p,\beta)|$ along with the resulting tomographic reconstructions are plotted in Fig. 4.3 for tilt angles $\gamma = 0°$ (a-b) and $\gamma = 54°$ (c-d). The simulation parameters are cross-polarizer angle $\rho = 27°$, $\delta n = 1\cdot 10^{-5}$, $R = 1$ mm and $\lambda = 633$ nm. For comparison, the case for a non-birefringent cylinder at $\gamma = 54°$ is shown (e-f). It can

be seen that the angular dependency of the amplitude projections results in a modulation along the horizontal projection angle axis in Fig. 4.3(c). Since this does not cause modulation along the transverse coordinate axis and the amplitude is zero outside of the projection of the birefringent object, the contrast inside the birefringent sample is not modulated (Fig. 4.3 (d)). Instead, it gives a slowly varying angular modulation in the background.

The second term $\left|\sin(2\rho - 2\gamma\cos(\beta))\right|$ in Eq. 4.11 also modulates the amplitude as a function of the tomographic angle β. This can be compensated for by taking the cross-polarization angle ρ such that $\left|\sin(2\rho - 2\gamma\cos(\beta))\right|$ is maximum. Experimentally, this implies that tomographic image acquisition should be done for a sufficient number of cross-polarizer angles ρ, and for each projection angle β the maximum amplitude projection is subsequently selected [8]. Thus, despite the angular dependency of the phase shift δ, a linear reconstruction algorithm can be used for polarization contrast tomography.

The question arises whether the phase of the crossed-polarizer component can be used to do the conventional phase reconstruction, so that capturing of U_x is not necessary. In cross polarization, the phase ϵ of the transmitted y-component is defined for any path through the birefringent sample where the field amplitude is not zero. Hence, this component cannot be used to reconstruct the conventional RI contrast ϵ across the whole sample. However, the phase of the y-component can be used in order to propagate the wavefield. This can be used to numerically refocus the wavefield if necessary, for example in the case of off-axis placement of the sample for noise suppression [3, 9], or to extend the depth of field of the imaging system [2].

4.3.4. POLARIZATION TOMOGRAPHY SIMULATIONS

In order to analyze the effect of large magnitude of δ on the tomographic reconstruction, we model a homogeneous hollow cylinder that exhibits uniaxial birefringence along the direction of the cylinder axis, based on a macroscopic model of a birefringent nerve fiber [10]. The cylinder has a radius of 1 mm, is illuminated with a plane wave of wavelength 633 nm, and has a refractive index difference $n_e - n_o$ along the optical axis and perpendicular to it that is varied between $1.3\cdot10^{-5}$, $1.3\cdot10^{-4}$ and $1.3\cdot10^{-3}$, corresponding to a maximum phase shift δ_{max} of approximately 0.26, 2.6 and 26 radians respectively. The results of the simulation are plotted in Fig. 4.4, where the first row corresponds to $n_e - n_o = 1.3\cdot10^{-5}$ and the last row to $n_e - n_o = 1.3\cdot10^{-3}$. The first column shows the amplitude projections, the second column the digital holograms and the last column a slice of the reconstructed cylinder perpendicular to the cylinder axis, reconstructed with FBP. It can be seen that for larger values of the projection integral δ, the FBP reconstruction does not yield correct results due to the non-linear behaviour of U_y for larger values of δ. At $n_e - n_o = 1.3\cdot10^{-4}$ a non-uniform birefringence is visible in the reconstruction. For $n_e - n_o = 1.3\cdot10^{-3}$ the reconstruction even yields ringing artifacts. We applied our proposed processing of the data, namely taking the inverse sine of the projection and apply a modified phase unwrapping procedure, and can correctly reconstruct the projection and the tomographic reconstruction for even a birefringent sample with the highest birefringence $n_e - n_o = 1.3\cdot10^{-3}$. This is indicated in Fig. 4.4(k).

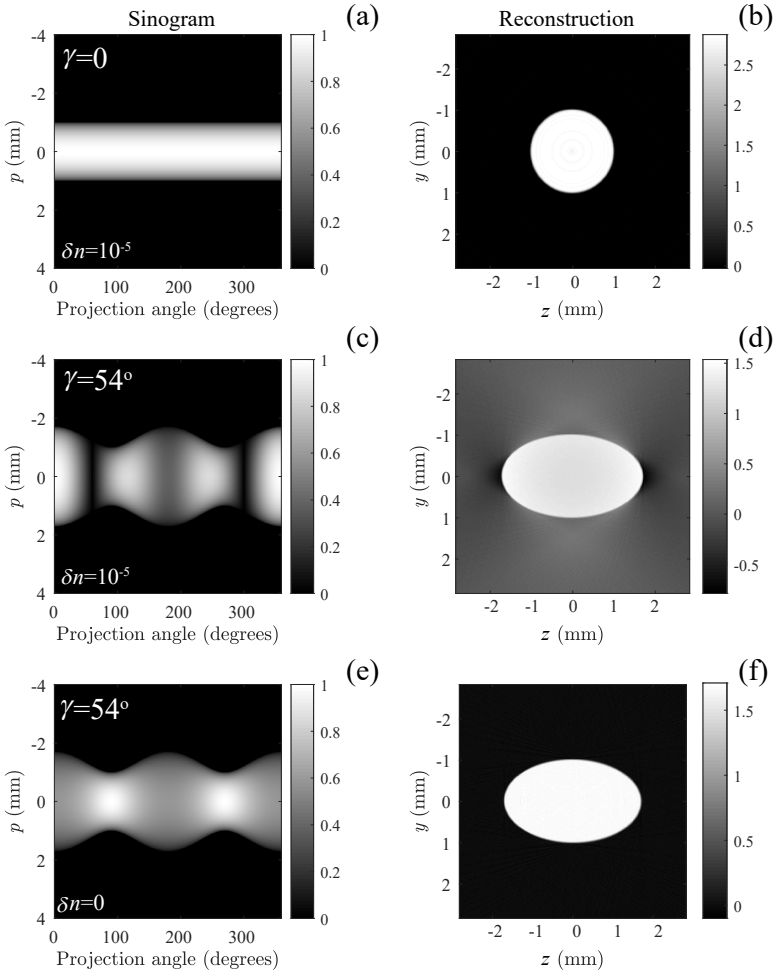

Figure 4.3: Plot of the projection functions $|U_y(p,\beta)|$ along with the resulting tomographic reconstructions for tilt angles $\gamma = 0°$ (a-b) and $\gamma = 54°$ (c-d). The simulation parameters are cross-polarizer angle $\rho = 27°$, $\delta n = 1 \cdot 10^{-5}$, $R = 1$ mm and $\lambda = 633$ nm. For comparison, the case for $\gamma = 54°$ for a non-birefringent cylinder is shown (e-f).

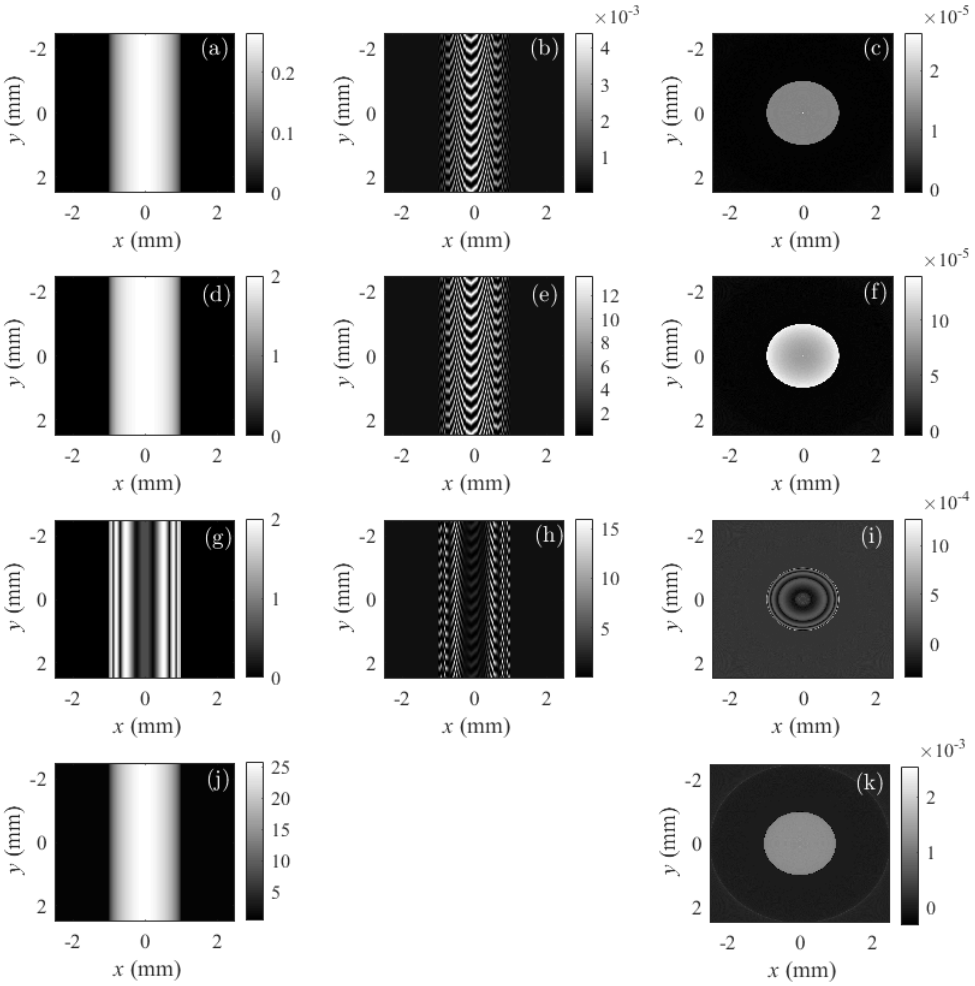

Figure 4.4: Polarization tomography simulations. (a-c) Simulation for $n_e - n_o = 1.3 \cdot 10^{-5}$ with (a) the amplitude projection, (b) the digital hologram at one angle and (c) the 2D reconstruction for a cylinder with radius of 1 mm.This figures illustrates what happens when the $n_e - n_o$ of the birefringent medium (the refractive index difference experienced by the two orthogonal polarization states) becomes large enough so that the projection is no longer linear with respect to the $n_e - n_o$ contrast. (d-f) for $n_e - n_o = 1.3 \cdot 10^{-4}$ and (g-i) for $n_e - n_o = 1.3 \cdot 10^{-3}$. (j-k) corrected phase and reconstruction for the $n_e - n_o = 1.3 \cdot 10^{-3}$ case based on our proposed unwrapping scheme.

4.4. MATERIALS AND METHODS

4.4.1. ACQUISITION OF PROJECTIONS

In ODT, the scattered field is recorded from multiple angles using digital holography. The digital holography setup is shown in Fig 4.5 and consists of a Mach-Zehnder interferometer operated in transmission. The light source is a HeNe laser with a wavelength of 633 nm and an output power of 3 mW. Two lenses (Thorlabs, LD2568 and LA1979) are used to expand and collimate the illuminating laser beam to a full width at half maximum (FWHM) of approximately 15 mm.

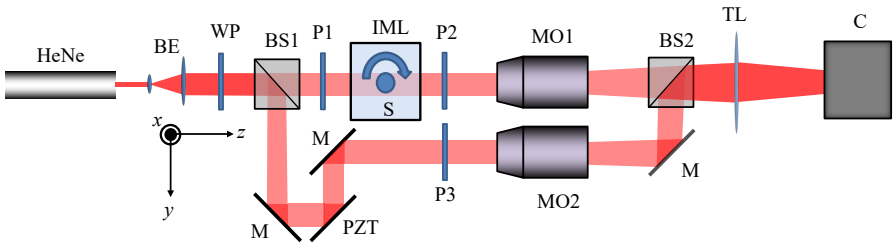

Figure 4.5: Experimental setup for acquiring the digital holograms. HeNe: Helium Neon laser, BE: Beam expander, BS: Beam splitter, IML: Index matching liquid, S: Sample rotated around the z-axis, MO: Microscope objective, M: Mirror, TL: Tube lens, PZT: Mirror mounted on piezo stage, C: Camera, P: Polarizer, WP: Half-wave plate.

In the object arm a 10X objective lens (NA=0.3) is used in combination with a 200 mm focal length tube lens (Thorlabs) to image the sample in close proximity to the detector of a CMOS camera, (Basler beA4000-62kc) with 4096×3072 pixels and a pixel pitch of 5.5 µm. A rotation mount (Thorlabs CR1) rotates the sample stepwise over 360°. One polarizer is placed in front of the sample (P1), and a second one is placed behind the sample (P2). For acquisition of the regular phase contrast projections, the optical axes of the polarizers are made parallel and a acquisition of 720 projections over 360° is performed. For the polarization contrast projections, the relative angle between both polarizers is kept constant at 90°. The complete tomographic measurement is then carried out as before. The polarization contrast measurement is then repeated after simultaneous rotation of both the polarizers by 30° and 60°,respectively. In the reference arm, a polarizer (P3) is placed in order to maximize the fringe contrast at the detector; this polarizer is rotated simultaneously with the polarizers in the object arm. A half-wave plate is placed behind the beam expander in order to maximize the signal at the detector. In the reference arm, a 10X Olympus microscope objective partly compensates for the object wave curvature to avoid the presence of too high spatial frequencies on the camera. The mirror in the reference arm is mounted onto a piezoelectric transducer (Thorlabs, KPZ 101) controlled by a computer for phase-shifting the digital hologram. We capture four holograms with reference arm phase shift increments of $\pi/2$ between each subsequent hologram. From

a linear combination of these holograms a complex hologram is formed where the zeroth and out of focus conjugate orders are removed [12]. In this way we maximize the lateral resolution in the reconstructed image. This is specifically important for large scale ODT where magnification is low but an as high as possible NA is desired.

4.4.2. PHASE AND POLARIZATION PROJECTIONS

Autofocus correction is applied on the digital hologram in order to obtain the wavefield in the object region. The object position is determined by calculating a focus metric (grayscale variance) as a function of the reconstruction distance. For transparent objects the gray scale variance has a minimum value when the reconstruction distance is located at the object. For polarization contrast projections, the gray scale variance has a maximum value when reconstructed in focus. For both cases separately the minimum/maximum is determined for ten samples of a full rotation acquisition (i.e. 0°, 36°, 72°, etc.). A sinusoidal function is then fitted to the minimum/maximum as a function of the projection angle to determine the object distance as a function of projection angle. For every angle the hologram is reconstructed for both the phase and polarization contrast data, with the object in focus by propagating the field to the object plane using the angular spectrum method for diffraction calculation, which is exact and valid for small propagation distances. In case of the phase projections, the phase is then calculated by taking the argument of the reconstructed wavefield. The phase projections are unwrapped using a least squares phase unwrapping algorithm [13].

For the polarization contrast projections, the amplitude of the cross-polarized component is calculated. This amplitude then gives a direct, but scaled measure for the birefringence: scaled $n_e - n_o$. For the different (cross) polarizations, the projections are misaligned horizontally by a few pixels. This is corrected by determining the center of rotation from the maximum variance of the tomographic reconstruction as a function of the shift for each polarization contrast sinogram individually. The projections are then shifted to the correct location using the circular shift function of MATLAB. The wavefield amplitude of the projections for the three angles are stacked, and the maximum value for each camera coordinate is extracted to form a single maximum birefringence projection sinogram. Tomographic imaging is performed with 720 projections over 360° (steps of 0.5°) with four phase steps per projection. At every projection angle and phase step, four measurements are taken (one for phase, three for polarization contrast) in total. The net acquisition time for a full 3D measurement is approximately 7 minutes with the total acquired data around 160 GB.

4.4.3. TOMOGRAPHIC IMAGE RECONSTRUCTION AND VISUALIZATION

For reconstruction of the phase contrast, assuming that RI variation in the sample is sufficiently small so that refraction does not occur, a phase projection is a scaled integral over the RI variation with respect to the background medium along the illumination direction. The average refractive index difference Δn_{avg} is calculated from the phase by using the system magnification and the pixel pitch [9]. Subsequently, the Δn_{avg} object is reconstructed using the FBP algorithm on a slice by slice basis. For polarization contrast, the maximum birefringence projection sinogram δ is reconstructed using the FBP algorithm as $n_e - n_o$. We used the Drishti software package [14] to visualize and merge

the phase and polarization contrast reconstructions with a non-linear transfer function.

4.4.4. NOISE SUPPRESSION IN POLARIZATION SENSITIVE ODT

The sample is displaced from the center of rotation by approximately 0.5 mm. Figure 4.6 shows the noise distribution, in standard deviation σ, in a tomographic ODT reconstruction of both the polarization contrast (a) and (b) and the phase contrast (c) and (d). The polarization contrast ODT reconstruction suffers from increased noise in the region of the center of rotation, similar to what has been shown to be the case with phase contrast ODT. The noise at the center of rotation is approximately a factor 7 higher than outside of the center. This also shows that the on-axis noise reduction is even more significant in the case of polarization contrast ODT than in phase contrast ODT, where the noise reduction by off-axis placement was found to be in the order of a factor 2 for 720 projections [3].

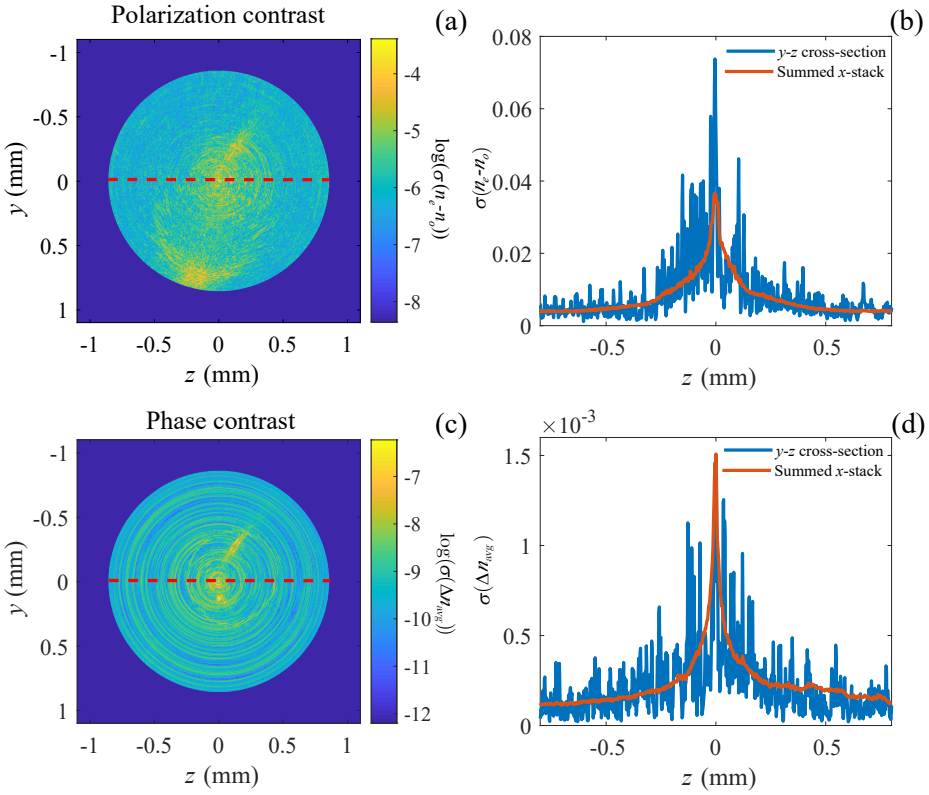

Figure 4.6: (a) Logarithm of the standard deviation $\sigma(n_e - n_o)$ of a single polarization contrast reconstructed slice. (b) Cross-section along the dashed line in figure (a) and the average standard deviation over all slices of the stack (red). (c) Logarithm of the standard deviation $\sigma(\Delta n_{avg})$ of the phase contrast reconstructed slice. (d) Cross-section along the dashed line in figure (c) and the average standard deviation over all slices of the stack (red).

4.4.5. ZEBRAFISH SAMPLE PREPARATION

The sample is a 3 day old zebrafish embryo (wild type). The eggs are grown on a petridish and subsequently placed in PTU (1-phenyl 2-thiourea) to prevent pigment formation. At 72 hours, the eggs are dechorionated and fixated in 4% paraformaldehyde. Then, the eggs are washed with Phosphate buffered saline three times, after which it is replaced with 100% MeOH in two cycles for dehydration. The embryos are placed in small cylinders (4 mm diameter) and mixed with agarose (2% mass-percentage). After the agarose is dry, the agarose containing the embryo's is removed from the cylinders and as a whole placed in BABB, a mixture of benzyl alcohol (Sigma B-1042) and benzyl benzoate (Sigma B-6630) in a 1:2 ratio, which makes the sample completely transparent [15]. During this process, the RI of the sample becomes almost that of the BABB clearing solution. We used a clearing time of 3 hours (similar to [3]) that ensures that the sample is transparent enough for optical phase tomography, while at the same time maximizing remaining RI contrast in order to keep a good signal (RI contrast in the reconstruction) to noise (background) ratio in the final reconstruction.

4.5. RESULTS

The polarization and phase contrast projections of a 3 day old zebrafish tail are shown in Fig. 4.7 (a)-(b) and (d)-(e), respectively. The phase contrast projections are similar to our earlier work on ODT applied to zebrafish larvae [3]. In the polarization contrast projections most of the larva appears dark, due to the absence of birefringent tissue, except in the tail where the developing highly birefringent muscle tissue (myotome) is located. The polarization contrast results are found to be similar in comparison with 2D polarization contrast measurements of Jacoby et al. [16]. The histograms of the 3D polarization and phase contrast reconstructions are shown in Fig. 4.7 (c) and (f) respectively. The polarization contrast histogram of the scaled birefringence shows two components, namely the background and the myotome tissue. In the phase contrast histogram of the polarization averaged refractive index multiple peaks, corresponding to different organs, are visible [3].

A 3D visualization of the phase contrast, the polarization contrast, the merged datasets and transverse cross-sections after tomographic reconstruction using FBP are shown in Fig. 4.8. It can be clearly seen from the visibility of the developing muscle tissue (myotome) that the phase and polarization contrast offer complementary contrasts, even though they spatially overlap. The anatomical structures are annotated based on reference data from microscopy [16] and OPT [17]. A striking result is the high contrast obtained in the polarization contrast projections compared to the phase projections. We quantify this by calculating the standard deviation of a background region outside of the center (since the level of noise is lower there), and estimate the mean of the signal in the tail at the same location for both the polarization and phase contrast reconstructions. For polarization contrast ODT, this yields an SNR of approximately SNR=73, and for the phase contrast ODT we obtain an SNR of approximately SNR=15. Polarization contrast ODT thus yields significantly higher SNR than phase contrast ODT for imaging the zebrafish tail.

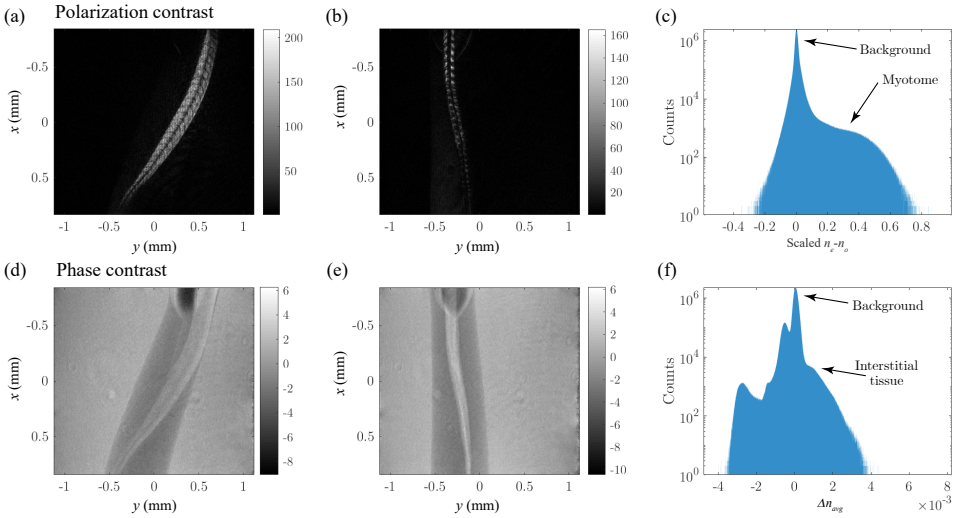

Figure 4.7: Reconstructed amplitude (a) and (b) and phase projections (d) and (e) from two different angles of a 3 day old optically cleared zebrafish larva, illustrating the different contrasts obtained through polarization and phase contrast respectively. In (c) and (f) the histograms of the full 3D data set are plotted for the polarization and phase contrasts, respectively. The background contribution is indicated in both histograms, and the myotome and interstitial tissue for the polarization and phase contrast, respectively.

4.6. DISCUSSION AND CONCLUSION

We demonstrate 3D polarization contrast ODT, which has previously only been achieved only with OPT. Applying it within the framework of ODT makes it possible to image both phase and polarization contrast and make use of the benefits of ODT such as numerical refocusing and extended depth of field, due to the fact that both phase and amplitude of the polarization contrast field are measured.

4.6.1. POLARIZATION ODT CONTRAST

Coherent speckle causes increased noise levels close to the center of rotation in polarization contrast ODT similar as in conventional phase contrast ODT and the same strategy of off-axis placement and numerical refocusing can be applied to reduce the noise level up to a factor of 7. The polarization contrast ODT reconstruction yields a significantly higher signal to noise ratio compared to the phase contrast reconstruction. We attribute this to the fact that in phase contrast ODT the refractive index differences decrease during clearing, leading to a reduction of the signal to noise ratio in the reconstructed images. For polarization contrast ODT, the background is zero (no transmission in the absence of birefringence) and consequently leads to a relatively high contrast when birefringent tissue is present. Besides this qualitative argument, also quantitatively, the value of the average refractive index, which is proportional to $n_e + n_o$, and the birefringence $n_e - n_o$ may vary during the clearing process [18] and thus influence the image contrast in both ODT modes.

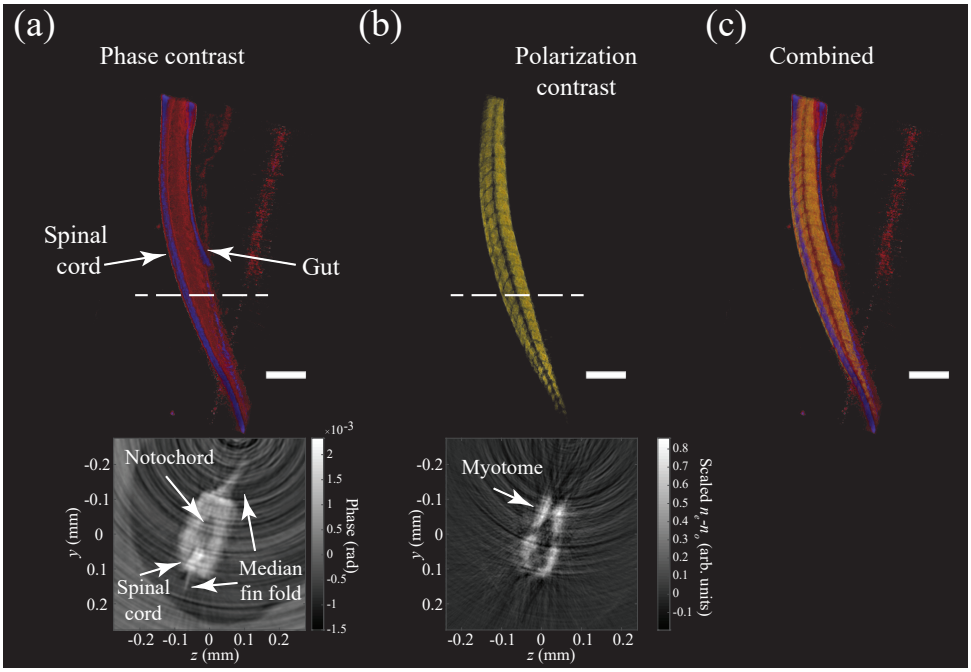

Figure 4.8: 3D visualization of the phase (a) and polarization (b) contrast, and combined (c) ODT reconstructions of a 3 day old zebrafish larva tail. In phase contrast, the tail (in red) and the spinal cord (in purple) appear, but not the developing muscle tissue (myotome), which is birefringent. In the polarization contrast reconstruction the structure of the myotome can be clearly discerned. Scalebar for 3D reconstruction corresponds to 200 μm. Insets show transverse cross sections in linear intensity scale taken at the location of the dashed line.

4.6.2. LIMIT ON MAXIMUM PROJECTED δ

Straightforward tomographic reconstruction procedure only yields valid results for polarization contrast ODT in case δ is small. In phase projections of highly birefringent materials, such as a FEP (fluorinated ethylene propylene) tube, phase wrapping is clearly visible as a dense amplitude modulation. For cleared biological samples we have not observed dense amplitude modulation and, for all practical purposes, the wrapping problem is absent. Even for uncleared samples with 0.5 mm of birefringent tissue, phase wrapping is absent for birefringence lower than $n_e - n_o = 6 \cdot 10^{-4}$, which is still smaller than the typical birefringence of uncleared tissue [7].

For application outside of biomedicine, the wrapping of δ places a practical limitation on the amount of birefringence and/or the maximum sample thickness that can be imaged using conventional reconstruction. In principle, the correct projection and reconstruction can be retrieved in case the linearity requirement is violated using a modified unwrapping procedure based on the forward model. However, further research is needed for application of this procedure on experimental data.

4.6.3. ABSOLUTE QUANTIFICATION OF BIREFRINGENCE

A limitation of the current method is that the polarization contrast is qualitative. Absolute quantification of the birefringence is challenging as the magnitude of the signal is dependent on the incident field distribution, sample optical absorption, the light to electron conversion, and the fiber orientation. In principle the first three factors can be divided out using a reference measurement, e.g., from the amplitude of the parallel polarization state projection. A further complication comes from the tomographic angle dependence of δ that causes a modulation outside of a continuous region of birefringence. In case the macroscopic assumption of uniform birefringence across a region does not apply, but the fiber orientation changes significantly on small length scales this may cause reconstruction artifacts. The case for quantitative birefringence tomography (quantification of optic axis, n_e, and n_o) is more complicated as it requires more information per projection angle and a non-linear inversion scheme. This is outside of the scope of the current work.

4.6.4. APPLICABILITY OF THE UNIAXIAL MODEL

The analysis and simulations in this paper are based on the assumption of uniaxial birefringence. The uniaxial model is a simple and widely used model in polarization microscopy, and applicable to fibrous structures such as myelin, elastin, and collagen. The fiber orientation as is present in the uniaxial model would be of importance to extract from the data. Further research is needed to determine whether fiber orientation can be retrieved in 3D, for example by performing more measurements under different input polarizations and using a full vectorial reconstruction [19].

Although the uniaxial model works for a large class of tissues, some types of tissues exhibit biaxial birefringence [20]. In addition, in some voxels there may be overlapping tissue fibers. Incorporating this in the tomographic reconstruction requires a more elaborate model and is a topic for further research.

4.6.5. CONCLUSION

We demonstrated 3D polarization contrast ODT. The developing muscle tissue in the tail of the zebrafish larva is known to be birefringent and cannot be discerned in conventional phase contrast ODT reconstruction. By illuminating the sample with a single polarization input state and measuring both the parallel (for the phase) and the orthogonal component (for the polarization contrast) with digital holography a conventional and polarization contrast ODT reconstruction of the same object can be obtained.

REFERENCES

[1] K. Kim, K. S. Kim, H. Park, J. C. Ye, and Y. Park, *Real-time visualization of 3-D dynamic microscopic objects using optical diffraction tomography,* Opt. Express **21**, 32269 (2013).

[2] W. Choi, C. Fang-Yen, K. Badizadegan, R. R. Dasari, and M. S. Feld, *Extended depth of focus in tomographic phase microscopy using a propagation algorithm,* Opt. Lett. **33**, 171 (2008).

[3] J. van Rooij and J. Kalkman, *Large-scale high-sensitivity optical diffraction tomography of zebrafish,* Biomed. Opt. Express **10**, 1782 (2019).

[4] R. Oldenbourg, *A new view on polarization microscopy,* Nature **381**, 811 (1996).

[5] F. Massoumia, R. Juškaitis, M. A. A. Neil, and T. Wilson, *Quantitative polarized light microscopy,* J. Microsc. **209**, 13 (2003).

[6] Z. Wang, L. J. Millet, M. U. Gillette, and G. Popescu, *Jones phase microscopy of transparent and anisotropic samples,* Opt. Lett. **33**, 1270 (2008).

[7] M. J. Everett, K. Schoenenberger, B. W. Colston, and L. B. D. Silva, *Birefringence characterization of biological tissue by use of optical coherence tomography,* Opt. Lett. **23**, 228 (1998).

[8] M. Fang, D. Dong, C. Zeng, X. Liang, X. Yang, A. Arranz, J. Ripoll, H. Hui, and J. Tian, *Polarization-sensitive optical projection tomography for muscle fiber imaging,* Scientific reports **6**, 19241 (2016).

[9] J. Kostencka, T. Kozacki, M. Dudek, and M. Kujawińska, *Noise suppressed optical diffraction tomography with autofocus correction,* Opt. Express **22**, 5731 (2014).

[10] M. Menzel, K. Michielsen, H. De Raedt, J. Reckfort, K. Amunts, and M. Axer, *A Jones matrix formalism for simulating three-dimensional polarized light imaging of brain tissue,* .

[11] A. C. Kak and M. Slaney, *Principles of computerized tomographic imaging* (IEEE press).

[12] I. Yamaguchi and T. Zhang, *Phase-shifting digital holography,* Opt. Lett. **22**, 1268 (1997).

[13] D. C. Ghiglia and L. A. Romero, *Robust two-dimensional weighted and unweighted phase unwrapping that uses fast transforms and iterative methods,* J. Opt. Soc. Am. A **11**, 107 (1994).

[14] A. Limaye, *Drishti: a volume exploration and presentation tool.* Proc. SPIE 8506, Developments in X-Ray Tomography VIII, 85060X (2012).

[15] A. d'Esposito, D. Nikitichev, A. Desjardins, S. Walker-Samuel, and M. F. Lythgoea, *Quantification of light attenuation in optically cleared mouse brains,* J. Biomed. Opt. **20**, 80503 (2015).

[16] A. S. Jacoby, E. Busch-Nentwich, R. J. Bryson-Richardson, T. E. Hall, J. Berger, S. Berger, C. Sonntag, C. Sachs, R. Geisler, D. L. Stemple, and P. D. Currie, *The zebrafish dystrophic mutant softy maintains muscle fibre viability despite basement membrane rupture and muscle detachment,* Development (Cambridge, England) **136**, 3367 (2009).

[17] R. J. Bryson-Richardson, S. Berger, T. F. Schilling, T. E. Hall, N. J. Cole, A. J. Gibson, J. Sharpe, and P. D. Currie, *Fishnet: an online database of zebrafish anatomy,* BMC Biology **5**, 34 (2007).

[18] D. Chen, N. Zeng, Q. Xie, H. He, V. V. Tuchin, and H. Ma, *Mueller matrix polarimetry for characterizing microstructural variation of nude mouse skin during tissue optical clearing,* Biomed. Opt. Express **8**, 3559 (2017).

[19] V. Lauer, *New approach to optical diffraction tomography yielding a vector equation of diffraction tomography and a novel tomographic microscope,* J. Microsc. **205**, 165 (2002).

[20] M. Ravanfar and G. Yao, *Measurement of biaxial optical birefringence in articular cartilage,* Appl. Opt. **58**, 2021 (2019).

5

CONCLUSION AND OUTLOOK

Here we present main conclusions of the work presented in this thesis and recommendations for further research.

5.1. DEPTH INFORMATION FROM 2D DATA

Absolute distance measurement using light is a challenging problem. Generally, the distance from a sample to the sensor cannot be quantitatively and directly derived from a single image. This is due to the fact that in classical imaging, the mapping from object to image is only related to the lateral coordinates. The axial coordinate of the light source is lost in the imaging process. The time-of-flight is in principle suitable for measuring absolute depth, but it can in general not be measured directly due to the high speed of light. Techniques such as phase shifting interferometry can measure relative depth in the sample for depth differences in the order of the wavelength by using the phase information of the object scattered wave. In this case the phase is used in a direct way, as for small depths the phase shift is linear with respect to the sample height. For larger depth differences phase wrapping occurs, but these still can be reconstructed using phase unwrapping if the object profile varies in a continuous way. However, in practice objects can have a rough and discontinuous surface. In this case, only relative depth can be obtained. Plenoptic imaging is a technique that captures the intensity of a scene as well as the direction that the rays are travelling through space. From this also depth information can be reconstructed, however little is known about the axial resolution and it has not been widely used as a tool for metrology.

We demonstrated that absolute depth reconstruction is possible while imaging in full field from a set of phase shifted images with depth resolved digital holography. This method also works when the depth profile does not vary continuously but step wise. For our method, the step size in depth of the sample is not restricted to be within the wavelength. A 100 micrometer axial resolution was achieved using a simple Michelson interferometer holography setup, without magnifying optics. Instead of using the object phase directly, the wave is numerically propagated. This is done with the complex amplitude of the field that is obtained using digital holography. By evaluating the focus at each propagation step, a focus metric as a function of propagation distance is obtained. For rough reflecting samples, the distance where the metric peaks directly gives the absolute distance from object to sample (assuming a plane reference wave). With an analytic model based on the description of the Talbot effect, it was possible to estimate the theoretical axial resolution of this method.

Depth-resolved digital holography is essentially a coherent version of the focus variation microscope (FVM). Coherence in depth-resolved digital holography enables the reconstruction of depth from a single image, since the complex wavefield can be retrieved. With the FVM, the distance between lens and sample is varied and the focus metric is evaluated at each distance. Thus, depth-resolved digital holography is potentially faster since it does not require mechanical scanning. However, optimizing the sample illumination is more challenging for depth-resolved digital holography. In direct backscattering geometry of a planar object the method worked well, but at slight tilt angles the captured reflection was weak. To obtain good depth resolution, the sample is ideally illuminated from different angles. In FVM, this is achieved by positioning LED's in a

ring (ring illumination). The separate LED's are not required to be mutually coherent for FVM. In depth resolved digital holography, illumination with different sources is not trivial because the sources are not generally mutually coherent as required to obtain digital holograms. A possible improvement in this regard could be to include a diffuser in the object arm in a Mach-Zehnder setup to create more diffuse illumination. This can make the method applicable to a more general class of objects, even those with less roughness or objects with different shapes or tilts.

The depth resolution of the method is limited by the highest lateral spatial frequency that can be sampled by the sensor. Therefore, using a camera with a smaller pixel pitch will improve the axial resolution of depth resolved digital holography, but at the same time limits the field of view. Another way to improve axial resolution is by using magnifying optics in the object arm to capture higher spatial frequencies. This will reduce the field of view, but this can be compensated by using a larger sensor.

In our study the sample depth was estimated by finding the maximum of the focus curve. This does not utilize other properties of the focus curve such as the peak width and shape. The method could further benefit from signal processing as applied in FVM, where a polynomial or point spread function is fitted to the focus curve to enhance the axial precision.

5.1.1. APPLICATIONS OF DEPTH-RESOLVED DIGITAL HOLOGRAPHY

There are still significant challenges for depth resolved digital holography before it can find its way in an industrial application. Among the challenges discussed are improving illumination conditions and improving axial resolution by benefiting from more optimal signal processing. Improving resolution by including magnifying optics is more straightforward. The most obvious application of depth resolved digital holography is a coherent version of FVM. This would eliminate the need to perform through-focus scanning needed in FVM. This means that it is not necessary to capture multiple images with different focus and that the sample does not have to be moved with respect to the optics. Since FVM is commonly used in a stable setting, the vibration sensitivity of the holographic system does not have to pose a problem in this regard. In combination with magnifying optics, depth-resolved digital holography has the potential to become a non-scanning counterpart of FVM. Similar to FVM, depth-resolved digital holography can have applications in dimensional metrology and height measurements of planar samples such as for example used in integrated circuits manufacturing, or evaluation of surface topography parameters [1].

5.2. SENSITIVITY AND CONTRAST IN LARGE SCALE ODT

5.2.1. ODT SENSITIVITY IMPROVEMENT

In this thesis we have shown high sensitivity optical diffraction tomography imaging. We have used various experimental methods to reduce the noise and thus increase the sensitivity. These methods are generally applicable in ODT and do not depend on specific experimental equipment. First of all, subtraction of a reference phase reduces coherent noise in the projection. Second, off-axis placement of the sample further reduces coherent noise in the reconstruction. Third, the acquisition of a large number of projections

reduces incoherent noise.

The source of the noise (coherent or incoherent) makes a difference in how the quality of the tomographic reconstruction is affected. Coherent speckle noise reduction deals with static coherent noise. Since the speckle noise is static, it will be present identically in each projection. Furthermore, the static speckle field will coherently interfere with the object and reference wave fields at the sensor. Incoherent noise (such as shot noise) does not interfere with the wave fields and varies randomly per projection. Mathematically the digital hologram then can be represented as

$$I(x,y) = \left|O(x,y) + R(x,y) + U_{speckle}(x,y)\right|^2 + \varepsilon(x,y)_{incoherent}, \tag{5.1}$$

with $U_{speckle}(x,y)$ the static speckle field and $\varepsilon(x,y)_{incoherent}$ the incoherent noise. There is still room for further improvement of the sensitivity by reduction of both noise types, as we will outline here.

SPECKLE NOISE REDUCTION

One way to reduce speckle noise is to use partially coherent illumination (PCI). PCI can be achieved by reducing the spatial coherence of the light source by inserting a rotating diffuser after the laser. This makes both the reference and the object wave to have dynamic speckle patterns on the detector. When the integration time of the camera is set to a value larger than (a fraction of) the period of rotation, the intensity variations in the static speckle field are eliminated. A phase sensitivity improvement of a factor 10 for a single projection is reported with this method [2].

However, as has already been demonstrated by Kostencka et al. [3] and in this thesis the effect of speckle noise can be mitigated by placing the sample off-axis with respect to the center of rotation. Thus, at off-axis positions the effect of speckle noise will be smaller. The question then arises whether speckle noise reduction in the projections (while placing the sample off-axis) reduces the noise in the tomographic reconstruction. We simulated the tomographic reconstruction from phase reconstructions from the hologram in Eq. (5.1) in the presence of speckle noise. The incoherent noise term is set to zero. We use a wavelength of 633 nm and a pixel pitch of 10 μm. The object we consider is a homogeneous transparent cylinder (5 mm diameter) with RI difference Δn=0.0005 with respect to the background, although the value of Δn was found not to influence the outcome of the simulation. The speckle field $U_{speckle}(x,y)$ in Eq. (5.1) is given by $U_{speckle}(x,y) = A_{speckle}(x,y)\cdot e^{i\phi_{speckle}(x,y)}$. For simplicity, we set the standard deviation of $\phi_{speckle}(x,y)$ across the (x,y)-plane to zero, and consider only amplitude speckle. This is modeled by assuming a normally distributed random value over $A_{speckle}(x,y)$, with a standard deviation $\sigma_{speckle}$ and zero mean [4]. Since the speckle field is static, we assume it to be identical for each projection. The phase is reconstructed from the simulated digital hologram using least squares phase unwrapping [5]. The phase projections are then combined in a sinogram and reconstructed using an inverse radon transform. We then compare the noise in the tomographic reconstruction as a function of the number of projections for speckle amplitude noise $\sigma_{speckle} = 0.3$ and $\sigma_{speckle} = 0.03$ in the absence of incoherent noise. This simulates a 10-fold reduction in speckle noise as reported by [2]. The results of this simulation are shown in Fig. 5.1.

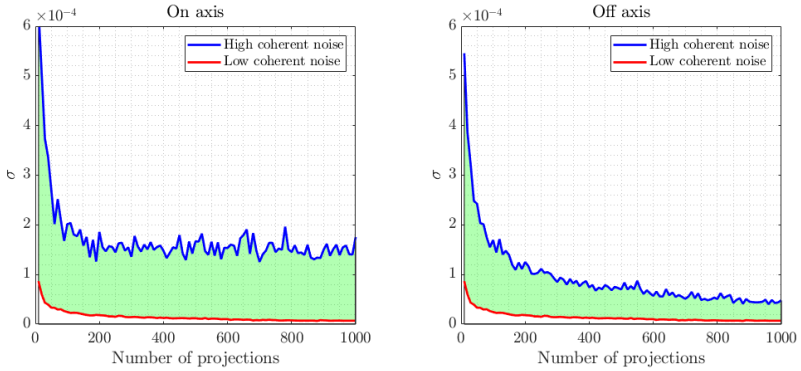

Figure 5.1: Comparison of tomographic reconstructions for high and low coherent noise in the digital hologram ($\sigma_{speckle}$ = 0.3 and $\sigma_{speckle}$ = 0.03 respectively) as a function of the number of projections. Static speckle noise is put to zero. Both the on (a) and off-axis (b) cases are shown for comparison. The improvement as a result of low coherent noise is indicated as the green-shaded area.

5

The simulation results indicate that both on and off-axis placement of the sample benefit significantly from speckle noise reduction in the absence of incoherent noise. The relative improvement due to speckle noise reduction is higher in the on-axis case as expected, but still significant in the off-axis case (roughly a factor 6 improvement). Thus, speckle noise reduction by off-axis placement of the sample can be further enhanced by speckle noise reduction in the phase projections. It must be noted that this assumes a coherent noise limited system. If incoherent noise is not reduced simultaneously, incoherent noise will become the dominant factor and further speckle noise reduction may not yield significant improvement.

INCOHERENT NOISE REDUCTION

A next step for sensitivity improvement is to decrease the incoherent noise. One way to do this is to record a number of frames and average these. By averaging 10 frames, an improvement of roughly 3 times ($\frac{\sigma}{\sqrt{N}}$) is reported by [6]. We investigate how much this noise reduction in a single projection can reduce the noise in tomographic reconstruction by comparing incoherent noise levels σ_{ic} = 0.3 and σ_{ic} = 0.1. The incoherent noise is generated independently from projection to projection, in contrast to the coherent speckle noise in the previous case. We set the static speckle noise to zero. The results are shown in Fig. 5.2 for the on and off-axis cases. In the absence of coherent noise, it appears to make no difference whether the sample is placed on or off-axis in terms of reconstruction noise.

For incoherent noise reduction in the projections of a factor 3 (in the absence of coherent noise), the reduction leads to an improvement of roughly a factor 3 both from on and off-axis placement at 1000 projections. This suggests that the sensitivity improvement in tomographic reconstruction is proportional to the noise reduction in the projections, and significant tomographic noise reduction is thus possible with this method. Again, it must be noted that this is in the absence of coherent noise. If coherent noise is not reduced simultaneously, the effect of incoherent noise reduction may be mitigated.

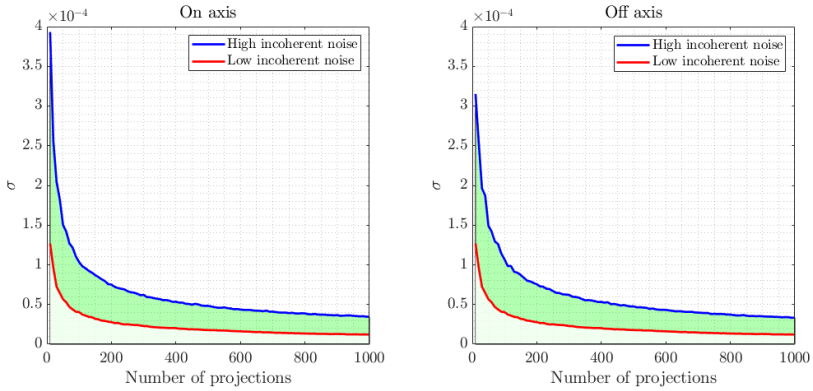

Figure 5.2: Comparison of tomographic reconstructions for high and low incoherent noise in the digital hologram (σ_{ic} = 0.3 and σ_{ic} = 0.1 respectively) as a function of the number of projections. Both the on (a) and off-axis (b) cases are shown for comparison. The improvement as a result of low incoherent noise is indicated as the green-shaded area.

5

Other methods exist to reduce incoherent projection noise even further, but these can require expensive hardware modifications. For example, the use of more laser power reduces incoherent noise but requires a camera with a larger well depth. This can lead to an improvement of the phase accuracy up to a factor 5 in sensitivity [6] in a single projection.

From the preceding, we can conclude that both coherent and incoherent noise contributions must be tackled independently in order to improve the sensitivity in the tomographic reconstruction. Otherwise, noise reduction will be limited by the coherent noise despite efforts to reduce incoherent noise, and vice versa. This is shown in Fig. 5.3, where the reconstruction noise σ is simulated on and off-axis as a function of coherent noise with different cases of constant incoherent noise (a) and vice versa (b). The number of projections for the tomographic reconstruction is 1000, with all other simulation parameters identical as before.. The slope in Fig. 5.3 (a) gives the change in reconstruction noise as a function of coherent projection noise. Since coherent noise affects the center of rotation more than the off-axis area, the slope is highest for the on-axis curves. Another point from Fig. 5.3 (a) is that for small values of $\sigma_{coherent}$, the reconstruction noise becomes limited by the incoherent projection noise. This can be seen by the higher offset of the purple off-axis curve where incoherent noise is present, as compared to the red curve. This confirms the idea outlined earlier that at some point, further reduction of coherent noise is not effective and further reduction is possible by reduction of incoherent noise independently. Figure 5.3 (b) shows the same principle, but then with incoherent and coherent noise interchanged. The off-set of the purple curve (off-axis in the presence of incoherent noise) shows that reducing incoherent noise in the phase projections does not yield further improvement at some point. Only when coherent noise is reduced independently (red off-axis curve), a further step in noise reduction can be made. Another interesting feature of Fig. 5.3 (b) is that in the presence of coherent noise, incoherent noise reduction is not effective for the on-axis case (yellow line). Thus, for

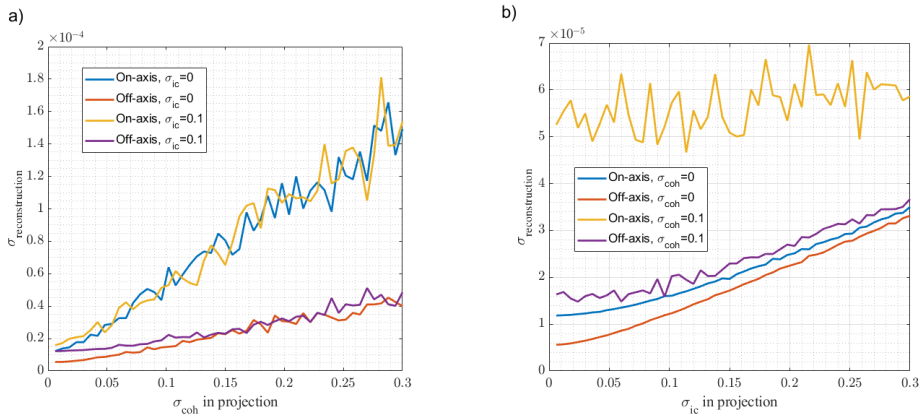

Figure 5.3: (a): Reconstruction noise σ as a function of the coherent projection noise σ_{coh} for different scenario's. (b) Reconstruction noise σ as a function of the incoherent projection noise σ_{ic} for different scenario's.

incoherent noise reduction (e.g. through averaging projections) to be effective in the presence of coherent noise, off-axis sample placement should be considered.

5.2.2. APPLICATIONS OF LARGE SCALE HIGH SENSITIVITY ODT

In this thesis we have applied optical diffraction tomography (ODT) to a millimeter-sized zebrafish-larva. The zebrafish is a well-known and studied model, and we could compare the imaging results with optical projection tomography (OPT) reconstructions. Furthermore, the zebrafish larva itself is suitable for testing of large scale ODT, since the larva consists of clearly separated regions with different refractive indices (RI's). For example the brain, eyes, spine and yolksack all have different RI's and are spatially separated. The question arises whether large scale ODT has applications in other kinds of biological samples. To that end we already imaged an adult zebrafish heart that was cryo-injured. Biologists study zebrafish heart recovery by estimating the volume of the injured part relative to the total volume. This is done by cutting the tissue into thin slices. By estimating the relative injured area per slice, the total relative volume is estimated. We furthermore demonstrated that with large scale ODT, relative volume estimation can be done digitally with the 3D dataset without cutting the tissue. This potentially saves significant labour, amount of resources and time. We demonstrated automatic segmentation of the injured area on a single slice; the next step in this regard is to apply 3D image segmentation to further speed up this process.

Another potential application is in imaging human tissue where ODT has mainly been applied to imaging at the cellular level. To the best of our knowledge millimeter-sized volumes of human tissue have not been studied with ODT before. In order to demonstrate the viability of large scale ODT on human tissue, we applied our technique to human prostate tissue taken after clinical biopsy or surgery. Prostate specimens are generally evaluated with high resolution microscopy in the form of mechanically sliced

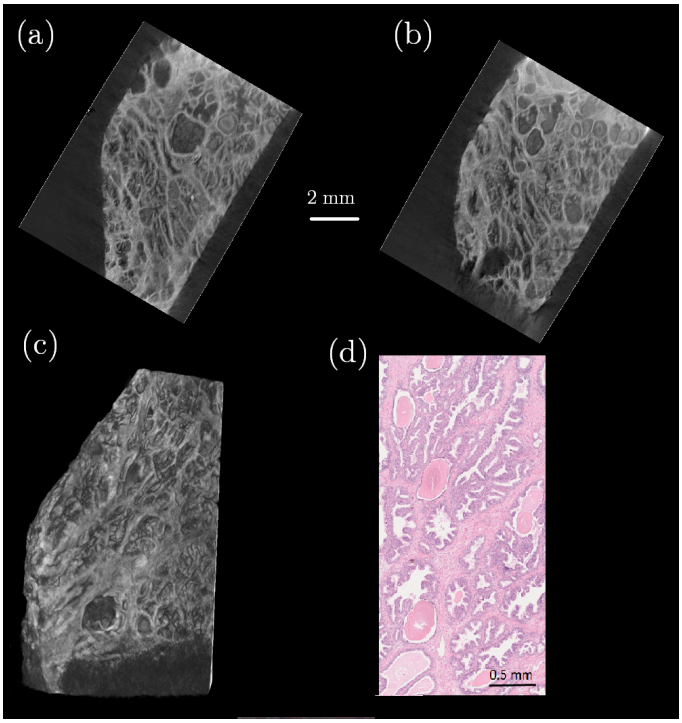

Figure 5.4: (a)-(b): Two virtual cross-sections of a optically cleared clinical prostate specimen imaged with ODT; (c) 3D rendering of the reconstruction; (d) H&E-stained histology image of a slice of the same sample.

thin tissue sections. These sections are stained with haematoxylin and eosin stain (H&E-stain). With this stain, the general layout and distribution of cells can be studied and it provides a general overview of tissue structure with nuclei and extracellular material having a different color. However, since this gives only 2D-structural information of a limited number of slices, little is known about 3D architectural features of prostate tissue and prostate cancer. 3D-microscopic analysis of prostate specimens has been performed by Royen et al. [7] using confocal microscopy on optically cleared tissue. Structures up to a depth of 800 μm were visualized using fluorescence contrast. Large scale ODT operates in transmission and can thus achieve greater imaging depth than confocal microscopy and image intrinsic RI contrast. We obtained intact fresh and formalin-fixed paraffin-embedded (FFPE) clinical prostate specimens that have been optically cleared from Erasmus Medical Centre (EMC). The sample dimensions were in the order of several millimeters. ODT images are shown in Fig. 5.4. For comparison, a HE-stained image from a slice of the same sample has been included in Fig. 5.4 (d). The results show that ODT is a method to do label free imaging with a tissue thickness up to a factor 5 of what was previously done using confocal microscopy. This offers potential new insights in large scale 3D structures of human prostate tissue that was not accessible before. Further research can be done to investigate how these structures change in the presence of, for example, different grades of prostate cancer.

5.2.3. POLARIZATION CONTRAST

In chapter 4, we demonstrated that 3D polarization contrast imaging is possible within the framework of large scale ODT. We also pointed out the main limitation of this method. The contrast mechanism becomes non-linear when the rotation of the polarization is not small ($\delta < \pi$), and thus tomographic reconstruction through inverse radon transform does not give accurate results without proper signal processing. This places a restriction on the samples that can be imaged. The developing muscle tissue of an optically cleared zebrafish larva could be imaged with our method as the phase difference δ is sufficiently small. However, a FEP-tube (Fluorinated Ethylene Propylene) could not. Although the FEP-tube is transparent and can be RI matched with water, its strong birefringence causes a large rotation of the polarization when the light propagates through this millimeter sized sample. This is clearly apparent in the reconstructed intensity projection in Fig. 5.5 where the intensity is modulated due to the rotation of the polarization across the FEP-tube. We also applied polarization contrast ODT on millimeter-sized clinical prostate tissue samples and found a similar effect. From single crossed-polarizer projections it was clear that the tissue contained highly birefringent structures. In both cases, standard tomographic reconstruction generated an image with little contrast due to the large rotation of the polarization.

The question arises how the tomographic reconstruction procedure must be modified to incorporate the non-linearity of the contrast mechanism. In chapter 4, we already showed that the general case of polarization contrast tomographic reconstruction can be approached as a modified phase unwrapping problem. The polarization rotation is encoded in the amplitude as a wrapped signal. We demonstrated through simulation that by approaching the problem in this way, contrast can be reconstructed even when the polarization rotation is no longer small. Our approach takes into account the physical forward model by which a projection is formed, i.e. that the amplitude on the detector scales with $|\sin(\frac{\delta}{2})|$, where δ is the phase shift between the two orthogonal polarizations. Only for small δ can this be approximated as a linear relation. Moreover, when the phase difference δ is even larger, the birefringence cannot be unambiguously determined and must be unwrapped.

In addition to the non-linear relation of the birefringence with the projection amplitude, another complication is that the amplitude is also modulated by several other factors:

- The illumination amplitude $A(x, y)$ varies spatially across the detector in the general case of non-uniform illumination. We thus reconstruct $|A(x, y)\sin(\frac{\delta}{2})|$, and $A(x, y)$ must be corrected for. This is analogous to correcting for the background phase in the case of phase contrast, by removing the sample and only measuring the background phase. However, the term $A(x, y)$ cannot be measured directly since if we remove the sample in the crossed-polarizer configuration, there is no signal behind the second (analyzer) polarizer.

- The sample itself can be (weakly) absorbing even in the case of cleared tissue. This is an additional cause of amplitude modulation and can make quantitative analysis of the amplitude difficult.

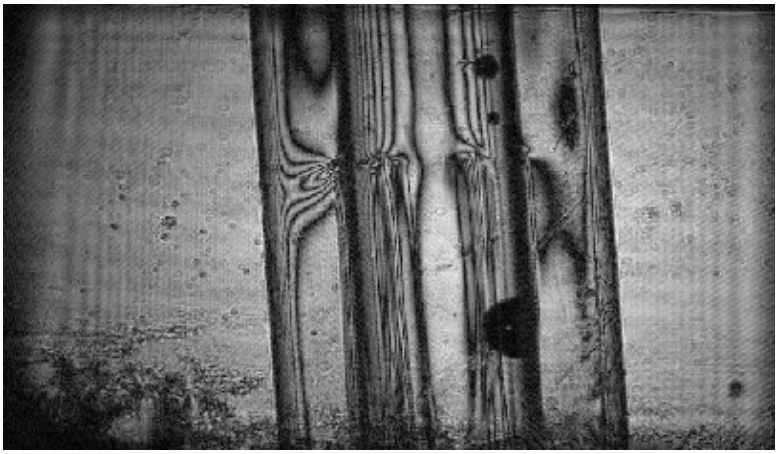

Figure 5.5: Intensity projection of a FEP-tube reconstructed from a digital hologram; the intensity across the tube is modulated due to the rotation of the polarization of the object wave across the tube.

- Local sample inhomogeneity's can cause strong refraction. This can cause intensity "hot-spots" on the detector, resulting in amplitude modulations that cannot be directly related to the relative phase δ.

Although these issues are not very relevant for the current work on zebrafish imaging, for extension of the method to a more broad set a samples they need to be addressed and require further processing of the raw amplitude projections. The goal of such preprocessing is to retrieve an amplitude projection where the only source of amplitude modulation is the relative phase shift δ and additional scaling factors are removed.

The first challenge can be addressed by rotating the second polarizer to be parallel to the first one, and capturing a reference image. Assuming that rotation of the polarizer does not induce a shift of the wavefield, the reference image yields a scaled version $cA(x,y)$ of the illumination amplitude. The constant c can be estimated by comparing the reference image with the maximum-intensity in the crossed polarizer image. The second challenge is more fundamental, as it requires knowledge of the object to correct for. Attenuation contrast can however be reconstructed using the amplitude of the wavefield that is measured with parallel polarizers. Attenuation can then be incorporated in the reconstruction model, as a linear attenuation coefficient k in the projection [8]. In this case, the constant k functions as a correction constant to normalize the amplitude signal. The third challenge can be dealt with by applying a threshold to the amplitude projections. Noise will still be a part of the image, however phase unwrapping algorithms (such as the least squares algorithm used in this work) show that proper reconstruction is still feasible with noisy images.

The development of a generalized reconstruction procedure for strongly birefringent samples is in any case a challenge that will involve experimental as well as signal processing efforts before it can be practically applicable. Even then, the results are most likely to be qualitative rather than quantitative, since the reconstruction model at this point does not take into account fiber orientation. Further research is needed to determine

whether it is possible to retrieve this orientation and how. Most likely, this will involve the use of generalized Jones matrices making the analysis considerably more complex, or additional experimental efforts by measuring under different polarization angles. Eventually, fiber orientation could offer an additional contrast mechanism on its own and provide insight in the organization of muscle or brain tissue.

REFERENCES

[1] E. N. Grossman, M. Gould, and N. P. Mujica-Schwann, *Robust evaluation of statistical surface topography parameters using focus-variation microscopy,* Surface Topography: Metrology and Properties **4**, 035003 (2016).

[2] Y. Choi, T. D. Yang, K. J. Lee, and W. Choi, *Full-field and single-shot quantitative phase microscopy using dynamic speckle illumination,* Opt. Lett. **36**, 2465 (2011).

[3] J. Kostencka, T. Kozacki, M. Dudek, and M. Kujawińska, *Noise suppressed optical diffraction tomography with autofocus correction,* Opt. Express **22**, 5731 (2014).

[4] H. Yu, M. Ding, X. Zhang, and J. Wu, *Pcanet based nonlocal means method for speckle noise removal in ultrasound images,* PLOS ONE **13** (2018).

[5] D. C. Ghiglia and L. A. Romero, *Robust two-dimensional weighted and unweighted phase unwrapping that uses fast transforms and iterative methods,* J. Opt. Soc. Am. A **11**, 107 (1994).

[6] P. Hosseini, R. Zhou, Y.-H. Kim, C. Peres, A. Diaspro, C. Kuang, Z. Yaqoob, and P. T. C. So, *Pushing phase and amplitude sensitivity limits in interferometric microscopy,* Opt. Lett. **41**, 1656 (2016).

[7] M. E. van Royen, E. I. Verhoef, C. F. Kweldam, W. A. van Cappellen, G.-J. Kremers, A. B. Houtsmuller, and G. J. L. H. van Leenders, *Three-dimensional microscopic analysis of clinical prostate specimens,* Histopathology **69**, 985.

[8] M. Fang, D. Dong, C. Zeng, X. Liang, X. Yang, A. Arranz, J. Ripoll, H. Hui, and J. Tian, *Polarization-sensitive optical projection tomography for muscle fiber imaging,* Scientific reports **6**, 19241 (2016).

SUMMARY

Optical imaging is the imaging of objects with visible light. It is a tool often used for diagnostic purposes, such as in biomedical and material sciences. Digital holography is an optical imaging technique that captures and images the amplitude as well as the phase (the complex amplitude) of the lightwave. An advantage is that the complex amplitude can be calculated in different propagation planes. The goal of this thesis is to use digital holography to image depth of a reflecting surface as well as make 3D images of biological samples, and to contribute to the theoretical understanding in this regard.

First of all we show, with a Michelson digital holography setup, that depth resolved imaging can be achieved of a rough reflecting surface, without physically scanning through-focus. We do not use any lenses for the actual imaging (lens free imaging). Furtermore, the setup is simple in terms of components. The method can image a surface of roughly half a centimeter by half a centimeter with a depth resolution of 100 micron. This is a significant improvement with respect to previous research in this regard. We achieve this improved depth resolution by introducing a phase-shift in the reference arm, in combination with using a pellicle beam-splitter. By introducing a phase-shift in subsequent captures and combining these later, a higher lateral and depth resolution can be achieved. We also present a theoretical framework to understand the depth-resolution of this method. We achieve this by describing the depthresolution in terms of the Talbot-effect. This effect occurs when light falls on a periodic diffraction grating. The image of this grating will repeat itself (self imaging) at certain propagation-distances from the diffraction grating. By treating the variance as a function of propagation distance of each spatial frequency separately and eventually summing these, we can calculate an overal focus-curve. The maximum of this focus-curve corresponds to the distance/depth of the object with respect to the detector in case the reference wave is a plane wave. Since the depth-resolving method depends on spatial frequencies in the reconstruction, the method only works when there is texture or roughness on the surface that is to imaged. Because this method does through-focus scanning numerically and not physically (e.g. by scanning the lens), this method can be useful when surfaces must be characterised fast or when absolute distance measurements are needed.

Secondly, we apply digital holography in combination with tomography to image a relatively large piece of tissue (in the order of 1 mm) in 3D with phaseconstrast. This is significantly larger than has been achieved so far using optical phase tomography. We use a Mach-Zehnder holography setup in transmission. The light that travels through the sample undergoes a phase modulation, which can be reconstructed with digital holography. By repeating this from multiple illumination angles a 3D phase contrast image can be reconstructed using computed tomography. We apply this to a zebrafish larva. This is a relatively large sample for optical phase tomography. The sample is therefore first made transparent using optical clearing in a benzyl-alcohol benzyl-benzoate solution. This homogenises the refractive index of the sample, reducing the light scattering. The

consequence however is a strong reduction of the phasecontrast. The influence of noise is then much larger and pollutes the image reconstruction, and as a result the zebrafish larva is hardly discernible. In order to avoid this problem, we place the sample off-axis with respect to the tomographic rotation axis. The fact that the object will now be out of focus for part of the rotation we compensate by tracking the in-focus position of the sample. We then numerically refocus so that the object will be in focus for all rotation angles. The result is that coherent speckle noise is strongly reduced. We also increase the number of projections to reduce the incoherent noise. We demonstrate that this approach makes it possible to image samples of several millimeters in 3D with phasecontrast. We furthermore demonstrate clinically relevant applications of this technique, such as imaging a cryo-injured zebrafish heart. The tissue regenerates after injury. Using optical phase tomography it is possible to image the heart and injured part in 3D, and also to determine the volume of the injured area. We also demonstrate the technique on prostate tissue samples of several millimeters and successfully reconstruct 3D phase contrast images of internal structures in the tissue. The method thus enables label-free imaging of structures in large scale biological samples. A limitation is the large amount of data needed to reconstruct an image with low noise levels and high resolution.

Finally we demonstrate combined phasecontrast and polarisationcontrast 3D tomography on a zebrafish larva. This combination is possible by capturing, besides the phase, also the amplitude of the wavefield. Certain types of tissue like muscle-tissue in a zebrafish tail are birefringent. The polarisation of the lightwave going through the sample undergoes a change as a result. This can be made visible using the amplitude of the wavefield by introducing cross-polarizers in the sample-arm before and after the sample. Only the light that travelled through birefringent tissue and changed its polarisation reaches the camera. In a digital holography setup we thus measure the projection of the amplitude as well as the phase. By measuring the projections from different angles and applying tomographic reconstruction a 3D reconstruction can be made of the muscle-tissue in the zebrafish tail. The polarisationcontrast image gives a significantly higher signal-to-noise ratio compared to the phasecontrast reconstruction. We also provide a theoretical analysis of the system (assuming uniaxial birefringence) and show that there are several non-linear dependencies in the signal. The most limiting of these is the relative phase-shift between the two polarisation states of the lightwave. If this becomes too large because of the thickness and/or strong birefringence of the sample, no meaningful image-reconstruction of the sample can be made using conventional reconstruction techniques. Using knowledge of the physical forward model, under certain assumptions a correct projection can be retrieved in principle, which we demonstrate in simulation. The non-linearity as a result of the tomographic angle causes a modulation in the background of the reconstruction, but does not cause modulation in the reconstruction of the birefringent sample itself and therefore does not pose a problem for qualitative reconstruction of a single homogeneous object. For absolute quantification of the birefringence, more information is needed per projection, as well as a non-linear inversion scheme. This research demonstrates that in combination with phasecontrast tomography, also polarisationcontrast tomography is possible, and that the same benefits (such as numerical focusing) apply.

SAMENVATTING

Optische beeldvorming is het afbeelden van objecten met zichtbaar licht. Het is een middel dat veel gebruikt wordt voor diagnostische toepassingen, zoals in de biomedische wetenschappen en materiaalonderzoek. Digitale holografie is een optische beeldvormingstechniek die zowel de amplitude als de fase (de complexe amplitude) van de lichtgolf vastlegt en afbeeldt. Een voordeel hiervan is dat een afbeelding op verschillende dieptes uitgerekend kan worden. Het doel van deze thesis is om digital holografie te gebruiken om zowel diepte van het oppervlakte van een reflecterend object af te beelden als 3D afbeeldingen te maken van biologische objecten, en een bijdrage te leveren aan het theoretische begrip hiervan.

Allereerst laten we, met een Michelson holografie opstelling, diepte-opgeloste beeldreconstructie zien van een ruw reflecterend oppervlak, zonder fysiek door-focus te hoeven scannen. We gebruiken geen lenzen om af te beelden ("lens-free imaging"). De opstelling is verder simpel qua componenten. We kunnen een oppervlak van ongeveer een halve centimeter bij een halve centimeter afbeelden en behalen een diepte-resolutie van 100 micron. Dit is een significante verbetering ten opzichte van voorgaand onderzoek. De hogere diepte resolutie behalen we onder andere door het introduceren van een faseverschuiving in de referentie-arm, in combinatie met het gebruik van een membraan bundelsplitser. Door een faseverschuiving te introduceren in opeenvolgende opnames en deze later te combineren, kan de laterale en diepte resolutie verhoogd worden. Tevens laten we ook een theoretisch kader zien waarin de diepte-resolutie van deze methode begrepen kan worden. Dit doen we door gebruik te maken van een beschrijving van de diepteresolutie in termen van het Talbot effect. Dit effect treedt op wanneer licht op een periodieke diffractietralie valt. De afbeelding van deze diffractietralie zal zich dan herhalen op gezette propagatie-afstanden van de diffractietralie. Door de variantie als functie van de afstand van elke spatiële frequentie afzonderlijk te beschouwen en uiteindelijk te sommeren, kunnen we een zogenaamde focus-curve berekenen. Het maximum van deze curve correspondeert met de afstand van het object tot de detector. Aangezien de methode afhankelijk is van spatiële frequenties in de reconstructie, werkt deze methode alleen wanneer er sprake is van structuren of ruwheid op het af te beelden oppervlak. Doordat bij deze methode het door-focus scannen numeriek gebeurt en niet fysiek, kan het bruikbaar zijn wanneer oppervlakten snel gekarakteriseerd moeten worden of wanneer absolute afstandmetingen nodig zijn.

Vervolgens passen we digitale holografie toe in combinatie met tomografie om een relatief groot stuk weefsel (in de orde van 1 mm) in 3D af te beelden met fasecontrast. Dit is significant groter dan toe nu toe met fasetomografie bereikt werd. Het licht dat door het object gaat ondervindt een fase modulatie. Met digitale holografie kan een projectie van de fase worden bepaald. Door dit te doen vanuit meerdere hoeken kan een 3D fasecontrast afbeelding gereconstrueerd worden met behulp van computer tomografie. We passen dit toe op een zebravis larve. Dit is een relatief groot object voor optische

fasetomografie. Het object is daarom eerst opgehelderd door het te laten rusten in een benzyl-alcohol benzyl-benzoaat oplossing. De brekingsindex van het object wordt hierdoor gehomogeniseerd waardoor de lichtverstrooiing afneemt. Dit heeft echter als gevolg dat het fasecontrast sterk vermindert. De invloed van ruis is dan veel groter en vervuilt dan de beeldreconstructie waardoor de zebravis larve nauwelijks te onderscheiden is. Daarom plaatsen we het object op enige afstand van de tomografische rotatieas, en compenseren we het feit dat het object dan uit focus is gedurende een deel van de rotatie door de in-focus positie van het object te meten. Vervolgens kunnen we het object digitaal herfocuseren en het in focus afbeelden voor alle rotatiehoeken. Dit heeft als gevolg dat de coherente (spikkel) ruis sterk gereduceerd wordt. Tevens verhogen we het aantal projecties om de incoherente ruis te verminderen. We laten zien dat met deze aanpak het mogelijk is om objecten in de orde van een milimeter in 3D af te beelden met fasecontrast. We demonstreren tevens een klinisch relevante toepassing met deze techniek, namelijk het afbeelden van een zebravishart dat beschadigd is door zogenaamde cryo-injury. Het weefsel herstelt zich na deze beschadiging. Middels fasetomografie kunnen we het geregenereerde deel in 3D te reconstrueren, en tevens het volume ervan bepalen. Ook demonstreren we de techniek op prostaat weefsel, en blijkt het mogelijk stukjes weefsel van meerdere millimeters in 3D af te beelden met goed fasecontrast. De methode heeft de potentie om zonder labelen structuren in grootschalige biologische objecten te reconstrueren. Een beperking is de grote hoeveelheid data die nodig is voor een reconstructie met lage ruis en hoge resolutie.

Als laatste demonstreren we gecombineerde polarisatiecontrast en fasecontrast 3D tomografie op een zebravis larve. Deze combinatie is mogelijk door naast de fase ook de amplitude van het golfveld mee te nemen in de reconstructie. Bepaalde type weefsels, zoals spierweefsel in de staart van de zebravis larve, zijn dubbelbrekend. De polarisatie van de lichtgolf die door het object gaat ondergaat daardoor een verandering. Dit kan zichtbaar gemaakt worden met de amplitude van het golfveld door gekruiste polarisatie filters voor en na het object te introduceren; enkel het licht wat door dubbelbrekend weefsel is gegaan en daardoor van polarisatie is veranderd bereikt de camera. In een digitale holografie opstelling meten we zodoende de projectie van zowel de fase als de amplitude. Door deze projecties voor verschillende hoeken te meten en tomografische reconstructie toe te passen kan hiermee een 3D reconstructie gemaakt worden van het spierweefsel in de staart van de zebravis. De polarisatiecontrast reconstructie geeft een significant hogere signaal-ruis verhouding dan de fasecontrast reconstructie. Tevens doen we een theoretische analyse van het tomografische polarisatiecontrast (onder de aanname van uniaxiale dubbelbrekendheid) en laten we zien dat er verschillende niet-lineaire afhankelijkheden zijn in het signaal. De meest beperkende hiervan is de relatieve faseverschuiving tussen de twee polarisatietoestanden van de lichtgolf. Als deze te groot wordt door de dikte en/of sterke dubbelbrekendheid van het object kan er geen betekenisvolle 3D afbeelding gemaakt worden met behulp van conventionele reconstructie technieken. Met kennis van het fysische voorwaartse model demonstreren we in simulatie dat onder bepaalde aannames een correcte projectie achterhaald worden. De niet-lineariteit als gevolg van de tomografische hoek zorgt welliswaar voor een modulatie in de achtergrond van de reconstructie, maar zorgt niet voor modulatie in de reconstructie van het dubbelbrekende object zelf en vormt daarom geen probleem voor kwalitatieve

reconstructie van een enkel homogeen object. Voor absolute kwantificering van de dubbelbrekendheid is echter meer informatie nodig per projectie, evenals een niet-lineair inversieschema. Dit onderzoek laat zien dat in combinatie met fasecontrasttomografie ook polarisatietomografie mogelijk is, en dat van dezelfde voordelen (zoals numeriek herfocussen) gebruik gemaakt kan worden.

ACKNOWLEDGEMENTS

Vele mensen zijn direct of indirect erg belangrijk zijn geweest voor de totstandkoming van dit proefschrift, die ik graag wil bedanken, hopende dat ik daarbij niemand over het hoofd zie.

In de eerste plaats dank naar mijn ouders, Marja en Jan. Jullie hebben qua onderwijs altijd de rode loper uitgelegd, en gezorgd dat het ons nooit ergens aan ontbrak. Zelfs met een tweede kind op komst steunden jullie mijn keuze om een tweede master te doen, waar dit promotietraject op volgde. Dankjulliewel voor jullie steun en betrokkenheid over de jaren. Eveneens wil ik bij deze mijn schoonouders bedanken voor hun directe en indirecte steun, als ook Rene en Anneke.

Jeroen, bedankt voor deze kans om onder jouw supervisie te promoveren, en de ruimte die je gaf om verschillende onderwerpen te verkennen. Ik kon vrijwel altijd bij je terecht om te sparren over het onderzoek, een laagdrempeligheid die niet overal vanzelfsprekend is. Als ik door de bomen het bos niet meer zag, hielp dit om weer een duidelijke richting te krijgen en concrete stappen voorwaarts te maken. Je commentaar op mijn schrijven tilde het werk naar een hoger niveau, was uitgebreid en liet nooit lang op zich wachten. Je oog voor detail heeft me geleerd dat een hoop details bij elkaar een grote verbetering kunnen geven. Bedankt voor je actieve betrokkenheid.

Lucas, ik heb je betrokkenheid als promotor als erg waardevol ervaren. Zowel het inhoudelijk sparren tijdens de voortgangsbesprekingen, alsook je snelle feedback op het schrijfwerk en het belang dat je hechtte aan het op tijd afronden van promotieonderzoek. Op een aantal momenten voorafgaand aan deze PhD vroeg ik je over promotieonderzoek (waaronder op de fiets als we elkaar tegenkwamen); je zei dat vooraf je niet weet wat er uit onderzoek gaat komen, en dat dat een onzekerheid is waar een promovendus mee om moet kunnen gaan. Terugkijkend is dit een scherpe samenvatting van de uitdagingen de afgelopen vier jaar.

I would further like to thank the independent members willing to take part in the doctoral committee for this defense, namely Prof. dr. ir. Fons Verbeek, Prof. dr. ir. den Boef, Prof. dr. Kujawinska, Prof. dr. Urbach and Prof. dr. Vdovine.

Sonja, ontzettend bedankt voor al je hulp met de samples. Een hoop van dit onderzoek leunde hevig op het door jou ter beschikking stellen van zebravis larven om onze beeldvormingstechniek op te testen. Een flink aantal keren kon ik bij je terecht voor nieuwe samples (no questions asked). Dit hielp me enorm met de voortgang van het onderzoek. Bij deze wil ik ook Hessel bedanken voor hulp met de samples en de zebravishartjes, die we uiteindelijk ook konden imagen. Ook dank aan Jeroen Bakkers voor het ter beschikking stellen van middelen in dit opzicht. In dit kader wil ik ook Tjakko van der Ham bedanken voor het beschikbaar stellen van samples in het beginstadium van het onderzoek.

Martin, Esther en Arno, wat later in het onderzoek zijn we begonnen met het testen van onze beeldvormingstechniek op prostaatweefsel. Alhoewel niet zonder slag of stoot,

kregen we voor een deel van het weefsel toch interessante beeldreconstructies, hetgeen belangrijk was om de toepasbaarheid van de techniek te illustreren. Bedankt voor het beschikbaar stellen van weefsels en het meedenken over hoe we dit konden laten slagen!

Ron Hoogerheide, bedankt voor je hulp met voornamelijk het vervaardigen van testobjecten, maar ook voor alle andere keren dat ik bij je binnen kon lopen voor praktische benodigdheden, je hulp voor bij het gebruik van de zandstraal machine en je bereidheid tot meedenken.

Ronald, vanaf het begin bij de aanschaf van een nieuwe computer, tot aan het einde kon ik altijd bij je terecht betreffende IT gerelateerde zaken. Bedankt voor de prettige samenwerking.

Jelle van der Horst, meer dan twee jaar hebben onze projecten overlap gehad. Met je ervaring stond je altijd klaar om te helpen, en gedurende het onderzoek heb ik daar ontzettend veel aan gehad, waarvoor dank.

Anna, bedankt voor je hulp met beeldsegmentatie algoritmes.

Robert Moerland, voor allerhande vragen omtrent imaging kon ik altijd bij je langslopen, waarvoor dank. Ook je initiatief om de experimentalisten meeting op te zetten heeft me erg geholpen (met name als start voor het afbeelden van polarisatie contrast).

Leon, ik heb een aantal keer voor belangrijke experimentele zaken beroep op je kunnen doen, hetgeen een en ander zeker vergemakkelijkt heeft, waarvoor dank.

Mojtaba, thank you for getting me started with the experimental setup of microscopy related techniques early in the PhD.

Tom Callewaert, bedankt voor je hulp bij de OCT metingen als referentie voor een test object voorafgaand aan het eerste paper.

Jelle Storteboom, Christiaan en Taylor, incidenteel heb ik een beroep op jullie kunnen doen wat betreft experimentele benodigdheden, waarvoor dank.

Thim Zuidwijk, in de master heb ik je leren kennen als iemand die altijd klaar stond om even te helpen, en ook tijdens mijn promotie kon ik bij je terecht om bijvoorbeeld een laser te lenen als de onze niet voldeed. Dit heeft ons een hoop tijd gescheeld. Dank voor je behulpzaamheid!

Patrick van Holst, bedankt voor je begeleiding bij en het ter beschikking stellen van jullie White Light Interferometer voor referentie metingen. Dit heeft ons erg geholpen voor het eerste artikel.

Elizabeth, on a number of occasions you shared insights on our image reconstructions of zebrafish, and also allowed me to make use of your facilities for sample preparation, which simplified a lot for me. Also Leonie helped me with sample preparation on different occasions; thank you both!

Carel Heerkens, gedurende mijn promotie kon ik gebruik maken van jullie faciliteiten en heb je me geholpen in het gebruik ervan, waarvoor dank.

Annelies en Angela, vele malen heb ik een beroep kunnen doen op jullie administratieve ondersteuning, en in het beginstadium van de promotie ook op Liesbeth en Joyce. Dankjulliewel!

Wojciech Krauze and Kyoohyun Kim, thank you for making available your ODT algorithms and support in adapting it for our purposes. Even though we did not implement them for our reconstructions eventually, it was useful to compare our results against.

Aurele en Nandini, since work I did under your supervision was a starting point for the first publication, it is only appropriate to thank you on this occasion.

Miriam Menzel, our interaction was extremely brief, but very critical. Thank you for the discussions and taking a critical look at some of our assumptions underlying the theoretical justification of polarization contrast tomography.

Zo nu en dan inhoudelijk sparren met iemand die niet direct bij het onderzoek betrokken was heb ik als erg waardevol ervaren. Hiervoor wil ik graag bedanken: Sjoerd Stallinga, Bernd Rieger, Ted Young, Eric Verschuur, Florian Bociort, Frans Vos, Rob Remis, Koen van Dongen en Jos Thijssen.

Kees Hagen, het was erg waardevol om jou als mentor te hebben binnen het graduate school programma. Je aanpak om standaard twee keer per jaar af te spreken vond ik prettig; ook al was er meestal geen concreet issue, toch vulden we de tijd makkelijk op. Bedankt voor de nuttige en aangename gesprekken.

Gyllion, Boling, since very early in the PhD we have been sharing the same office and developed a nice friendship. Also after moving to another more spacious office, we remained co-located. We shared struggles, but most of all a lot of fun and interesting discussions on all kinds of things. Thanks for the great time.

Verder wil ik ook Ruben, Nico en Andrei, bij wie ik een rol mocht spelen in de begeleiding van hun stage/afstuderen, bedanken voor hun inhoudelijke bijdragen en discussies.

Musab, bedankt voor je gezelschap en vriendschap de afgelopen jaren in Delft. Het wekelijkse koffiedrinken op vrijdag middag op de campus zal ik missen

Over the last few years, I have had lots of fun at the table-soccer table during the breaks with many different people. The vibe of friendly competition amongst the enthusiasts brought some welcome distraction and excitement in daily PhD life. Thank you for the fun games, Pierre, Jelle, Leon, Gyllion, Boling, Jos, Joost, Mojtaba, Davide, Martin, Jin, Yuri and all others

Bas, als tweelingbroers hebben we altijd een sterke band gehad, en een gesprek met jou hielp altijd om een en ander, waaronder obstakels in het onderzoek, in perspectief te zetten. Bedankt voor al je steun.

Jolien, de afgelopen 10 jaar dat we samen zijn heb je altijd achter me gestaan, ook toen ik nog verder wilde studeren, we kinderen kregen en we het financieel niet zo heel breed hadden (volgens CBS maatstaven). Maar arm heb ik me nooit gevoeld met jullie; dank aan jou en de meisjes voor al jullie liefde en geduld de afgelopen jaren.